ELECTRONIC EQUALIZATION OF HIGH-SPEED MULTI-MODE FIBER LINKS

A Thesis
Presented to
The Academic Faculty

by

Kasyapa Balemarthy

In Partial Fulfillment
of the Requirements for the Degree
Doctor of Philosophy in the
School of Electrical and Computer Engineering

Georgia Institute of Technology
August 2007

ELECTRONIC EQUALIZATION OF HIGH-SPEED MULTI-MODE FIBER LINKS

Approved by:

Professor John Barry, Committee Chair
School of Electrical and Computer Engineering
Georgia Institute of Technology

Professor Stephen E. Ralph, Advisor
School of Electrical and Computer Engineering
Georgia Institute of Technology

Professor Steven W. McLaughlin
School of Electrical and Computer Engineering
Georgia Institute of Technology

Professor Erik Verriest
School of Electrical and Computer Engineering
Georgia Institute of Technology

Dr. Robert Lingle Jr.
OFS Fitel and
School of Electrical and Computer Engineering
Georgia Institute of Technology

Date Approved: July 5, 2007

कायेन वाचा मनसेन्द्रियैर्वा बुद्ध्यात्मना वा प्रकृतेः स्वभावात् ।
करोमि यद्यत्सकलं परस्मै नारायणायेति समर्पयामि ॥

Everything that I do with my Body, Speech, Mind,

Sensory Organs, Behavior, Intellect and Soul

— I dedicate to God

ACKNOWLEDGEMENTS

I would like to thank Prof. Stephen Ralph for introducing me to the world of multi-mode fiber communications. His Socratic method of supervising this research led to a deeper understanding of the fundamental Physics behind optical communications as well as its practical implications. I would also like to thank my friends in the UFOCL group for the years of fun and work: Ketan Patel, Jeffrey Lillie, Arup Polley, and Joong Kim.

I am grateful to Dr. Robert Lingle Jr. and OFS for funding this research effort. This fruitful collaboration has not only resulted in influencing the course of the IEEE 802.3aq 10 Gbps Ethernet standard, it has also given concrete form to my career plans.

I would like to thank Prof. John Barry, Prof. Steven McLaughlin, Prof. Erik Verriest and Dr. Robert Lingle Jr. for serving on my Ph.D. committee. Their feedback on my research has been useful in improving both the content and presentation of this dissertation.

I am forever indebted to the late Dr. J.J. Werner of Bell Labs from whom I learnt the subtleties of equalization. I would like to thank my former colleagues in the Advanced Data Communications group of Bell Labs for the numerous discussions we had on both the theoretical and practical aspects of equalization when I worked there.

How do you really thank somebody who gave you life itself, nurtured you and inspired in you a lifelong passion for learning? However inadequate these words may be, I am grateful to my parents, Dr. Lalitha and Sri. B.G.K. Murthy, for everything.

This entire work would not have been possible without the constant support of my best friend, my beloved wife Aruna. She happily took upon herself the day-to-day running of the house, leaving me free to ponder the more intricate aspects of optical communications. Finally, my sons, Gnyana Bhaskar and Pragnya Tejas, have been a source of immense joy and happiness for me during this research.

TABLE OF CONTENTS

LIST OF TABLES

LIST OF FIGURES

SUMMARY

The widespread demand for data rates higher than 1 Gbps has resulted in the increasing use of multi-mode fiber (MMF) in local area networks, particularly because of its higher bandwidth compared to unshielded twisted pair wiring. Still the channel responses of 220-300 m MMF links operating at 10 Gbps span several bit periods because of the differential modal delay (DMD) of the various fiber modes, resulting in failure of over 80% of the links with conventional receivers. To achieve 10 Gbps or higher data rates and/or extended reach, the effects of the inter-symbol interference (ISI) in serial MMF links have to be mitigated.

The overall objective of this research is to propose low-complexity, electronic equalizers to increase the data rate and/or extend the reach of multi-mode fiber links, exploiting all the available diversity. We begin with a characterization of the MMF channel using a very robust mode solver that was developed as part of this research. This channel modeling tool is currently being used by the largest manufacturer of fiber in the world for its internal R&D work involving fiber design.

We then investigate the performance limits of conventional equalizers such as the linear equalizer (LE) and the decision feedback equalizer (DFE) in the context of MMF links. Although the electronic equalization of such links has been studied in the past, none of these efforts involved a thorough performance characterization based on comprehensive fiber models such as those discussed in this research. In fact, our work on the performance of finite-length DFEs helped in shaping the power budget discussion of the IEEE 802.3aq task force. However, the initial objective of extending the reach to 300m with a limited power budget and moderate complexity is unattainable even with a DFE.

To achieve this goal, we have investigated the use of the bidirectional DFE (BiDFE) in

MMF links. We have developed a new joint optimization technique that helps finite-length BiDFEs perform significantly better than even the infinite-length DFE and asymptotically approach the matched-filter bound. Furthermore, we show that given a limited number of filter taps, the BiDFE utilizes them better than a conventional DFE. In order to arrive at these results, we have developed techniques to estimate the performance of the BiDFE that circumvent the need for raw bit processing. We have also demonstrated that using BiDFEs the link can be extended to 350-400 m at a data rate of 10 Gbps.

Although the multiple modes of light propagation enable a multiple-input, multiple-output (MIMO) characterization of the MMF channel, this additional source of diversity has been largely ignored by the MMF community, with a few exceptions. In this research, we first determine the capacity bounds for MMF links when multiple transmit and receive "antennas" are present. We then apply a MIMO version of the DFE to mitigate the effect of ISI and co-channel interference (CCI). Comparative analysis indicates that MIMO processing allows increasing the data to 20 Gbps with a small increase in complexity.

One of the long-term objectives of the MMF community is to extend the reach to 1 km and beyond. In this research, we show that a proper assessment of the power penalty in MMF links necessarily requires a more comprehensive fiber model that includes mode coupling effects. Using our in-house mode coupling simulator, we show that ignoring coupling effects can result in an under-estimation of the penalty by as much as 1 dBo for 1 km MMF links employing DFEs.

CHAPTER I

INTRODUCTION

The first Ethernet based local area network (LAN), designed in 1973, operated at a modest data rate of 2.94 Mbps [1, 2] over coaxial cable. The subsequent increase in computing power and the associated demand for high speed LANs has driven Ethernet to support 10 Mbps, 100 Mbps and even 1 Gbps. With the availability of computers with pre-installed Gigabit Ethernet interfaces at a low cost, there is an urgent demand for at least 10 Gbps communication over the in-building cabling infrastructure.

At data rates higher than 100 Mbps, the significantly higher bandwidth of optical fiber makes it more cost effective compared to unshielded twisted pair (UTP) wiring that Ethernet has traditionally employed. Optical networks for metro-access and long-haul applications have employed single-mode fiber (SMF) because of its large bandwidth. But the high installation and maintenance cost of SMF networks resulting from the extremely restrictive tolerances for connectors and light coupling precludes its use in LAN applications.

The larger core area of multi-mode fiber (MMF) compared to SMF results in increased tolerance to alignment mismatches, thereby enabling its use in LANs. One main drawback of the larger core of MMF is that light propagates via a larger number of modes, each with its own group velocity. As a consequence MMF has lower bandwidth than SMF. However, the bandwidth of MMF is still sufficiently larger than that of copper cables to support data rates of 1 Gbps and higher with relative ease. For example, category-5 UTP cable has a usable bandwidth of about 100 MHz whereas MMF has a typical bandwidth of 10 GHz or more. As a result multi-mode fiber is the preferred transmission medium for most of the backbone cabling in modern office premises.

According to various surveys [3], approximately 85% of the MMF links are 300m or

Table 1.1: Reach as per IEEE 802.3ae-2002 10 Gbps Ethernet Standard for Multi-Mode Fiber.

PHY Name	Core Size (μm)	Wavelength (nm)	Serial or Parallel	Modal BW (MHz-km)	Reach (m)
10GBASE-S	50μm	850nm	Serial	400	66 m
				500	82 m
				2000	300 m
	62.5μm	850nm	Serial	160	26 m
				200	33 m
10GBASE-LX4	62.5μm	1310nm	Parallel: 4 λs	500	300m

shorter. Therefore, the objective of the MMF community is to increase the data rate to at least 10 Gbps and extend the reach of the link to at least 220m, if not 300m.

1.1 Reach Limitation in MMF Links

For 220m-300m long links at data rates of 10 Gbps and higher, even multi-mode fiber begins to exhibit dispersion effects. One of the parameters often used by multi-mode fiber manufacturers to characterize this effect is the modal bandwidth of the fiber. This is essentially the product of the 3 dB bandwidth of the fiber and its length. Table 1.1 lists the modal bandwidths and the implied reach of MMF links at 10 Gbps as specified by the IEEE 802.3ae-2002 standard [4]. The 10GBASE-S PHY sublayer specifies serial operation at 10 Gbps at a nominal wavelength of 850nm over both 50μm and 62.5μm core MMF. While modern 50μm core MMF with a modal bandwidth of 2000 MH-km can support 10 Gbps over 300m long links, a majority of the installed fiber base consists of 62.5μm core MMF [3]. In this case the reach is restricted to about 33m at 10 Gbps. A longer reach of about 82m can be supported at 1310nm over 62.5μm core MMF since it has a higher modal bandwidth (500 MHz-km) at this wavelength.

While a parallel solution employing four transceivers operating over different wavelengths was standardized to achieve a reach of 300m (10GBASE-LX4), the associated costs of the system are significantly higher. So if we restrict ourselves to serial transmission at

1310nm over 300m of 62.5μm core MMF, then the channel impulse response is likely to result in inter-symbol interference (ISI) that spans several bit periods. Receivers traditionally used in MMF links simply sample the received waveform (after photodetection) at the bit rate and then threshold the result to arrive at an estimate of the transmit bit. Therefore, achieving the stated goal of 10 Gps serial transmission over 220-300m of 62.5μm at 1310nm with conventional receivers may not be possible on a majority of the links.

A more detailed investigation of the performance limitations of conventional receivers based on a comprehensive fiber model is presented in Chapter 2.

1.2 Mitigation of Dispersive Effects in MMF Links

The objective of this research is to investigate low-complexity, efficient electronic equalizers to increase the data rate and/or extend the reach of multi-mode fiber links. Several techniques for mitigating the effects of ISI in serial MMF links have been proposed in the past [5–14]. These approaches can broadly be categorized into optical and electronic techniques along with a combination of these approaches.

The optical approaches [5–7] involve optical processing either at the transmitter or at the receiver such that the conventional receiver sees a channel response with limited ISI. These optical approaches typically involve a subtle trade-off between dispersion and loss which will still impact the overall power penalty. For example, the technique proposed in [5] uses single-mode fiber at both ends of the multi-mode fiber to launch and receive a restricted set of fiber modes. While this method reduces modal dispersion, the loss associated with the power in the higher-order modes that are rejected by the receiver, can be significant.

Electronic equalization has been commonly used in wireline and wireless channels for over three decades to mitigate the effects of ISI [15]. These electronic techniques have several advantages over the optical approaches. Historically, the manufacture, installation and maintenance of optical components have not realized the economies of scale that purely electronic solutions using conventional CMOS processing have traditionally achieved. Another advantage of electronic processing is the inherent adaptability to the wide variation in the response of different fibers and launch conditions as well as the slowly time-varying nature of the channel response. Furthermore, electronic solutions can be implemented in small form factors.

In view of these advantages, it was only natural for various researchers to investigate the impact of such techniques on the MMF channel [8–14]. These efforts primarily focus on the linear equalizer (LE), also known as the feed-forward equalizer (FFE), and the decision feedback equalizer (DFE). While the optimum receiver, the maximum likelihood sequence estimator (MLSE), yields superior performance, its complexity is exponential in channel memory[1] [15]. On the other hand, sub-optimal equalizer architectures such as the FFE and the DFE improve performance significantly at a complexity that is linear in channel memory [15].

Indeed, the IEEE 802.3aq task force [16] has decided to employ receiver-based electronic dispersion compensation (EDC) to extend the reach of 10 Gbps serial MMF links to 220m. In fact, our work on the performance of finite-length equalizers was instrumental in shaping the power budget discussion of the IEEE 802.3aq task force [11, 17–19].

A thorough analysis of the performance of both infinite and finite-length FFEs and DFEs for MMF links is discussed in Chapter 3.

1.3 Low-Complexity Equalizers: the BiDFE

As we show in Chapter 3, the DFE needs to have significantly large number of filter taps to achieve reliable transmission over 220m links at 10 Gbps. Therefore, another objective of this research is to explore low-complexity receiver structures that result in better performance than the DFE.

---

[1] Channel memory is the number of bit periods the ISI spans

One low-cost generalization of the DFE, the bidirectional DFE (BiDFE), has the potential to out-perform the DFE [20, 21]. We investigate the use of the BiDFE in the context of MMF links. We develop a new joint optimization technique that helps the BiDFE perform significantly better than even the infinite-length DFE and asymptotically approach the matched-filter bound.

We exploit the superior performance of the BiDFE in two different ways. Firstly, we show that given a limited number of filter coefficients, the BiDFE utilizes them better than a conventional DFE [22, 23]. Secondly, given the same number of taps, the BiDFE can support longer MMF links at 10 Gbps [23]. These results are presented in Chapter 4.

1.4 Multiple-Input, Multiple-Output (MIMO) Processing of MMF Links

Although 10 Gbps transmission over MMF links is challenging, there is already a push for higher data rates, even as high as 100 Gbps [24]. The most common approach being discussed is parallel transmission where a ribbon cable with ten fibers, each supporting a serial data rate of 10 Gbps, will be employed. While putting together such a system is relatively easy, it is likely to be expensive. Before embarking on a parallel solution, a fundamental question needs to be addressed. Has the upper limit of transmission over a single multi-mode fiber been reached?

Closer examination of propagation in MMF links indicates that the different fiber modes, which are orthogonal to each other, can be exploited to significantly increase the data rate. In principle, this can be accomplished by transmitting a separate data stream via each mode and detecting it separately at the receiver. Although similar multiple-input, multiple-output (MIMO) processing of the MMF link was proposed in [25, 26], the scheme involved coherent detection at the receiver. On the other hand, the effort in [7, 27–36] exploited the spatial diversity of these modes to reduce ISI in direction-detection MMF links by using a two-segment photodetector. More recently, we have proposed using dual launches at the transmitter and a two-segment photodetector along with MIMO equalization at the receiver to increase the data rate [37].

In order to establish the potential benefits of such a MIMO scheme over conventional transmission, we determine the Shannon capacity bounds of MMF links when multiple launches and multi-segment photodetectors are utilized. A lower bound for the capacity of intensity modulated optical channels is discussed in Chapter 5. We then investigate the impact of the MIMO version of the DFE (MIMO-DFE) to improve the performance of such multiplexed MMF links. These results are presented in Chapter 6.

1.5 Equalization of Long Fibers: Mode Coupling Effects

One of the long-term objectives of the MMF community is to extend the reach to 1 km and beyond [38]. Random micro-bends along the length of the fiber result in exchange of power between the propagating modes. Such mode coupling can significantly impact the channel response. In this research, we show that a proper assessment of the power penalty in MMF links necessarily requires a more comprehensive fiber model that includes mode coupling effects, particularly when evaluating the equalizer performance on long fibers [39]. To this end, we determine the effect of ignoring mode coupling effects in multi-km fibers. These results are presented in Chapter 7.

1.6 Note on the tone of the Thesis

Before we delve into the details of modal dispersion and ways to mitigate its effects, we point out that communication over optical fiber has been possible through the untiring efforts of numerous physicists and electrical engineers with an optics background. It is only in the last 3-4 years that communications engineers and researchers have started applying techniques traditionally used in wireline and wireless communications to MMF channels. Since this research straddles the worlds of communications and optical fiber, a more tutorial nature of treating various concepts from both domains has been adopted. The hope is that such an expository style of writing makes the thesis and the research results contained therein accessible to researchers and engineers from both domains.

CHAPTER II

FIBER MODELING AND CONVENTIONAL RECEIVERS

As stated earlier, the objective of this research is to investigate low-complexity, efficient electronic equalizers to increase the data rate and/or extend the reach of multi-mode fiber links. Before we discuss ways to mitigate ISI, we need a detailed understanding of the multi-mode fiber channel. In this chapter, we provide a brief overview of a multi-mode fiber model that we will utilize throughout this research. One of the key contributions of this research, a robust mode solver that can analyze MMF links with arbitrary profiles and launch conditions, is then briefly discussed. Subsequently, we characterize the performance of conventional receivers.

2.1 Modal Dispersion

The large core diameter of multi-mode fiber, typically 62.5μm, permits the propagation of multiple modes each with its own group velocity, Fig. 2.1. Although the ray picture of mode propagation is depicted for illustration purposes, these modes are the unique solutions of Maxwell's equations as applied to the refractive index profile of the MMF core and cladding regions. For the 62.5μm fiber at an operational wavelength of 1300nm, there are approximately 100 modes. These modes can be classified into mode groups, defined by the common phase velocity of the constituent modes [40]. There are approximately 18 mode groups for the example considered. Henceforth, we will discuss the propagation characteristics of MMF links in terms of these mode groups rather than the individual modes.

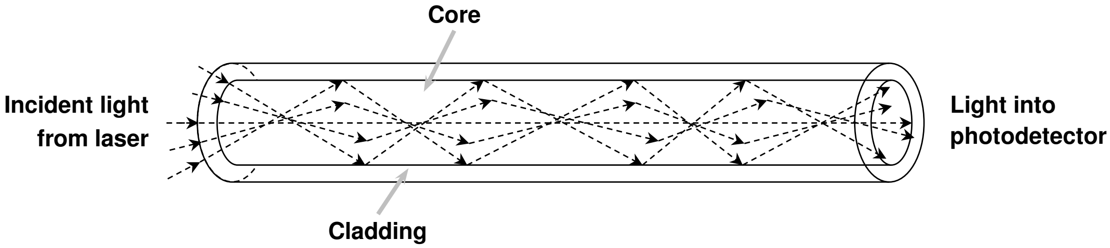

Figure 2.1: Light propagation in multi-mode fiber: a ray propagation perspective

2.1.1 Graded-Index Fiber

These mode groups have different group delays and so a pulse launched at one end of the multi-mode fiber arrives at different times at the far end. The most common approach to minimizing this delay spread is to use the graded refractive index profile, $n(r)$:

$$n(r) = \begin{cases} n_{\mathrm{co}}\sqrt{1-2\Delta\left(\frac{r}{a}\right)^{\alpha}} & 0 \le r \le a \\ n_{\mathrm{cl}} & r > a \end{cases} \tag{2.1}$$

where a is the core radius, $\Delta = (n_{\mathrm{co}}^2 - n_{\mathrm{cl}}^2)/(2n_{\mathrm{co}}^2)$, n_{co} is the maximum refractive index of the core, and n_{cl} is the refractive index of the cladding. Referring to the ray picture of light propagation (Fig. 2.1), such a pure α profile intentionally slows down the rays traveling along the fiber axis compared to the off-axis rays. Since the on-axis rays travel a shorter distance compared to the off-axis rays, the overall delay spread is reduced. Multi-mode fiber with such an index profile is known as *graded-index fiber*.

2.2 Index Perturbations: Modeling the Installed Fiber Base

Although fiber manufacturers try to achieve the pure alpha profile, process limitations result in small deviations. Figure 2.2 shows various index profile perturbations. In fact this set of perturbations, comprising 108-fibers, was first created by researchers at the University of Cambridge [41] and further modified by the IEEE 802.3aq task force [42]. The almost quadratic shape in Fig. 2.2 corresponds to the pure alpha profile with a nominal value of

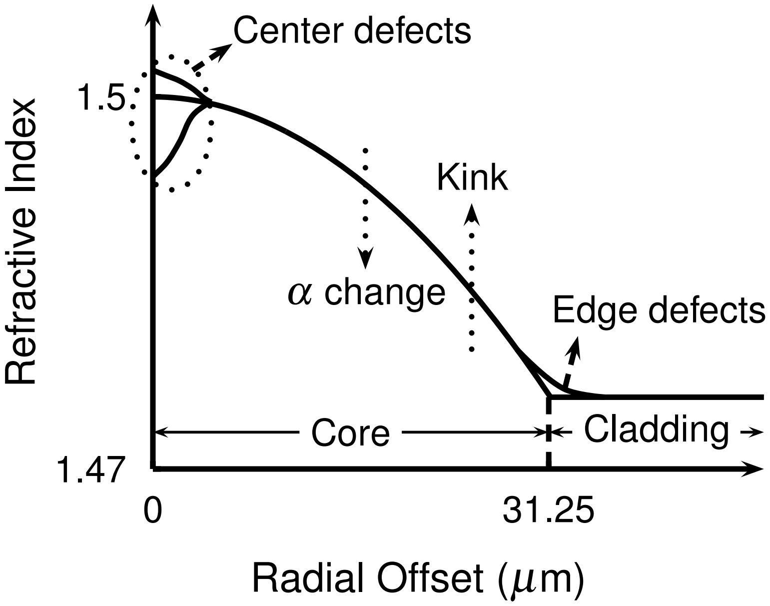

Figure 2.2: Refractive index profile perturbations considered in the 108-fiber model. These perturbations can be classified into center defects, α changes, kinks and core/cladding edge defects.

$\alpha = 1.97$. Sometimes the α of the profile can vary across the fiber cross-section. The 108-fiber model divides the core region into two halves, each of which can independently have $\alpha = 1.89, 1.97, 2.05$. In addition to the nominally smooth α profile at the center, dips and peaks are also observed in practice. The transition at the core and cladding interface can be abrupt or exponentially smooth. The final defect considered in the 108-fiber set is the kink which is effectively a perturbation in the gradient of the refractive index profile. The model considers both kink-free profiles and kinks at different locations. The model arrives at a total of 108 index profiles by considering all possible combinations of these perturbations. The parameters of these index perturbations are specified in [42].

Another widely prevalent fiber model is the Monte Carlo fiber set [43], which consists of approximately 5000 fibers whose modal delays are determined by empirically matching randomly generated delays to statistics of measured fiber parameters such as bandwidth and delay spread. The data about these measured fibers was provided by the top three fiber manufacturers in the world.

The 108-fiber set is considered to represent the worst 5% of the installed fiber base [41] whereas the Monte Carlo model is supposed to be representative of the entire installed base. The validity of both claims was highly debated in the IEEE 802.3aq task force discussions. Although the 108-fiber set was initially used by the task force, the final power budgets and the receiver test impulse responses determined by the IEEE are based on the Monte Carlo fiber set. This is partly because the Monte Carlo set is indirectly based on fiber measurement data.

Although we have used both models in our research, we will report the results based only on the 108-fiber set in this thesis. The main reason is the availability of refractive index profiles representing a diversity of challenging fibers. Some of the communication techniques proposed in this thesis specifically require the index profiles so that appropriate link responses can be generated. Although we could have used the Monte Carlo model where possible and the 108-fiber set in the remainder of the thesis, a fair comparison of the different receiver algorithms would not be possible in that case.

2.3 Modal Delays

Although the pure alpha profile minimizes the delay spread, actual fibers with these non-ideal refractive index profiles exhibit considerable delay spread in practice. Figure 2.3 illustrates this effect by showing the modal delays for the pure alpha profile, the center dip profile, the center peak profile and finally a fiber with a kink in its refractive index profile. These perturbations have been chosen from the 108-fiber model. Although one cannot predict how the modal delays for a particular profile will behave without detailed simulations, the general trends can sometimes be estimated. For example, the center dip profile implies that the mode groups propagating closer to the axis, the lower-order mode groups (LOMs), travel faster than the mode groups away from the axis, the higher-order mode groups (HOMs). Therefore, the modal delays should increase with mode group in general, as verified by Figure 2.3.

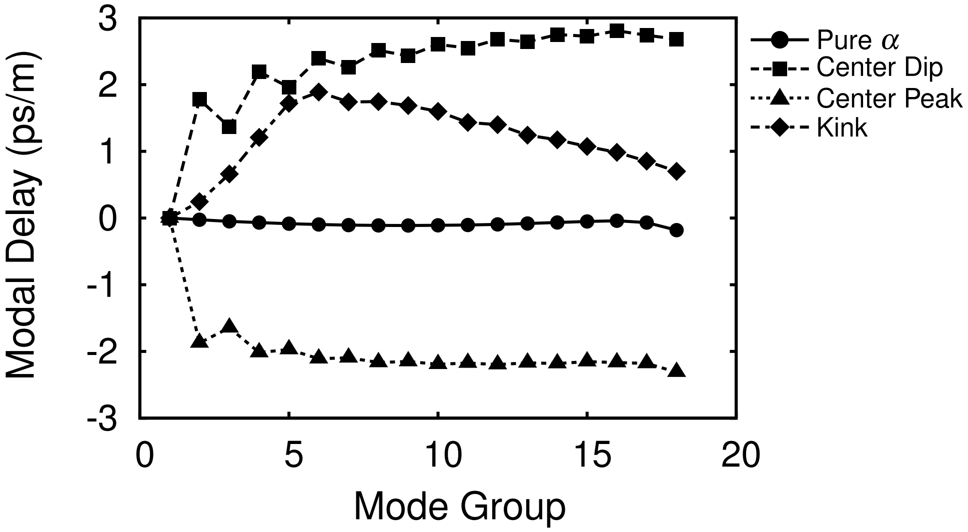

Figure 2.3: Relative modal delays for four illustrative fibers. All the delays have been normalized with respect to the lowest order mode group. The modal delays show a strong dependence on the refractive index profile.

2.4 Linearity of Fiber Response

The propagating electric fields are collected by the photodetector at the far end of the MMF link. Since the photodetector is typically modeled as a memoryless, square-law device, the linearity of the end-to-end link may be suspect. It can be shown that the electric fields corresponding to the different propagating modes are orthogonal to each other [40]. So the square-law detector results in the addition of the received optical power in each mode.

For a typical MMF link, the chromatic dispersion of each mode is negligible. Therefore, the square-law detector does not introduce any non-linear inter-symbol interference (ISI) for the individual modes. As a consequence, the end-to-end MMF link is linear [44], with the differential modal delay (DMD) being the only source of pulse dispersion.

A typical link consists of two connectors near the transmit end. Sometimes due to connector offsets the orthogonality of the modes may not be exact. Random micro-bending of the fiber may result in mode coupling which also impacts mode orthogonality. The absence of complete orthogonality among the received modes is mitigated by the use of low coherence sources [44]. Thus a linear model of the end-to-end system is still valid.

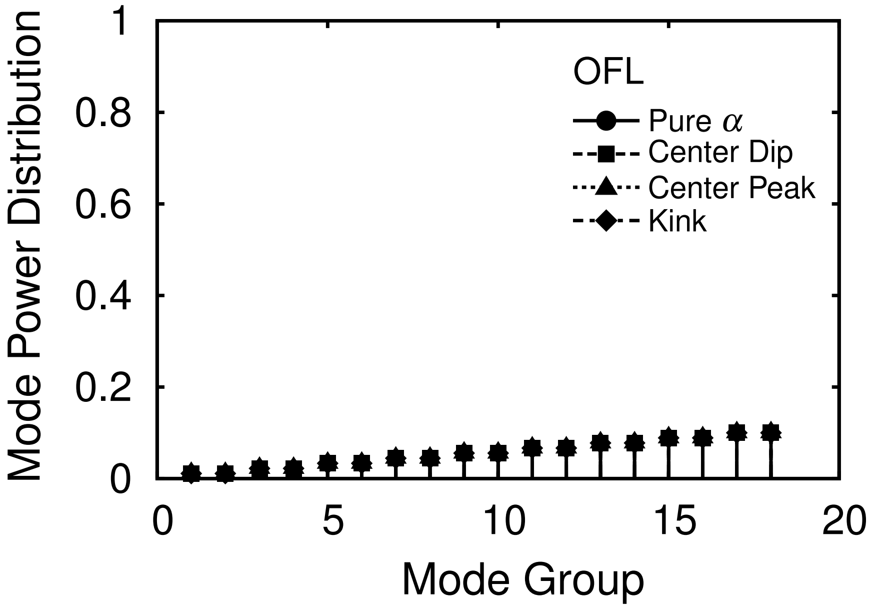

Figure 2.4: Mode power distribution for LED based over-filled launch (OFL).

This linear formulation assumes that the transmit data sequence modulates the output intensity and not the electric field. Such links are therefore known as *intensity-modulated, direct-detection* links.

2.5 Launch Condition and Mode Power Distribution

In view of the linearity of the link, the fiber impulse response is simply given by the modal delays and the relative optical power coupled into each mode. The power in each mode, also known as the *mode power distribution* (MPD), is determined by the manner in which light is launched into multi-mode fiber.

Light emitting diodes (LEDs) were the predominant light source in the early days of communication using multi-mode fiber. These sources typically excited all the propagating modes of the fiber to an equal extent. Such a launch, known as over-filled launch (OFL), results in the mode power distribution shown in Fig. 2.4. Since the higher-order mode groups have more modes, they transport more power compared to the lower-order mode groups.

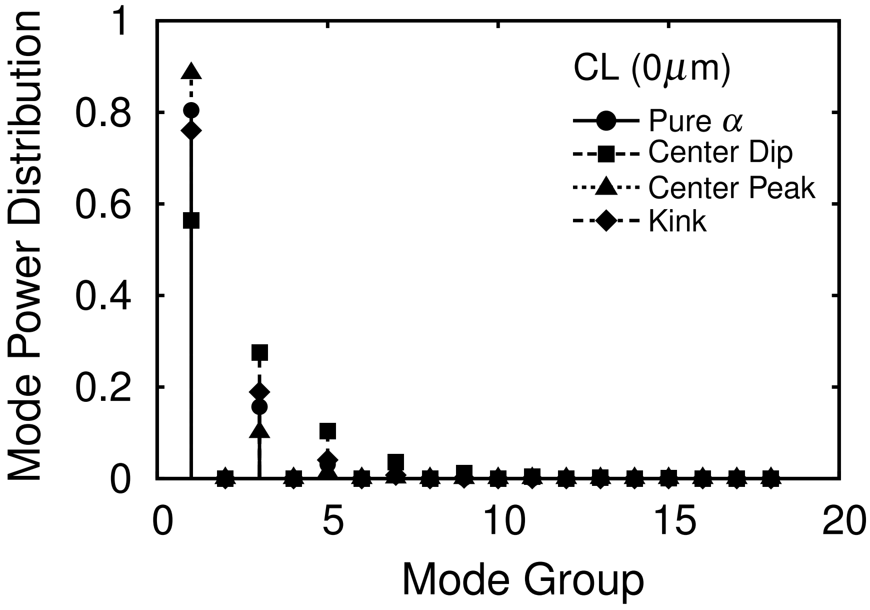

Figure 2.5: Mode power distribution for laser based center launch (CL): 0 μm.

Since multi-mode fiber links use directly modulated light sources to keep system costs low, the switching speed of LEDs became a limitation as the data rates increased to 1 Gb/s and higher. This issue was overcome by using lasers as the light sources. In the most common configuration the laser is aligned with the multi-mode fiber axis. Such a launch, known as *center launch* (CL), typically excites only the lower-order modes as illustrated in Fig. 2.5. Although the laser is nominally aligned with the fiber axis, a tolerance of ± 3 μm is typically allowed.

The fact that only a subset of the fiber modes is excited by center launch is not a problem by itself. But when the lower-order modes have a larger delay spread (Fig. 2.3), the resulting impulse response spans several bit periods. For these illustrative fibers, the intermediate to higher-order mode groups have a much smaller delay spread compared to the LOMs. Therefore, a narrower fiber response is obtained by using a mode-conditioning patch chord to offset the laser with respect to the fiber axis. For a 62.5 μm fiber, this offset is nominally set to 20 μm with a tolerance of ± 3 μm. The mode power distribution for this launch, known as *offset launch* (OSL), is shown in Fig. 2.6. Interestingly, the four different

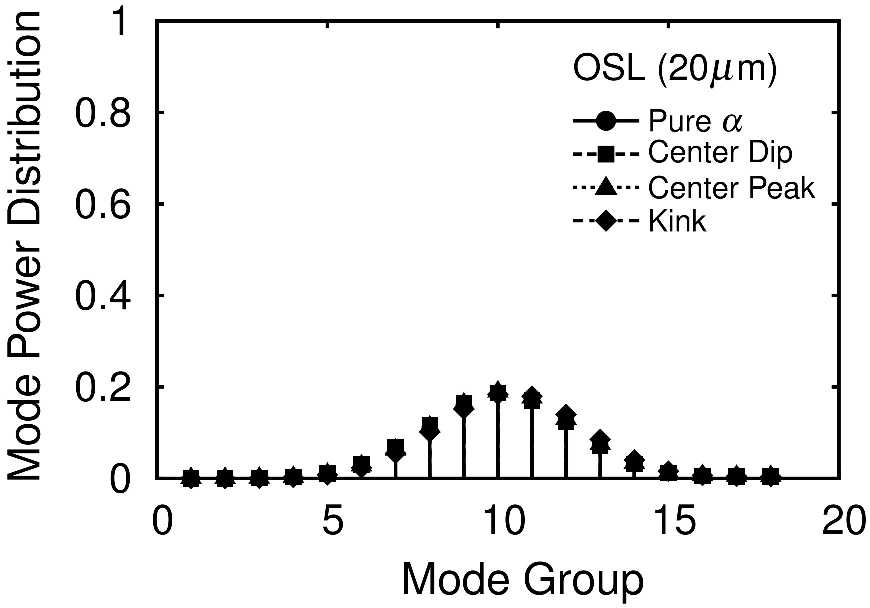

Figure 2.6: Mode power distribution for laser based offset launch (OSL): 20 μm.

refractive index profiles yield almost idential MPDs for offset launch.

The mode power distribution is computed via the overlap integral between the excitation electric field and the electric fields corresponding to the various propagating modes. For laser launch via the patch cord, the incident field is modeled as a Gaussian beam with a full-width half-maximum (FWHM) of 7 μm.

It has been observed that the mode power distribution is relatively independent of the refractive index profile but varies strongly with the launch condition. In fact, the Monte Carlo fiber model assumes that the MPD for the pure alpha profile at a given launch can be applied to all the other perturbed profiles for the same launch.

2.6 Georgia Tech Mode Solver

Prior to this research, a rudimentary multi-mode fiber simulator was being used at Georgia Tech [45]. Since it could handle only the pure alpha profile, it was of limited utility in assessing the performance of practical MMF links.

As part of this research, we have developed a robust mode solver that can determine the

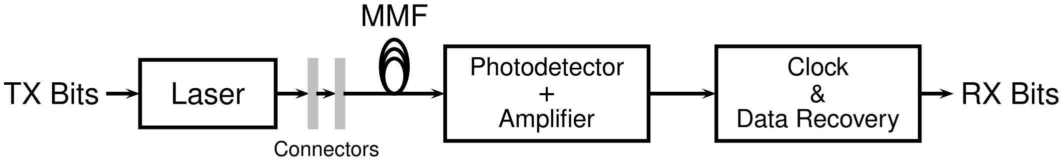

Figure 2.7: End-to-End configuration of a typical multi-mode fiber based communication link.

modal delays and the mode power distribution, given an arbitrary refractive index profile and launch condition. Furthermore, the simulator can be configured to operate at different wavelengths. The scalar wave equation, which governs the radial part of the propagating electric field, is solved by a finite-difference method. The Rayleigh quotient approach is used to solve for the modal delays. Since the main focus of this research is on equalization techniques for the MMF channel, we will not go into the details of our mode solver further.

Through comparisons with analytical expressions of modal delays for simple refractive index profiles, we have found our simulator to be more accurate than commercially available multi-mode fiber simulators. We have also validated our simulator against results from other research groups around the world. Our MMF link simulator is currently being used by the largest manufacturer of fiber in the world for its internal research and development work. The modal delays, MPDs, and impulse responses shown in this research have all been generated using our MMF simulator.

2.7 End-to-End Link Modeling

The end-to-end multi-mode fiber link comprises the data source that modulates the laser, the connectors in the link, the fiber itself, the photodetector along with the trans-impedance amplifier (TIA), and the clock and data recovery unit, Fig. 2.7. The equivalent mathematical representation of the link up to the input to the clock and data recovery unit is shown in Fig. 2.8.

Since MMF-based LANs have always used NRZ signaling together with a directly modulated laser, a good model for the transmit filter is the NRZ pulse shape with a finite

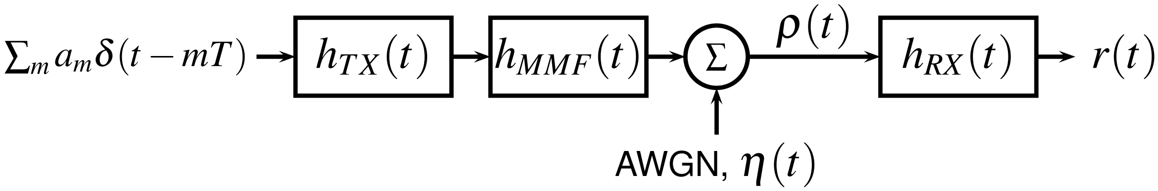

Figure 2.8: Mathematical representation of the end-to-end link.

rise-time $h_{TX}(t)$. In the case of 10Gb/s operation a rise-time $(20\% - 80\%)$ of 47.1 ps is used. Note that throughout this thesis T denotes the bit period, which for exactly 10 Gbps operation is 100 ps[1].

As mentioned earlier, the typical link has two connectors near the transmit end of the fiber. They are modeled by a simple power exchange between the different mode groups based on the connector offset [46]. The offset for each connector is modeled by a Rayleigh distribution with a mean of 3.58μm and a worst-case offset of 7μm. Depending on the effect being discussed, we will sometimes use ideal connectors with 0μm offset each. Note that the IEEE 802.3aq task force recommends that the worst-case offset of 7μm per connector be used with the 108-fiber model whereas the truncated Rayleigh distribution be used with the Monte Carlo model. This is in part due to the fact that the 108-fiber set is considered to represent the worst 5% of the installed fiber base. Therefore, any set of worst-case fibers should also include the worst-case connector offsets. The impulse response of the multi-mode fiber including any connector effects is represented by $h_{MMF}(t)$ in Fig. 2.8.

After square-law detection, the photocurrent passes through a trans-impedance amplifier which has a band-limited response given by a fourth order Bessel-Thomson filter, $h_{RX}(t)$ in Fig. 2.8. The 3-dB bandwidth of this filter is 7.5 GHz for 10 Gb/s operation.

The main source of noise in the link, $\eta(t)$, is the thermal noise of the amplifier, which is typically modeled as an additive, white, Gaussian process with power spectral density $N_0/2$.

---

[1] Strictly speaking, 10 Gbps Ethernet MMF links operate at 10.3125 Gbps resulting in $T = 96.97$ ps.

The models and parameters for each of these blocks are consistent with those used by the IEEE 802.3aq task force in its standardization efforts [16].

2.8 *Link Impulse Responses*

Since all the constituent blocks of the end-to-end link are modeled as linear filters, a simple convolution of the individual responses, $h_{TX}(t)$, $h_{MMF}(t)$, $h_{RX}(t)$, yields the link impulse response, $h(t)$:

$$h(t) = h_{TX}(t) \bigstar h_{MMF}(t) \bigstar h_{RX}(t) \tag{2.2}$$

$$r(t) = \sum_m a_m h(t - mT) + \underbrace{\eta(t) \bigstar h_{RX}(t)}_{v(t)} \tag{2.3}$$

where $\bigstar$ denotes the convolution operation.

As mentioned earlier, the objective of the MMF LAN community is to achieve a reach of 220m or better at a data rate of 10 Gbps. Figure 2.9 shows the impulse responses for our four illustrative fibers for such a link with center launch. Clearly, the link response varies strongly from fiber to fiber. In addition, the impulse response can span anywhere between one and six bit periods at 10 Gbps. We note that the inter-symbol interference can be either pre-cursor[2] ISI or post-cursor[3] ISI. Specifically, *without connectors* the fiber with the center peak exhibits pre-cursor ISI whereas the center dip fiber shows post-cursor ISI, Fig. 2.9a. But *with connectors* the ISI for the center peak fiber changes to the post-cursor type, Fig. 2.9b. Note that the worst-case offset of 7μm per connector has been used to generate the responses with connectors.

The offset launch link responses are shown in Fig. 2.10. With the 20μm launch, the very same fibers are much more well-behaved with the response limited to a maximum of three bit periods without connectors. Although connectors do impact the link response with offset launch, their effect is much less dramatic compared to center launch. This is largely

---

[2] Pre-cursor ISI: Significant energy present before the main peak of the response

[3] Post-cursor ISI: Significant energy present after the main peak of the response

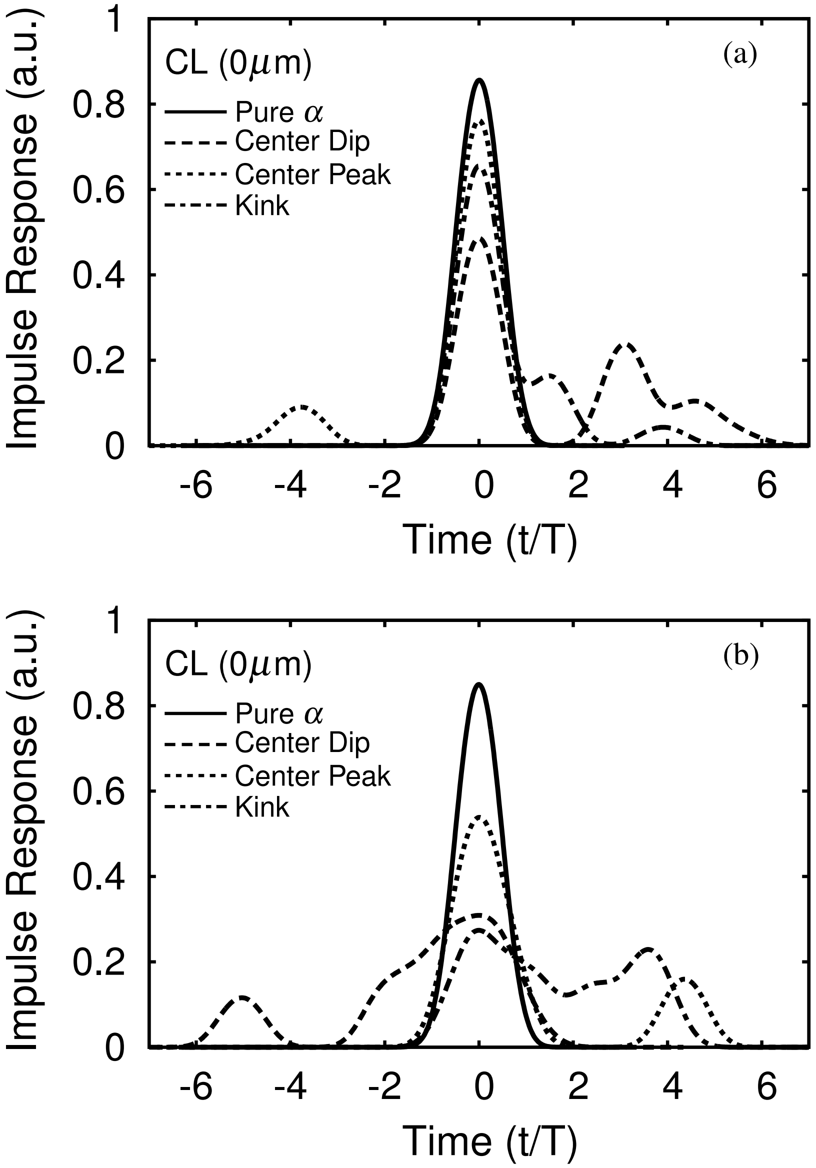

Figure 2.9: Impulse responses for 220m links with center launch: (a) Without connectors and (b) With connectors. The time axis has been centered with respect to the main peak and then normalized with respect to the bit period at 10 Gbps.

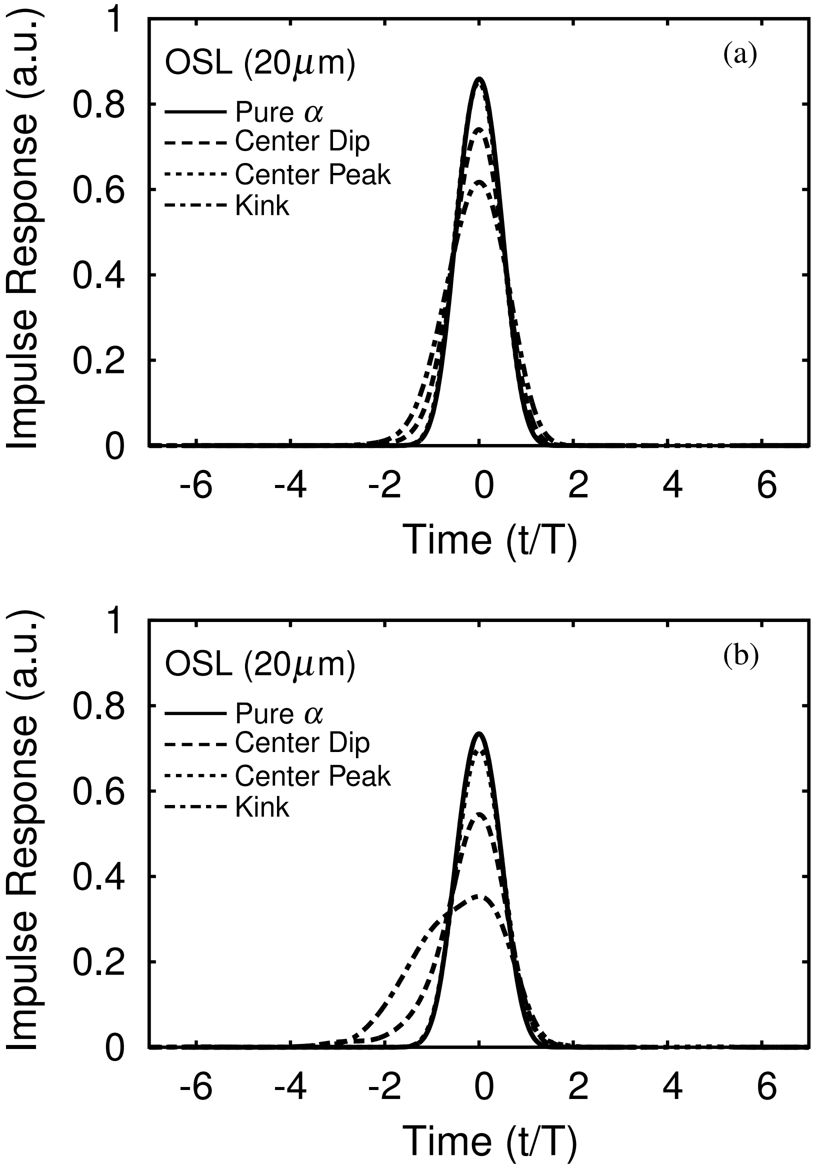

Figure 2.10: Impulse responses for 220m links with offset launch: (a) Without connectors and (b) With connectors. The time axis has been centered with respect to the main peak and then normalized with respect to the bit period at 10Gbps.

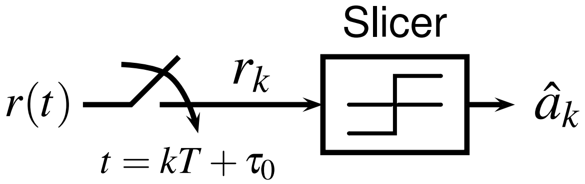

Figure 2.11: Mathematical model of the conventional receiver.

due to the higher number of mode groups with a comparatively smaller delay spread getting excited with offset launch. Therefore, although power is exchanged between these mode groups, the signal energy mostly occupies the same time slots as before the power transfer.

2.9 Power Penalty Estimation for the Conventional Receiver

We have thus far not discussed the functionality of the clock and data recovery unit in Fig. 2.7. This unit implements the only electronic processing currently employed in installed MMF links. It samples the output of the trans-impedance amplifier at the optimal sampling instant and then thresholds the result to arrive at its estimate of the transmit bit, Fig. 2.11. Note that τ_0 is the sampling instant chosen by the clock and data recovery unit and lies in the interval $[0, T]$. Such a receiver shall be known as the *conventional receiver* throughout this thesis. Note that such a simple receiver has been adequate for MMF links thus far, primarily because either the data rates were low (1 Gbps or lower [47]) or the reach was limited.

Keeping our objective of 220m reach at 10 Gbps in mind, we will first baseline the performance of the conventional receiver for such a link. The typical bit error rate (BER) requirement on MMF links is 10^{-12} or lower. Since MMF links do not use error control coding, this raw bit error rate needs to be satisfied by the signaling and detection scheme directly. Although measuring such error rates experimentally in the laboratory is trivial for 10 Gbps links, it becomes an astronomically time consuming pursuit if done numerically through simulations [4]. So the Monte Carlo methodology of performance characterization

---

[4] In order to reliably estimate a BER of 10^{-12} we need to process at least 10^{14} bits. Even if we process a

that is widely used for wireless and other wireline channels is not practical for MMF links. Therefore, we resort to estimation techniques to quickly but accurately determine the performance of MMF links. Although several different methods are discussed in the literature, we believe our method, described in Appendix A, achieves a good balance between speed and accuracy.

The input to the decision device of the conventional receiver, r_k, can be modeled as the sum of the desired signal, $h_0 a_k$, the residual ISI, q_k, and additive noise, ν_k :

$$r_k = h_0 a_k + \underbrace{\sum_{i \neq 0} h_i a_{k-i}}_{q_k} + \nu_k \tag{2.4}$$

where a_k is the transmit bit and h_k are the T-spaced samples of the end-to-end link response, $h(t)$. The noise samples, ν_k, form a correlated Gaussian process since they are samples of a filtered, white, Gaussian process. Since this discretized channel has the same form as that assumed in Appendix A, the BER estimation technique discussed therein can be directly applied.

2.9.1 Margin and Optical Power Penalty

The figure of merit that will be used throughout this thesis is the power penalty that the ISI channel suffers compared to the ISI-free case at a bit error rate of 10^{-12} or lower. Once the BER versus signal-to-noise (SNR) curve is available using the method described in Appendix A, this penalty can then be quickly determined. A quicker and more practical approach that is widely used in the industry is discussed next.

Figure 2.12 shows hypothetical bit error rate curves for an ISI channel along with that for the ISI-free case. The ISI-free curve achieves a BER of 10^{-12} at an SNR of γ_0. The relationship is governed by $P_e = Q\left(\sqrt{SNR}\right)$, where $Q(\cdot)$ is the well known Q-function [15].

In order to achieve the same performance, the ISI channel should operate at a much higher SNR. The maximum permissible SNR is determined by the power budget for the

---

million bits per second numerically, the entire task requires 10^8 seconds or about 3.2 years.

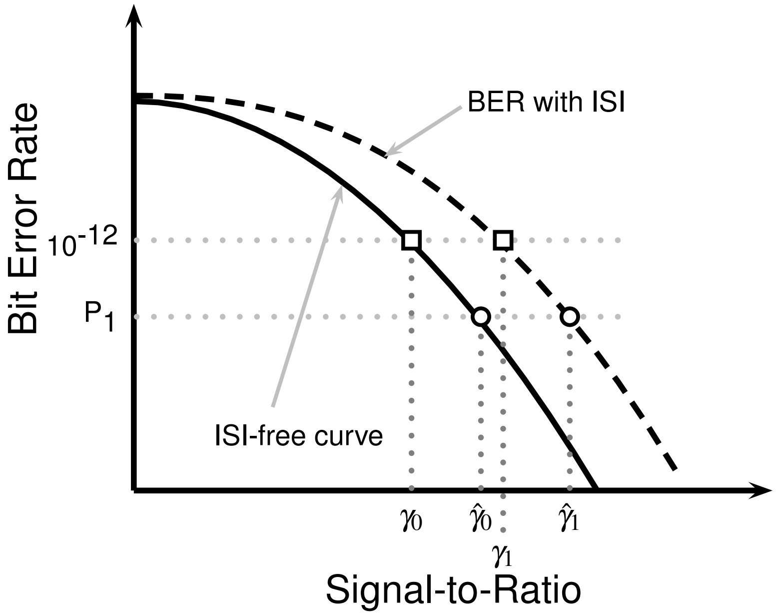

Figure 2.12: Margin and optical power penalty

link. For 10 Gbps operation over MMF links, the IEEE 802.3aq task force [16] has allocated a dispersion power budget, or margin, of 6.5 dBo[5]. This margin moves the operating SNR to $\hat{\gamma}_1$ from γ_0. At this SNR, the ISI channel achieves a BER denoted by P_1. The ISI-free curve will achieve this BER at an SNR denoted by $\hat{\gamma}_0$. Therefore, the power penalty compared to the ISI-free case is given by :

$$\text{Power penalty } = \hat{\gamma}_1 - \hat{\gamma}_0 \tag{2.5}$$

See Appendix B for more details about the ISI-free link.

While specifying the margin of the system, we have used the qualifier "dispersion" for the power budget. It indicates that fiber loss and loss resulting from connectors are not considered here.

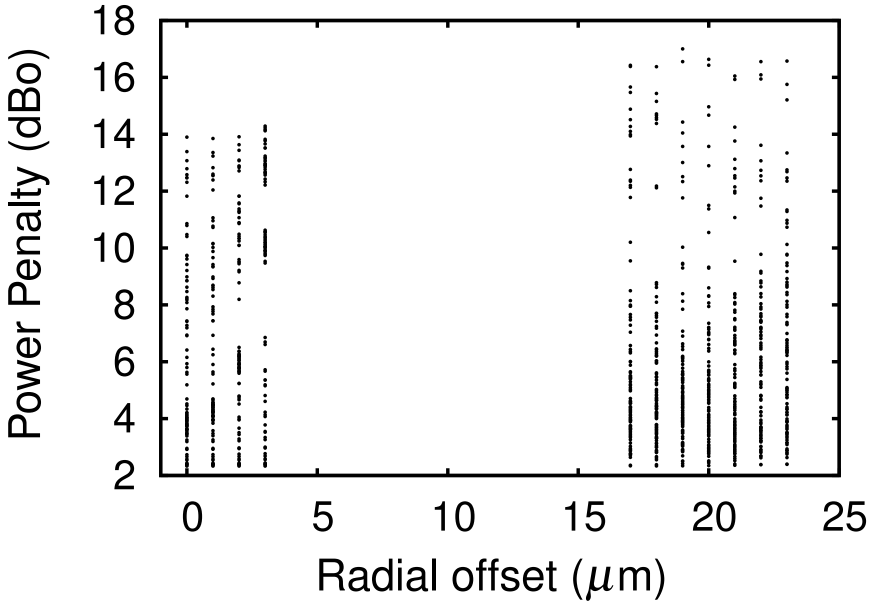

Figure 2.13: Variation of the optical power penalty with launch offset. The penalties correspond to a 10 Gbps, 220m long MMF link without connectors.

2.10 Conventional Receiver Performance

For the conventional receiver, we compute the optical power penalty for the 108-fiber set for 220m long MMF links operating at 10 Gbps using the techniques of the previous section. Figure 2.13 shows the scatter plot of the power penalty against the launch offset for the connector-less case. Clearly, the penalties can be as large as 17 dBo and as small as 2 dBo. Furthermore, both center and offset launches exhibit these wide variations in penalty.

Given that the allocated dispersion budget is only 6.5 dBo, it is clear that a large percentage of the 220m fibers cannot be operated at 10 Gbps. This type of statistical information is better illustrated through the *coverage curve*, which is the percentage of fibers with the penalty less than that given by the abscissa, Fig. 2.14a. The coverage curve for center launch is obtained by computing the cumulative distribution for the power penalty under the assumption that the offsets 0-3μm are equally likely. With the allocated maximum penalty of 6.5 dBo, only 58% of the 108-fiber set (without connectors) is useful for reliable

---

[5] dBo = optical dB. In general, dBo = 0.5×dBe where dBe = electrical dB.

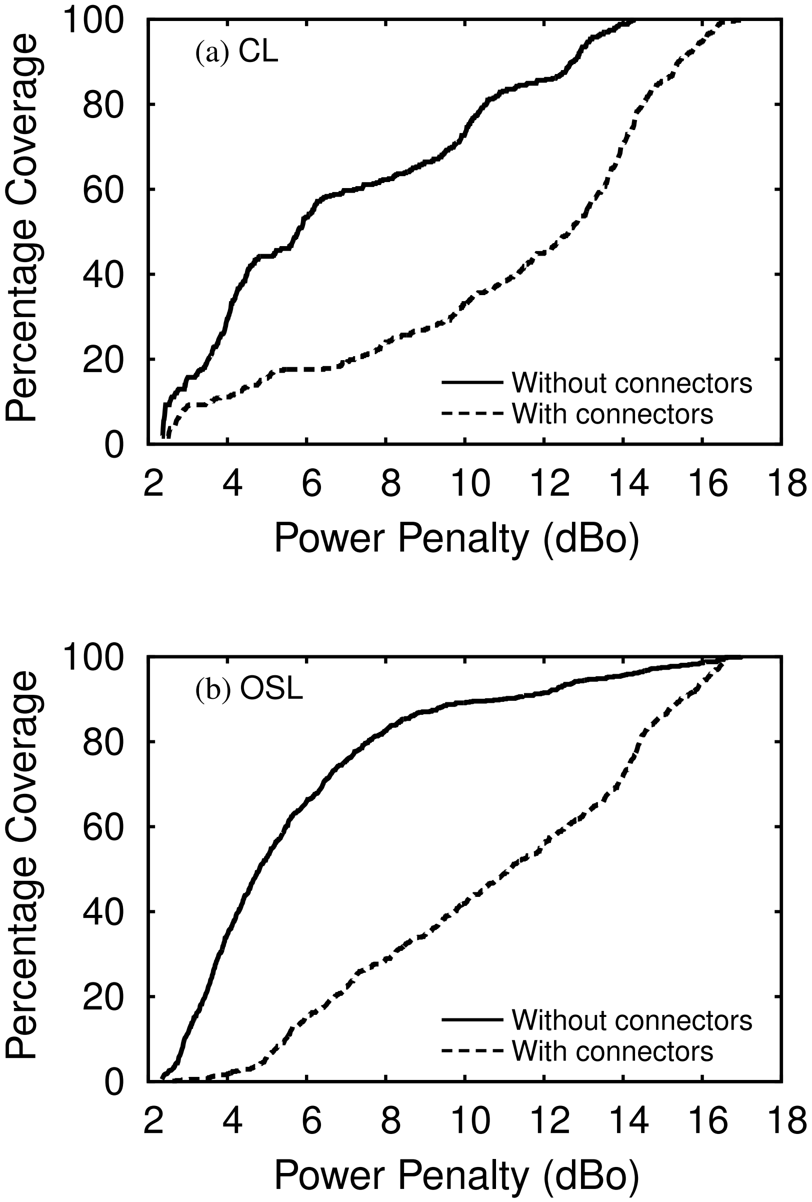

Figure 2.14: Coverage curves for 220m long MMF links operating at 10 Gbps: (a) Center launch (b) Offset Launch.

transmission at 10 Gbps. This coverage drops dramatically to 18% when connectors are added to the link.

Similarly, for offset launch the offsets 17-23μm are considered to be equally likely while computing the coverage curve, Fig. 2.14b. In this case, the 6.5 dBo margin achieves a coverage of 71% in the connector-less case and 18% with two connectors in the link.

It is standard practice to design communication transceivers to operate successfully over at least 99% of the channels. In fact, the IEEE regularly uses such a requirement while determining link power budgets during its standardization efforts. Clearly, such a coverage requirement is a strong function of the fiber model used. If the 108-fiber set, with its underlying assumption of being the worst 5% fibers, is used then the 80% coverage point of this model characterizes receiver performance. One of the problems with this approach is that the 5% estimate is based on differential modal delay statistics and not on the power penalty. On the other hand, if the Monte Carlo fiber set is used, then the 99% coverage point of this model determines receiver performance.

Comparisons of certain performance metrics for the 108-fiber set and the Monte Carlo fiber set indicate that there is some discrepancy between these two models [48]. For example, the 80% coverage point of the 108-fiber set does indeed correspond to the 99% coverage point of the Monte Carlo set. But this is only for offset launch when connectors are added to the link. If connectors are not considered, then the 93.5% coverage point of the 108 fiber set corresponds to the 99% coverage point of the Monte Carlo set. In the context of this thesis, we will use the 95% point of the 108 fiber set in the connector-less case and the 80% point when connectors are used. The implicit assumption is that both these data points correspond to the 99% of the installed fiber base.

For MMF links with connectors the conventional receiver has a penalty of 14.5 dBo with center launch and 14.4 dBo with offset launch at the 80% coverage point. Therefore, the conventional receiver cannot support 10 Gbps over 220m long MMF links and so we seek better ways to detect the transmitted bits in the presence of ISI.

CHAPTER III

DECISION FEEDBACK EQUALIZATION OF MMF LINKS

In the previous chapter, we saw that conventional receivers are unable to overcome the deleterious effects of modal dispersion. In this chapter, we employ linear and decision-feedback equalization to mitigate ISI effects in multi-mode fiber links. We characterize the performance of these receivers for 220m MMF links operating at 10Gbps. Performance of both infinite-length and finite-length equalizers is considered.

3.1 Conventional Equalization Architectures and Metrics

The optimum detector is the one that chooses the mostly likely sequence of transmit bits given the received waveform. Such a receiver, known as the maximum-likelihood sequence estimator (MLSE), is efficiently implemented via the Viterbi algorithm [49]. While the MLSE receiver has optimum performance, its complexity increases exponentially with channel memory. As a consequence, implementations at data rates of 10 Gbps are particularly challenging. Although some prototypes have been discussed in the literature in the context of single-mode fiber links, these MLSE receivers can handle only two bits of ISI [50]. Furthermore, the power consumption and cost of such optimal receivers cannot be justified in multi-mode fiber LANs, which operate at much lower price points compared to long-haul SMF links. Therefore, sub-optimal equalizers with complexity that is linear in channel memory are the focus of this research.

We begin with a brief overview of the various equalization architectures considered in this chapter. Optimization of the equalizer coefficients and some key performance metrics are also discussed.

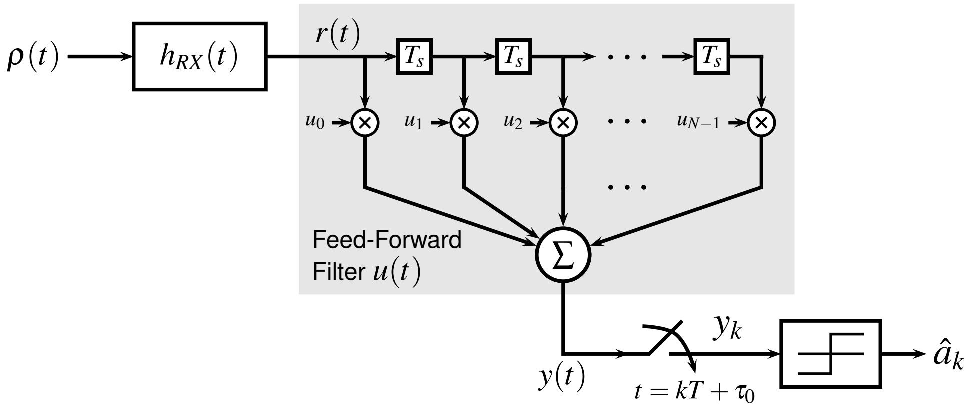

Figure 3.1: Structure of the fractionally spaced linear equalizer.

3.1.1 Linear Equalization

The simplest of electronic equalizer structures involves linear filtering of the received waveform and is known as the *linear equalizer* (LE) in the literature [15, 51], Fig. 3.1. It is also called the feed-forward equalizer (FFE). Delayed and appropriately scaled versions of the received waveform are combined by the linear equalizer. The corresponding output, $y(t)$, is sampled at the bit rate, $1/T$. The output of the sampler, y_k, is then processed by the slicer to arrive at an estimate of the transmit bit, a_k. Typically the tap spacing, T_s, is a fraction of the bit period, so such a receiver is also known as the fractionally spaced linear equalizer. The ratio $\beta = T/T_s$ is known as the fractional-sampling or the over-sampling rate. Practical equalizers use rational values of β, with $\beta = 2$ being very common. When $\beta = 1$, the equalizer is known as the T-spaced or the *baud-spaced equalizer*. One important reason why the fractionally spaced equalizer is preferred to the baud-spaced equalizer is the relative insensitivity of the former to the sampling phase τ_0 [52].

The most common technique to adjust the equalizer coefficients is minimum mean-square error (MMSE) equalization, where the energy of the error between the slicer input, y_k, and the corresponding transmit bit, a_k, is minimized.

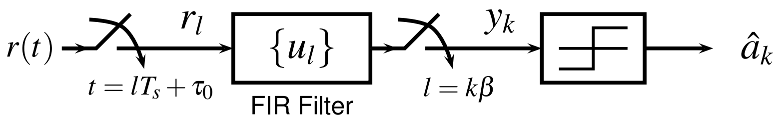

Figure 3.2: Equivalent digital implementation of the fractionally spaced linear equalizer.

Specifically,

$$e_k = y_k - a_k \tag{3.1}$$

$$\textit{Choose } \{u_l\} \textit{ to minimize } \xi \overset{\Delta}{=} E\left[e_k^2\right] \tag{3.2}$$

The minimum mean-square error for the optimum linear equalizer with binary signaling is given by [53]:

$$\text{Minimum MSE } = \xi_{LE} = T\int_{-\frac{1}{2T}}^{\frac{1}{2T}} \frac{N_0/2}{\frac{1}{T}\sum\limits_{l}\left|G\left(f-\frac{l}{T}\right)\right|^2 + \frac{N_0}{2\sigma_a^2}} df \tag{3.3}$$

where $G(f)$ is the Fourier transform of $g(t)$ and σ_a^2 is the variance of the transmit bits. For the multi-mode fiber link, the response up to the front-end filter is given by $g(t) = h_{TX}(t)\bigstar h_{MMF}(t)$, where $\bigstar$ is the convolution operation. Assuming e_k to be Gaussian with variance ξ_{LE}, we find that the power penalty for the infinite-length linear equalizer compared to the ISI-free case is given by :

$$\text{PIE-L} \overset{\Delta}{=} T\int_{-\frac{1}{2T}}^{\frac{1}{2T}} \frac{1}{\frac{1}{T}\sum\limits_{l}\left|G\left(f-\frac{l}{T}\right)\right|^2 + \frac{N_0}{2\sigma_a^2}} df \tag{3.4}$$

where PIE-L stands for *Penalty of Ideal Equalizer-Linear equalizer*. The quantity $N_0/(2\sigma_a^2)$ is chosen such that the MMF link is operating at a margin of 6.5 dBo from the noise power at which the ISI-free link has a BER = 10^{-12}. Further details related to the operating SNR are provided in Appendix B.

The FSE structure shown in Fig. 3.1 is an inherently analog implementation. An equivalent digital implementation is shown in Figure 3.2, where the $1/T$ sampler has been broken into two samplers, one operating at $1/T_s$ and another operating at $1/\beta$. The $1/T_s$ sampler

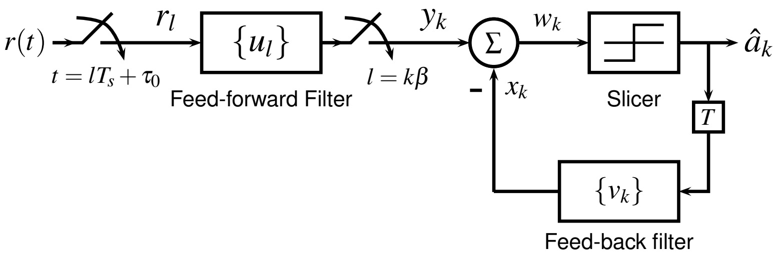

Figure 3.3: Structure of the decision feedback equalizer.

has then been moved to the input of the feed-forward filter. This digital implementation is the standard practice in wireline and wireless communications. Since its implementation at 10 Gbps is challenging, the analog implementation is the preferred approach for multi-mode fiber links. On the other hand, performance estimation using the digital structure is more convenient because of the reduction in the highest sampling rate in the system. Therefore, we will use the digital implementation to assess the performance of finite-length equalizers, although the results apply equally well to the analog FSE.

While the concept of linear equalization can be traced back to Nyquist [54, 55], the details of minimum mean-square optimization of the LE were provided by Berger and Tufts [53]. Automatic adaptation of the linear equalizer was first considered by Lucky [56].

3.1.2 Decision Feedback Equalization

In section 2.8 we saw that the inter-symbol interference can be of the pre-cursor and/or post-cursor type. Therefore, one can improve upon the performance of the linear equalizer by canceling the ISI from the past bits before making a decision about the present bit. One way such an estimate can be formed is by appropriately weighting the past decisions from the slicer. Such a receiver structure is known as the *decision feedback equalizer* (DFE), Fig. 3.3. The only difference from the linear equalizer structure is the feedback filter with T-spaced coefficients v_k that produces the estimate of the post-cursor ISI.

Unlike the linear equalizer case, the feed-forward filter is trying to equalize only the pre-cursor part of the ISI, leaving the post-cursor ISI for the feedback filter. Therefore, the additional noise enhancement that the LE had during post-cursor equalization is no longer present in the case of the DFE. Therefore, the DFE is expected to have better performance than the LE. The power penalty for the infinite-length DFE is given by :

$$\text{PIE-D} \triangleq \exp\left[-T\int_{-\frac{1}{2T}}^{\frac{1}{2T}} \ln\left\{\frac{1}{T}\sum_{l}\left|G\left(f-\frac{l}{T}\right)\right|^{2}+\frac{N_0}{2\sigma_a^2}\right\}df\right] \tag{3.5}$$

where PIE-D stands for *Penalty of Ideal Equalizer-Decision feedback equalizer*.

The decision feedback equalizer was proposed by Austin [57] while an explicit formula for its minimum mean-square error was derived by Salz [58].

3.2 Infinite-length Equalizer Performance for MMF Links

In this section, we determine the coverage curves for the infinite-length linear and decision feedback equalizers, Fig. 3.4. These results serve to illustrate the best performance that can be achieved using such receiver architectures. The MMF links are 220 m long with two connectors and are operated at a data rate of 10 Gbps. The power penalties for the infinite-length LE and the DFE have been computed using (3.4) and (3.5) respectively. As expected the optimum DFE performs significantly better than the infinite-length LE. In fact, at the 80% coverage point, links with the DFE require about 2 dBo (= 4 dBe) less power than those employing the LE, Table 3.1. Furthermore, using either equalizer improves performance by more than 7 dBo compared to the unequalized links.

Table 3.1: Optical power penalty at the 80% coverage point for links with no equalizer, with LE and with DFE. Each link is 220 m long with two connectors and is operated at 10 Gbps.

Equalizer	Center Launch	Offset Launch
Unequalized	14.5 dBo	14.4 dBo
Infinite-length LE	7.1 dBo	7.5 dBo
Infinite-length DFE	5.1 dBo	5.3 dBo

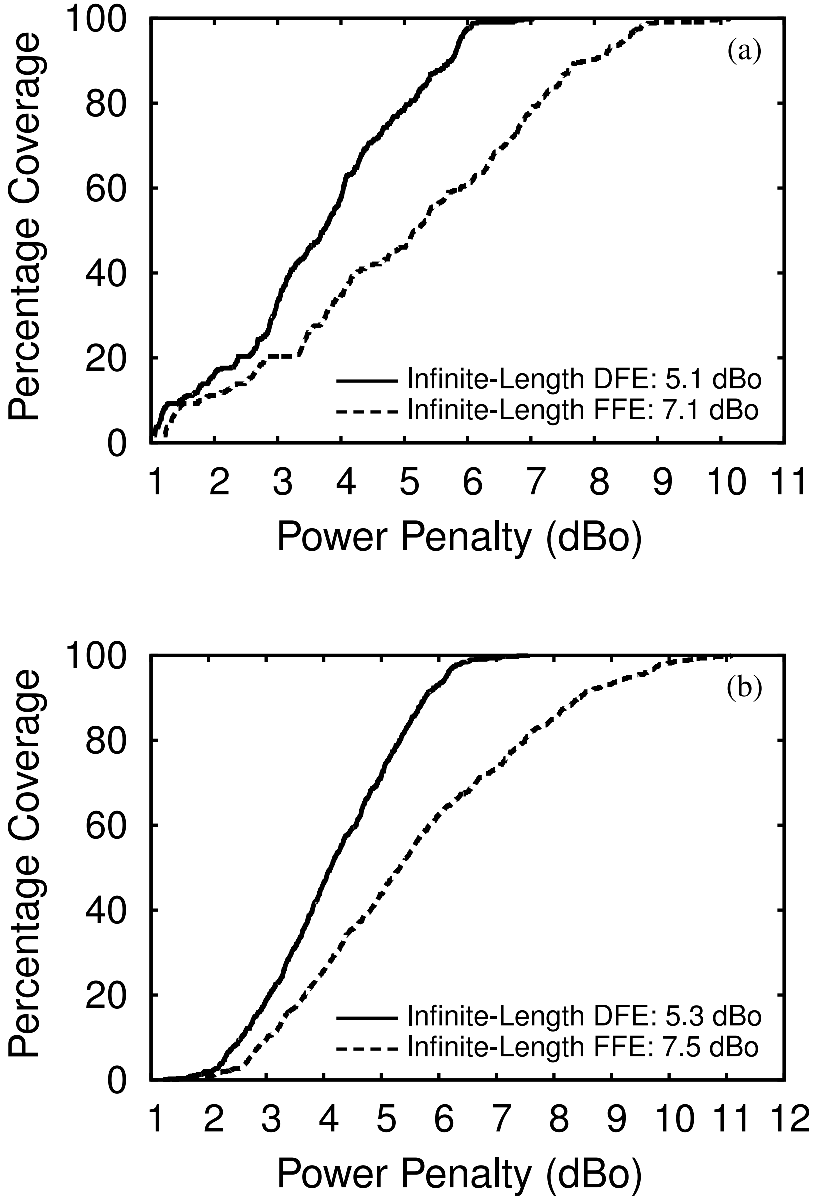

Figure 3.4: Coverage curves with the infinite-length linear and decision feedback equalizers for the 108 fiber set: (a) Center launch (b) Offset launch. Each link is 220 m long with two connectors and is operated at 10 Gbps.

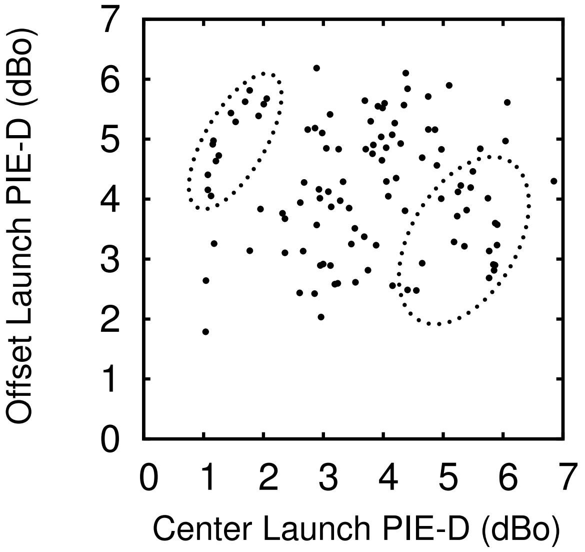

Figure 3.5: Correlation between center launch and offset launch performance for the infinite-length DFE (220 m long link at 10Gps).

3.2.1 Launch Diversity: Joint Launch

Thus far, we have presented power penalty results for center and offset launches separately. Based on our discussion of the four illustrative refractive index profiles, we observe that center defects have a more adverse effect on center launch performance than on offset launch performance. Similarly, edge and mid-axis defects impact offset launch more significantly than center launch. Although such observations may be applicable to individual defects, they may not be valid for arbitrary refractive index profiles, which often have a combination of defects. To determine any possible correlation between CL and OSL performance of fibers, we plot the average PIE-Ds for center and offset launches on a fiber-by-fiber basis, Fig. 3.5. Indeed there are fibers with poor OSL performance that have good CL performance and vice versa (enclosed by the dotted ellipses). The overall statistical performance of the DFE with the installed fiber base can be improved if this launch diversity can be exploited.

Based on such reasoning, the IEEE 802.3aq task force [16] has recommended the use of *joint launch* (JL) in 10 Gbps serial links employing electronic dispersion compensation.

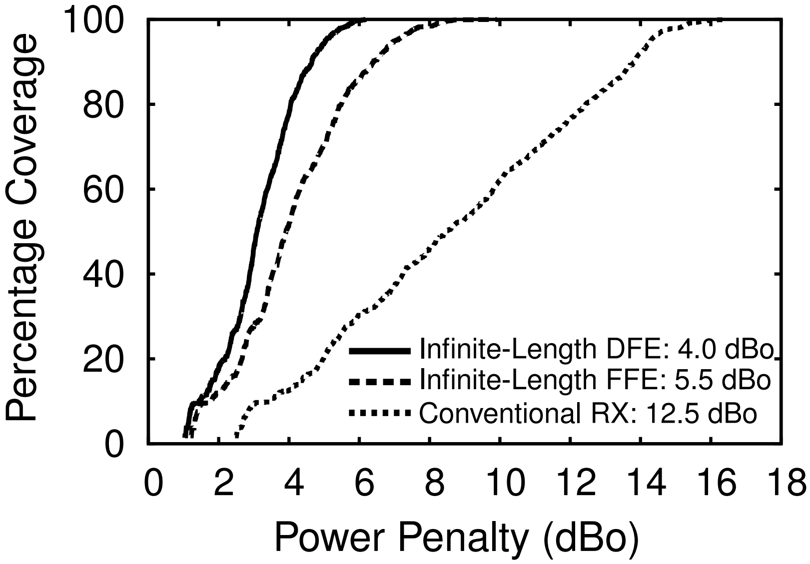

Figure 3.6: Coverage curves with joint launch for the conventional receiver and links with the infinite-length linear and decision feedback equalizers. Each link is 220 m long with two connectors and is operated at 10 Gbps.

For any given link, joint launch selectively chooses the optimum launch between center and offset launch, although the implementation details are left to the installers and the equipment manufacturers. The statistical performance of JL is determined by first generating pairs of CL and OSL PIE-Ds for each link. Specifically, a total of 28 pairs of metrics can be generated from four center launch PIE-Ds ($0 - 3\mu$m) and seven offset launch PIE-Ds ($17 - 23\mu$m). For each pair of metrics, the smaller of the two PIE-Ds is chosen. The cumulative distribution for the joint launch metrics can then be generated assuming that each of these 28 PIE-Ds is equally likely. Figure 3.6 shows the coverage curves with joint launch for both the conventional receiver and links with the infinite-length LE and DFE. At the 80% coverage point, the reduction in power penalty resulting from joint launch is at least 1 dBo, Table 3.2. In the rest of this research, we use joint launch for performance comparison purposes, unless stated otherwise.

Table 3.2: Joint launch power penalty at the 80% coverage point for links with no equalizer, with LE and with DFE. Also shown are the reductions in penalty when compared to center and offset launches.

Equalizer	Joint Launch	Center Launch	Offset Launch
Unequalized	12.5 dBo	2 dBo	1.9 dBo
Infinite-length LE	5.5 dBo	1.6 dBo	2 dBo
Infinite-length DFE	4.0 dBo	1.1 dBo	1.3 dBo

3.3 Finite-length Equalizer Performance for MMF Links

The performance of the infinite-length equalizers discussed in the previous section is usually sufficient to approximate the behavior of practical equalizers in wireline communications. This is primarily due to the ease with which equalizers with tens and hundreds of taps can be implemented for those applications. However, the significantly higher data rate of multi-mode fiber links makes the equalizer implementation particularly challenging. Therefore, even though the infinite-length DFE can achieve a BER = 10^{-12} or lower on 99% of 220m links at a penalty of 4 dBo with joint launch, finite-length DFEs are expected to have significant additional penalty.

We estimate the penalty of finite-length equalizers via a time-domain method, as opposed to the frequency-domain method adopted for the infinite-length LE/DFE. The finite-length DFE coefficients that minimize the mean-square error can be determined in a straightforward manner [59,60], as summarized in Appendix C. Note that the sampling phase, τ_0, and decision delay, Δ, (where $\hat{a}_k = a_{k-\Delta}$) that minimize the MSE are chosen in each case. We assume that the past decisions fed back in the DFE are correct (known as zero error-propagation). Under such an assumption, the end-to-end channel up to the input of the slicer can be represented by an FIR filter. Knowing the channel filter and the DFE coefficients, the end-to-end channel filter can be computed as described in Appendex C. At this point, the problem reduces to that of estimating the performance of an ISI channel, the solution of which has already been outlined in Appendix A. We note that the zero error

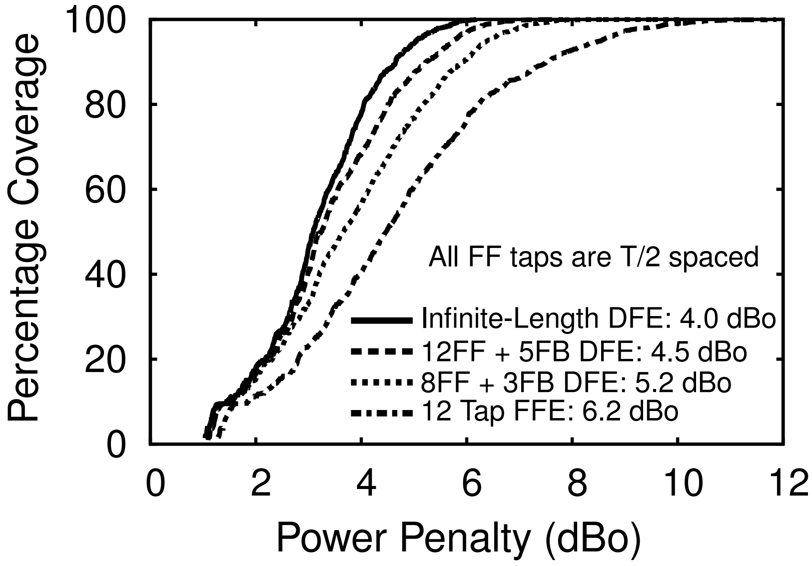

Figure 3.7: Coverage curves with joint launch for a few representative finite-length equalizers. The infinite-length DFE coverage curve is repeated for comparison purposes.

propagation assumption is generally valid at bit error rates of 10^{-12} and lower.

An over-sampling rate of $\beta = 2$ was used for the finite-length equalizers. The number of feed-forward filter taps was chosen from $\{2,4,6,8,10,12,14\}$ and the number of feedback filter taps was in the range $[0,6]$. The link parameters are consistent with those used for the infinite-length DFE/LE cases (220m/two connectors/10 Gps). The coverage curves for a few representative equalizer configurations with joint launch are shown in Fig. 3.7.

It is clear that finite-length equalizers can have significant additional penalty compared to the infinite-length equalizers. For example, the 12 ($T/2$-spaced) tap linear equalizer can be 2.2 dBo away from the infinite-length DFE while the 12 FF + 5 FB DFE performs within 0.5 dBo of the infinite-length DFE. A better understanding of the performance of various finite-length equalizers can be arrived at via contour plots such as the one in Fig. 3.8. The 80% coverage point penalty corresponding to the FF and FB taps given by the x- and y-coordinates is shown. Furthermore, the individual penalty squares are color coded, with black representing the unequalized link and white representing the infinite-length DFE performance. The trade-off between the number of feed-forward and feedback taps and the

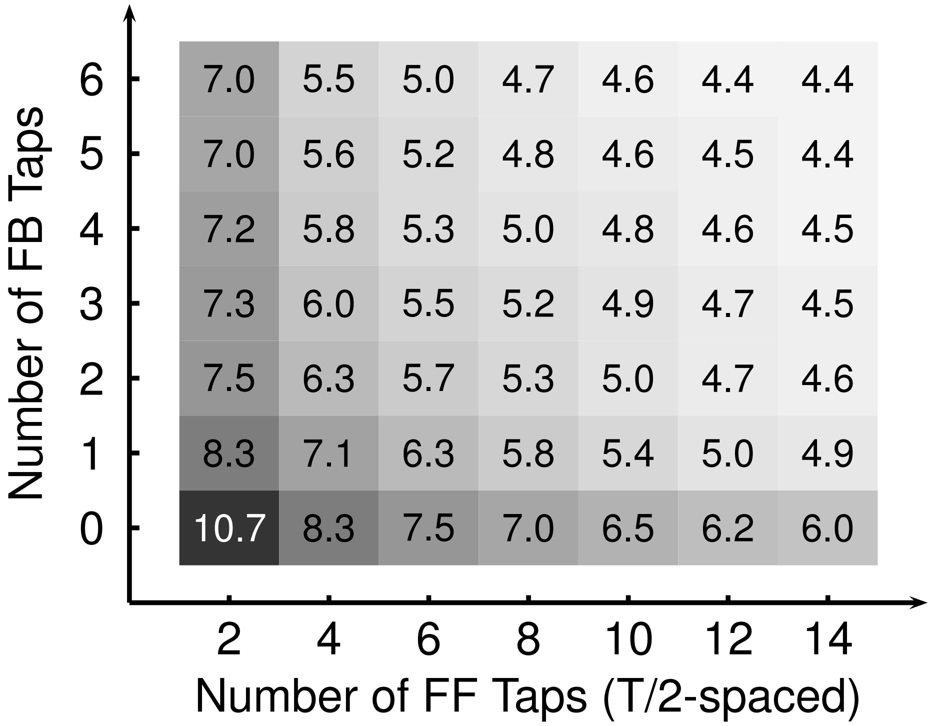

Figure 3.8: Performance of finite-length equalizers with $T/2$-spaced feed-forward taps for 220m links. The power penalty corresponds to the 80% coverage point of the 108-fiber set with two connectors for joint launch.

corresponding performance can be understood both qualitatively and quantitatively from such a plot.

Prior to our contributions to the IEEE 802.3aq task force [17–19], the performance metrics discussion primarily focused on the infinite-length DFE, with the assumption that practical equalizers will operate within 0.5 dBo of PIE-D. Although this may be true for the 12 FF + 5 FB DFE, this assumption is definitely not valid for the shorter equalizers that are being considered by various EDC vendors. Our contributions on finite-length equalizers opened the debate on the performance of practical equalizers. Eventually, a complicated procedure that took into account all the different equalizer configurations (Fig. 3.8) but at the same time was independent of any specific design was developed by the IEEE.

Based on these results, we conclude that 220m long 10 Gps links can achieve a BER = 10^{-12} or lower when the receiver employs electronic equalization. Since the penalties

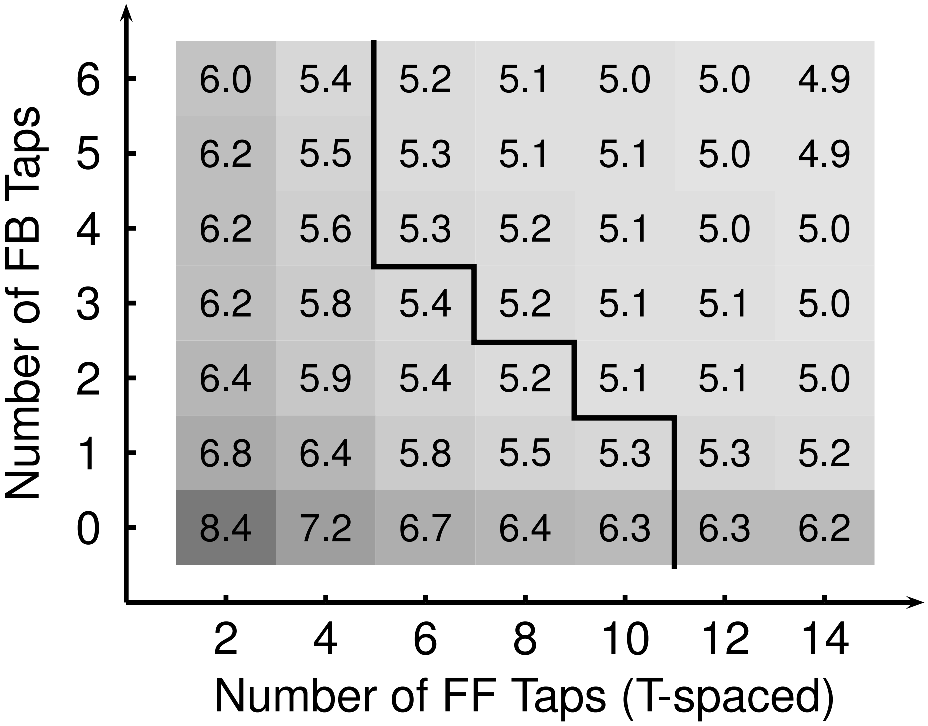

	2	4	6	8	10	12	14
6	6.0	5.4	5.2	5.1	5.0	5.0	4.9
5	6.2	5.5	5.3	5.1	5.1	5.0	4.9
4	6.2	5.6	5.3	5.2	5.1	5.0	5.0
3	6.2	5.8	5.4	5.2	5.1	5.1	5.0
2	6.4	5.9	5.4	5.2	5.1	5.1	5.0
1	6.8	6.4	5.8	5.5	5.3	5.3	5.2
0	8.4	7.2	6.7	6.4	6.3	6.3	6.2

Figure 3.9: Performance of finite-length equalizers with T-spaced feed-forward taps for 220m links.

reported here are the ideal, simulation-based numbers, another 0.5 dBo of this penalty is typically allocated to implementation issues. Therefore, a linear equalizer with 12 ($T/2$-spaced) taps is not likely to achieve the required performance. At the same time, an 8 FF + 3 FB tap DFE or a 12 FF + 5 FB tap DFE will perform adequately.

3.3.1 Baud and Fractionally Spaced DFEs

The finite-length equalizer results discussed in the previous sections were generated under the assumption that the feed-forward filter taps were $T/2$-spaced. Therefore, given a fixed number of feed-forward taps, such an equalizer spans fewer bit periods compared to the T-spaced equalizer. If the number of bits the ISI spans lies in between the spans of these two equalizers, then the baud-spaced equalizer is expected to have superior performance. This may result in sufficient reduction in equalizer complexity. To verify if this is indeed true, we determine the performance of the T-spaced equalizer for various number of feed-forward and feedback taps. The discretized contour plot of the penalty at the 80% coverage point is shown in Fig. 3.9. For all equalizer configurations below and to the left of the piece-wise linear solid line, the T-spaced equalizer has better performance. Unfortunately, approximately half of these configurations have a penalty larger than 6.0 dBo and so they cannot support 10 Gbps operation over 220m MMF links. Therefore, only a handful of T-spaced equalizer configurations are useful. As explained next, even for these cases timing issues may result in poorer realizable performance.

Note that for both the fractionally spaced and the baud-spaced equalizer the performance shown assumes that the optimum sampling instant has been chosen. While the fractionally spaced equalizer is relatively insensitive to timing issues, the performance of the T-spaced equalizer can significantly degrade with small deviations from the optimum sampling instant [52]. This is because the T-spaced equalizer attempts to equalize the folded or aliased spectrum :

$$H_T(f) = \frac{1}{T}\sum_{l} H\left(f - \frac{l}{T}\right) \exp\left[j2\pi\left(f - \frac{l}{T}\right)\tau_0\right] \tag{3.6}$$

where $H(f)$ is the channel response up to the equalizer input and τ_0 is the sampling instant. Since the signal has a bandwidth somewhere between $1/(2T)$ and $1/T$, aliasing will occur and hence the baud-spaced equalizer cannot directly equalize the phase distortion due to timing issues. Therefore, even for the equalizer configurations where the T-spaced equalizer meets the performance requirement and is better than the $T/2$-spaced equalizer, the actual realizable performance is a strong function of the timing circuitry.

On the other hand, the $T/2$-spaced equalizer is not likely to see any aliasing and so it is effectively equalizing the channel response directly. In addition to relaxed timing circuitry requirements, the fractionally spaced equalizer will have superior performance, provided it has sufficient number of taps. This is indeed the case with the equalizer configurations above and to the right of the solid line in Fig. 3.9. In fact, the fractionally spaced linear equalizer can realize the optimum linear equalizer which is nothing but the matched filter followed by a baud-spaced equalizer [51,52].

In view of the results presented, we believe that a filter tap spacing of $T/2$ is appropriate for MMF links.

3.4 Can reach be extended to 300m?

The results of the previous sections indicate that equalizers of reasonable complexity can support 10 Gbps over 220m of multi-mode fiber. Since the original goal was to achieve a reach of 300m, we also determine equalizer performance for such links. In this case, the infinite-length DFE has a penalty of 4.8 dBo at the 80% coverage point with joint launch.

The finite-length equalizer performance with $T/2$-spaced feed-forward filter taps is shown in Fig. 3.10. We find that a larger number of equalizer taps are required to have a penalty smaller than 6.0 dBo compared to the 220m case. For example, the 12 feed-forward tap, 5 feedback tap DFE has a penalty of 5.8 dBo, which just satisfies the performance requirement. Clearly, the equalizer complexity required to support 10 Gbps transmission over 300m of multi-mode fiber is significant. Indeed, the IEEE 802.3aq task force relaxed the reach requirement to 220m in view of such equalizer complexity issues.

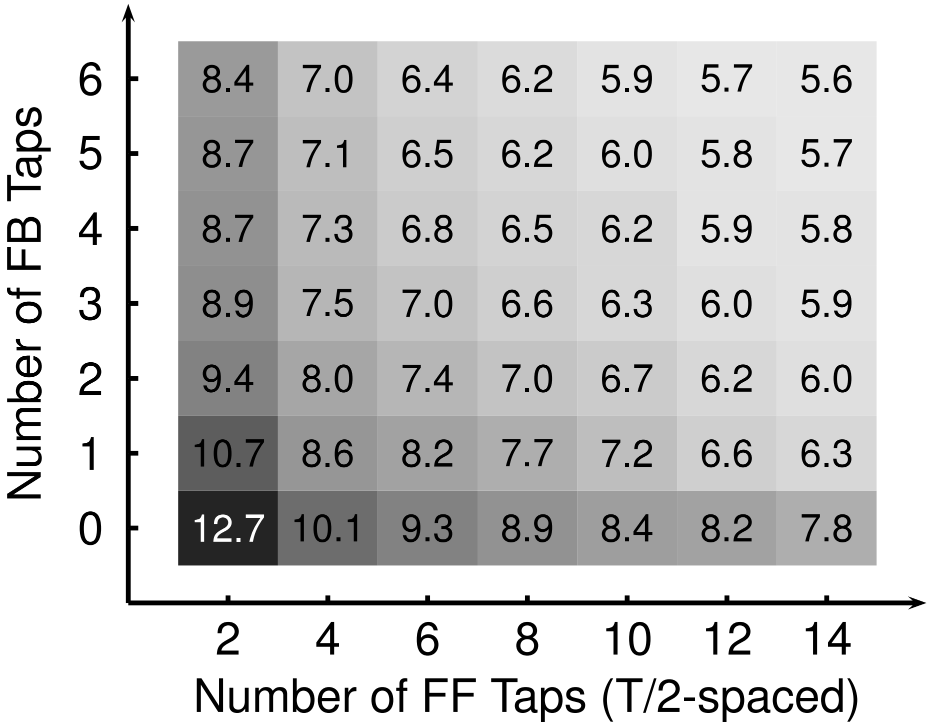

Figure 3.10: Performance of finite-length equalizers with $T/2$-spaced feed-forward taps for 300m links.

CHAPTER IV

BIDIRECTIONAL DFE FOR MMF LINKS

In the previous chapter, we saw that a DFE with as many as 12 feed-forward and 5 feedback taps is required to just support 10 Gbps transmission over 300m long multi-mode fiber links. Since implementing such long DFEs is particularly challenging at 10 Gbps, the IEEE 802.3aq task force relaxed the link length to 220m. Given this reach-complexity bottleneck, we explore a low-complexity extension of the DFE equalizer, known as the bidirectional DFE (BiDFE). We will establish its performance for MMF links both when the BiDFE is infinitely long and when it is of finite length. In the process, we will develop a new coefficient optimization algorithm.

4.1 The BiDirectional DFE

The performance of the infinite-length DFE is independent of whether the ISI is of the pre-cursor or the post-cursor type since the matched filter makes the composite channel response symmetric in both cases. On the other hand, finite-length DFEs result in higher power penalties with pre-cursor ISI than with post-cursor ISI. This is evident from the limiting case of only post-cursor ISI, where the feedback filter cancels the ISI without any noise enhancement whereas pure pre-cursor ISI will result in significant penalty with finite number of taps. We note that if the channel response is reversed in time then pre-cursor ISI effectively becomes post-cursor ISI and vice versa. This can be indirectly accomplished by a time-reversal of the received waveform. A DFE equalizing such a time-reversed signal will be known as the *reverse DFE* whereas the conventional DFE will be referred to as the *forward DFE*. The outputs of the reverse DFE (slicer input, detected bits) are in the time-reversed order. Therefore, another time-reversal operation is required to obtain the transmit bits in the original order.

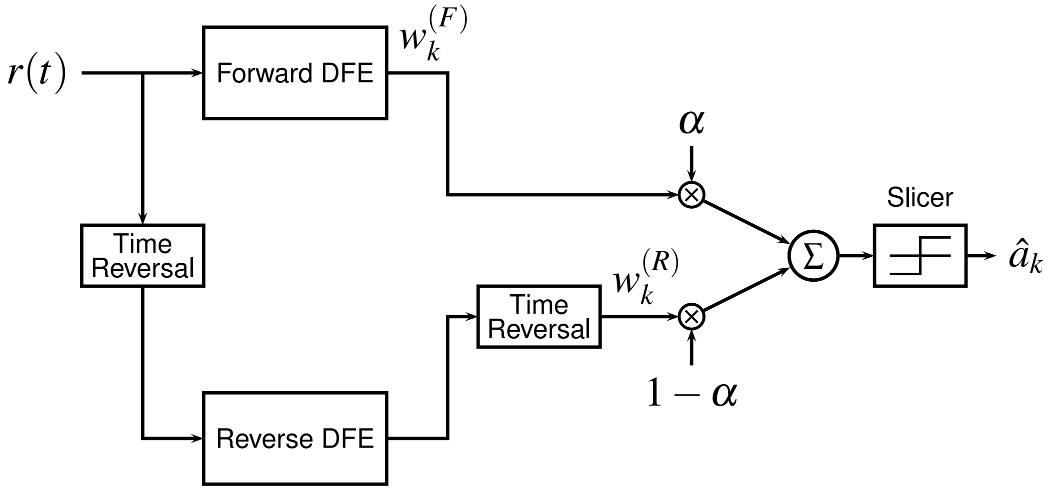

Figure 4.1: Structure of the bidirectional DFE (BiDFE).

The concept of selectively choosing between the forward DFE and the reverse DFE was independently proposed by Ariyavisitakul [61,62] and Suzuki [63] in the context of indoor wireless communications. We shall refer to such an equalizer as the *selection DFE*. The noise at the output of the forward and reverse DFEs is typically poorly correlated with each other, thereby providing an additional source of diversity.

Time-reversal diversity has been exploited in two different ways in the literature. The bi-directional arbitrated DFE (BAD) approach [21,64] generates two estimates of the received signal using the detected bits for the forward and the reverse DFEs and an estimate of the channel response. From the actual received signal and its estimates, it then computes error signals that are used to arbitrate between the outputs of the two DFEs. Although the BAD approach performs excellently, the complexity of the entire system is considerable. A much simpler technique is to linearly combine the slicer inputs of the forward and the reverse DFEs ($w_k^{(F)}, w_k^{(R)}$) and then threshold the result to determine the transmit bit, Fig. 4.1. Such a receiver structure is known as the *bidirectional DFE* (BiDFE) [20,65,66]. The linear combination occurs through the single weighting parameter α.

After the initial burst of research on bidirectional DFEs [20,21,64–66], no further results have been reported in the literature. We believe that this research is the first effort to generalize the design and analysis of the BiDFE and apply it to practical channels. The filter coefficients of the BiDFE can be obtained either by separate optimization of the constituent DFEs or via joint optimization. The joint optimization of the finite-length BiDFE for arbitrary, asymmetric channels[1] has been performed in [66] under the assumption of a matched-filter front-end. In this research, we develop joint optimization tools for the BiDFE for the most general case of an arbitrary front-end filter together with fractionally-spaced feed-forward filters. Furthermore, we develop performance estimation techniques that avoid Monte Carlo simulations for the BiDFE under both separate and joint optimization.

4.2 Infinite-Length BiDFE

The infinite-length BiDFE was analyzed in [65] under the high signal-to-noise ratio assumption. Furthermore, it is assumed that the channel does not have zeros on the unit circle. In addition, the jointly optimized infinite-length BiDFE is analyzed under the assumption that after matched-filtering, the constituent DFEs have identical filter coefficients. This restriction will be clarified later. In this section, we relax these assumptions and determine the performance of the infinite-length BiDFE.

4.2.1 Mathematical Preliminaries

Any continuous-time, linear, communication channel can be reduced to an equivalent discrete-time channel using the whitened matched filter (WMF) front-end [51,67]. Therefore, without loss of generality, the infinite-length BiDFE will be analyzed assuming the following channel model :

$$r_k = a_k \bigstar h_k + n_k \quad \Longleftrightarrow \quad r_k = \{a_k\} \bigstar H(z) + \{n_k\} \tag{4.1}$$

where a_k are the transmit bits, h_k is the channel response and n_k is the noise, which is white and Gaussian with variance σ_n^2. The transmit bits are assumed to be independent

---

[1] Channel impulse response is not symmetric with respect to pre-cursor and post-cursor ISI.

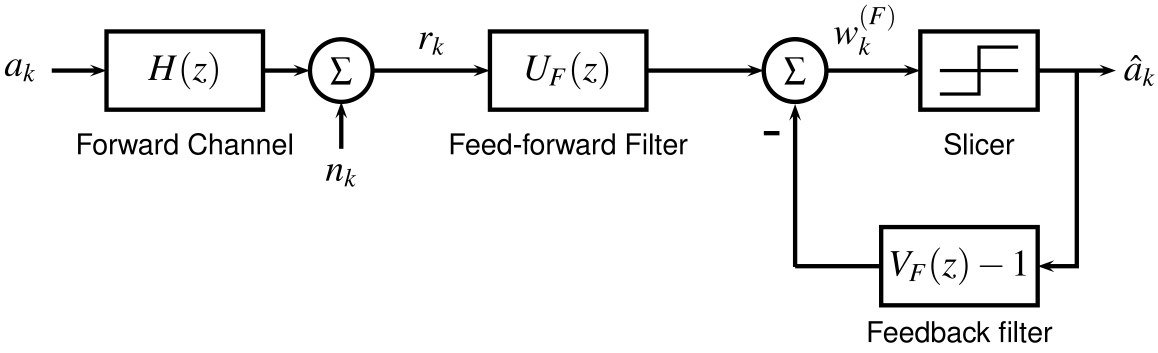

Figure 4.2: The forward channel and the corresponding DFE.

and identically distributed with variance σ_a^2. For the sake of conceptual clarity, we have abused the notation slightly in mixing time-domain and transform-domain quantities in the alternative representation to the right.

We combine the conventional time-reversal operation with the complex conjugation operation to arrive at the operator $\mathscr{R}\{\cdot\}$:

$$\tilde{r}_k \overset{\Delta}{=} \mathscr{R}\{r_k\} = r_{-k}^* \quad \Longleftrightarrow \quad \tilde{R}(z) = R^*(1/z^*) \tag{4.2}$$

where r_k are the received samples of the equivalent discrete-time equivalent channel. This minor modification to the time-reversal operation simplifies the subsequent analysis considerably compared to the efforts in [62, 65]. It is straightforward to show that :

$$\tilde{r}_k = \tilde{a}_k \bigstar \tilde{h}_k + \tilde{n}_k \quad \Longleftrightarrow \quad \tilde{r}_k = \{\tilde{a}_k\} H^*(1/z*) + \{\tilde{n}_k\} \tag{4.3}$$

4.2.2 Separately Optimized Forward DFE

The separately optimized forward DFE equalizes the channel modeled by equation (4.1). The structure of the DFE is shown in Fig. 4.2, where $U_F(z)$ is the feed-forward filter and $V_F(z)-1$ is the feedback filter with $V_F(z)$ being monic and minimum phase. We determine the DFE filters that minimize the mean square error (MSE) :

$$e_k^{(F)} = w_k^{(F)} - \hat{a}_k \approx w_k - a_k \tag{4.4}$$

$$\xi_F = E\left[|e_k^{(F)}|^2\right] = \frac{1}{2\pi}\int_{-\pi}^{\pi} S_e\left(e^{j\omega}\right) d\omega \tag{4.5}$$

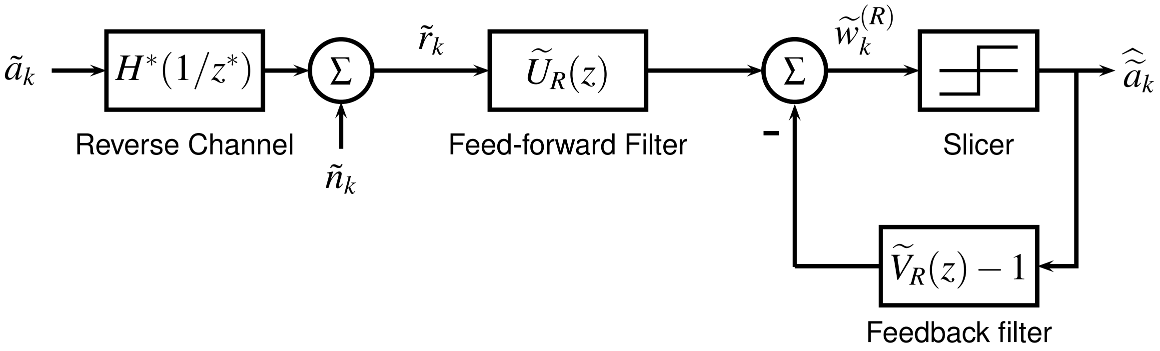

Figure 4.3: The reverse channel and the corresponding DFE.

where $S_e\left(e^{j\omega}\right)$ is the power spectrum of the error e_k. Under the assumption that no erroneous decisions are fed back, it can be shown that the MSE is minimized by the following choice of filters [51,59] :

$$U_F(z) = \frac{H^*\left(1/z^*\right)}{\sigma_p^2 P^*\left(1/z^*\right)} \tag{4.6}$$

$$V_F(z) = P(z) \tag{4.7}$$

where we have utilized the following spectral factorization :

$$|H(z)|^2 + \frac{\sigma_n^2}{\sigma_a^2} = \sigma_p^2 P(z) P^*\left(1/z^*\right) \tag{4.8}$$

$$\sigma_p^2 = \exp\left[\frac{1}{2\pi}\int_{-\pi}^{\pi} \ln\left\{\left|H(e^{j\omega})\right|^2 + \frac{\sigma_n^2}{\sigma_a^2}\right\} d\omega\right] \tag{4.9}$$

with $P(z)$ being monic and minimum-phase. The error sequence is then given by :

$$e_k^{(F)} = \{n_k\} \bigstar \left(\frac{H^*}{\sigma_p^2 P^*}\right) - \{a_k\} \bigstar \left(\frac{\sigma_n^2/\sigma_a^2}{\sigma_p^2 P^*}\right) \tag{4.10}$$

4.2.3 Separately Optimized Reverse DFE

The separately optimized reverse DFE equalizes the channel modeled by equation (4.3). In this case, we denote the feed-forward and feedback filters by $\widetilde{U}_R(z)$ and $\widetilde{V}_R(z) - 1$ where $\widetilde{V}_R(z)$ is monic and minimum-phase, Fig. 4.3.

The filters that minimize the MSE are given by :

$$\widetilde{U}_R(z) = \frac{H(z)}{\sigma_p^2 P^*(1/z^*)} \tag{4.11}$$

$$\widetilde{V}_R(z) = P(z) \tag{4.12}$$

The corresponding error and and minimum MSE are :

$$\tilde{e}_k^{(R)} = \{\tilde{n}_k\}\bigstar\left(\frac{H}{\sigma_p^2 P^*}\right) - \{\tilde{a}_k\}\bigstar\left(\frac{\sigma_n^2/\sigma_a^2}{\sigma_p^2 P^*}\right) \tag{4.13}$$

The transmit bit sequence is retrieved in the correct order after another time-reversal. Therefore, the error with respect to the original transmit bits is then given by :

$$e_k^{(R)} = w_k^{(R)} - a_k = \{n_k\}\bigstar\left(\frac{H^*}{\sigma_p^2 P}\right) - \{a_k\}\bigstar\left(\frac{\sigma_n^2/\sigma_a^2}{\sigma_p^2 P}\right) \tag{4.14}$$

4.2.4 Separately Optimized Bidirectional DFE

The input to the final slicer of the BiDFE is given by :

$$w_k = \alpha w_k^{(F)} + (1-\alpha)\, w_k^{(R)} = a_k + e_k \tag{4.15}$$

$$e_k = \alpha e_k^{(F)} + (1-\alpha)\, e_k^{(R)} \tag{4.16}$$

To understand the auto-correlation and cross-correlation properties of the forward and reverse error sequences, we define ν_k :

$$\nu_k = \{n_k\}\bigstar H^* - \frac{\sigma_n^2}{\sigma_a^2}\{a_k\} \quad \Longleftrightarrow \quad S_\nu(z) = \sigma_n^2 \sigma_p^2 P(z) P^*(1/z^*) \tag{4.17}$$

where $S_\nu(z)$ is the power spectrum of ν_k. Therefore, the two error sequences are then given by :

$$e_k^{(F)} = \{\nu_k\}\bigstar\left(\frac{1}{\sigma_p^2 P^*}\right) \quad \Longleftrightarrow \quad S_F(z) = \frac{\sigma_n^2}{\sigma_p^2} \tag{4.18}$$

$$e_k^{(R)} = \{\nu_k\}\bigstar\left(\frac{1}{\sigma_p^2 P}\right) \quad \Longleftrightarrow \quad S_R(z) = \frac{\sigma_n^2}{\sigma_p^2} \tag{4.19}$$

Therefore, the forward and the reverse DFE have the same minimum mean square error. Furthermore, the cross power spectrum between the forward and the reverse error sequences is :

$$S_{F,R}(z) = \frac{\sigma_n^2}{\sigma_p^2} \cdot \frac{P(z)}{P^*(1/z^*)} \tag{4.20}$$

Clearly, the forward channel error sequence is an all-pass filtered version of the reverse channel error sequence.

It is straightforward to show that the choice of α that minimizes the mean square error $\xi = E[|e_k|^2]$ is given by [20]:

$$\alpha_{\text{opt}} = \frac{\xi_R - \rho\sqrt{\xi_F \xi_R}}{\xi_F + \xi_R - 2\rho\sqrt{\xi_F \xi_R}} \tag{4.21}$$

where the normalized cross-correlation ρ is defined as :

$$\rho = \frac{\Re\{E[e_k^{(F)} e_k^{(R)^*}]\}}{\sqrt{\xi_F \xi_R}} \tag{4.22}$$

with $\Re\{\cdot\}$ denoting the real part of the argument. The corresponding minimum MSE is then :

$$\xi_{\min} = \frac{\left(1-\rho^2\right)\xi_F \xi_R}{\xi_F + \xi_R - 2\rho\sqrt{\xi_F \xi_R}} \tag{4.23}$$

where $\Re\{\cdot\}$ denotes the real part of the argument. When the forward and the reverse mean-square errors are equal, we have :

$$\alpha_{\text{opt}} = \frac{1}{2} \qquad \xi_{\min} = \xi_F \left(\frac{1+\rho}{2}\right) \tag{4.24}$$

Applying this result to the infinite-length BiDFE, equations (4.18)-(4.20), we find that its performance gain over the forward DFE is :

$$\frac{\xi_{BiDFE,S}}{\xi_F} = \frac{2}{1 + \Re\left\{\frac{1}{2\pi}\int_{-\pi}^{\pi} \frac{P(e^{j\omega})}{P^*(e^{j\omega})} d\omega\right\}} \tag{4.25}$$

The formulation in [65] expresses this result in terms of the zeros of the channel response $H(z)$ at high signal-to-noise ratio, under the assumption that no spectral nulls occur. In contrast, equation (4.25) is applicable at all signal-to-noise ratios and allows for spectral nulls.

Since $0 \leq \rho \leq 1$, the maximum possible gain because of the BiDFE, under separate optimization, is 3 dBe (= 1.5 dBo) .

4.2.5 Jointly Optimized Bidirectional DFE

In the previous section, the forward and the reverse DFEs of the BiDFE were optimized to achieve the minimum mean-square error at their respective slicers. Since the global mean-square error across the final slicer in Fig. 4.1 is indicative of the performance of the BiDFE, we will now optimize the constituent DFEs to minimize this MSE.

Without loss of generality, we assume a matched-filter front end as shown in Fig. 4.4. Its output is given by :

$$y_k = a_k \bigstar Q(z) + \gamma_k \tag{4.26}$$

where $Q(z) = H(z)H^*(1/z^*)$ and γ_k is Gaussian with power spectral density $N_0Q(z)/2$. The forward and reverse DFE filters are denoted by $\{U_F(z), V_F(z)\}$ and $\{U_R(z), V_R(z)\}$ respectively. As before, $V_F(z)$ and $V_R(z)$ are monic and minimum phase. The analysis in [65] assumed that both the constituent DFEs have identical filters and proves that such a BiDFE achieves the matched filter bound (MFB). While such an assumption simplifies the analysis, it also results in a unique solution to the joint optimization problem. Although [65] illustrates the non-uniqueness of the optimum BiDFE through examples, we prove this by allowing for the constituent DFEs to have different filters. It is from this perspective that we analyze the joint optimization issue. Furthermore, our results are applicable at all SNRs. Finally, we provide a completely different proof for the key result of this section compared to [65].

It is straightforward to show that the forward and reverse DFE error samples are given

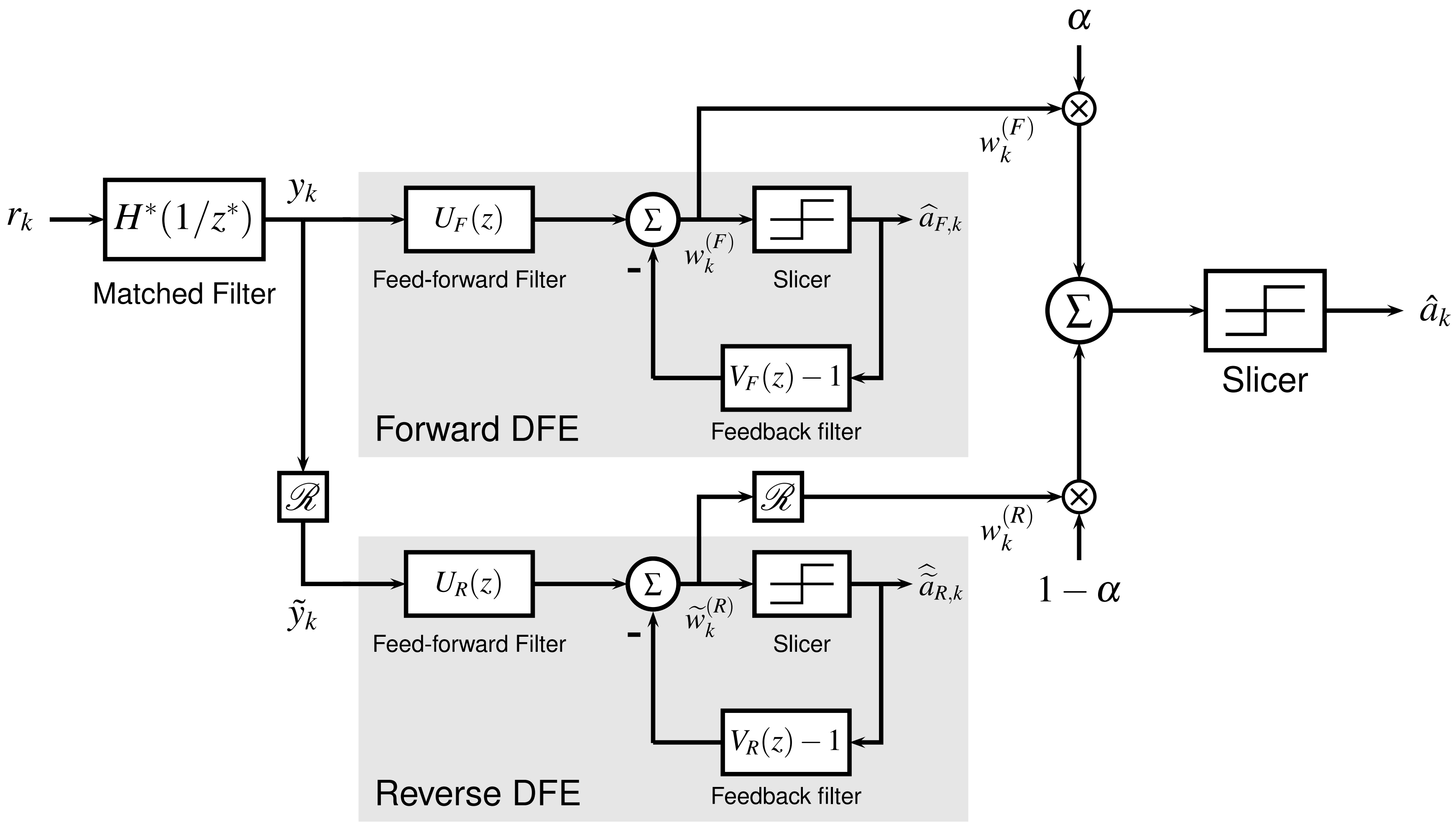

Figure 4.4: The jointly optimized, infinite-length BiDFE with a matched filter front-end.

by :

$$e_k^{(F)} = w_k^{(F)} - a_k = \gamma_k \bigstar [U_F] + a_k \bigstar [QU_F - V_F] \tag{4.27}$$

$$e_k^{(R)} = w_k^{(R)} - a_k = \gamma_k \bigstar [U_R^*] + a_k \bigstar [QU_R^* - V_R^*] \tag{4.28}$$

Note that the $w_k^{(R)}$ is obtained after a second time-reversal operation. From equation (4.16), the overall error is then given by :

$$\begin{aligned} e_k = \gamma_k \bigstar [\alpha U_F + (1-\alpha) U_R^*] + \\ + a_k \bigstar [Q\{\alpha U_F + (1-\alpha) U_R^*\} - \{\alpha V_F + (1-\alpha) V_R^*\}] \end{aligned} \tag{4.29}$$

We define the following quantities :

$$U(z) = \alpha U_F(z) + (1-\alpha) U_R^*(1/z^*) \tag{4.30}$$

$$V(z) = \alpha V_F(z) + (1-\alpha) V_R^*(1/z^*) \tag{4.31}$$

which result in :

$$e_k = \gamma_k \bigstar [U] + a_k \bigstar [QU - V] \tag{4.32}$$

The problem reduces to determining the $U(z), V(z)$ that minimize the mean square error $\xi = E\left[|e_k|^2\right]$ subject to the constraint that $V(z)$ is monic.

Theorem 4.2.1 *The unbiased, jointly optimized, infinite-length BiDFE achieves the matched filter bound (MFB). The BiDFE that satisfies this bound is not unique. The corresponding biased BiDFE is given by :*

$$\begin{aligned} \alpha U_F(z) + (1-\alpha) U_R^*(1/z^*) &= \frac{1}{q_0 + \sigma_n^2/\sigma_a^2} \\ V_F(z) &= 1 + \frac{1}{\alpha} \cdot \frac{[Q(z)]_+}{q_0 + \sigma_n^2/\sigma_a^2} \\ V_R(z) &= 1 + \frac{1}{1-\alpha} \cdot \frac{[Q(z)]_+}{q_0 + \sigma_n^2/\sigma_a^2} \end{aligned}$$

where $[Q(z)]_+ = \sum_{k>0} q_k z^{-k}$.

Proof The MSE can be expressed using the frequency domain as follows :

$$\xi = \frac{1}{2\pi}\int_{-\pi}^{\pi}\left[\sigma_a^2\left|Q(e^{j\omega})U(e^{j\omega})-V(e^{j\omega})\right|^2+\sigma_n^2\cdot Q(e^{j\omega})\left|U(e^{j\omega})\right|^2\right]d\omega \tag{4.33}$$

The fact that $V(z)$ is monic implies :

$$\frac{1}{2\pi}\int_{-\pi}^{\pi}V(e^{j\omega})d\omega = \frac{1}{2\pi}\int_{-\pi}^{\pi}V^*(e^{j\omega})d\omega = 1 \tag{4.34}$$

We introduce the Lagrange multiplier λ to account for this constraint and formulate the augmented performance metric ζ as :

$$\begin{aligned}\zeta = \frac{1}{2\pi}\int_{-\pi}^{\pi}\left[\left|Q(e^{j\omega})U(e^{j\omega})-V(e^{j\omega})\right|^2+\frac{\sigma_n^2}{\sigma_a^2}\cdot Q(e^{j\omega})\left|U(e^{j\omega})\right|^2\right]d\omega- \\ -\lambda\left[\frac{1}{2\pi}\int_{-\pi}^{\pi}V^*(e^{j\omega})d\omega-1\right]\end{aligned} \tag{4.35}$$

This optimization can be easily carried out using variational principles. Applying the well-known Euler-Lagrange equation [68], it can be shown that :

$$Q(e^{j\omega})U(e^{j\omega})-V(e^{j\omega}) = -\frac{\sigma_n^2}{\sigma_a^2}U(e^{j\omega}) = \lambda \tag{4.36}$$

Plugging these results into equation (4.34), we finally get :

$$U(z) = \frac{1}{q_0+\sigma_n^2/\sigma_a^2} \tag{4.37}$$

$$V(z) = \frac{Q(z)+\sigma_n^2/\sigma_a^2}{q_0+\sigma_n^2/\sigma_a^2} \tag{4.38}$$

where q_0 is the DC term of $Q(z)$ and is nothing but $q_0 = \sum_k |h_k|^2$. Therefore, it follows from equation (4.33) that :

$$\xi_{BiDFE,J} = \frac{\sigma_n^2}{q_0+\sigma_n^2/\sigma_a^2} \tag{4.39}$$

Since minimum MSE optimization results in a biased receiver, we would like to estimate the performance of the unbiased BiDFE. Applying the standard result that $SNR_{unbiased} = SNR_{biased}-1$ from [67], we get the MSE of the unbiased BiDFE :

$$\xi_{BiDFE,J,U} = \frac{\sigma_n^2}{q_0} = \frac{\sigma_n^2}{\sum_k |h_k|^2} \tag{4.40}$$

Therefore, the unbiased, jointly optimized, infinite-length BiDFE achieves the matched filter bound[2].

Note that any combination of $\alpha, U_F, V_F, U_R^*, V_R^*$ that results in $U(z)$ and $V(z)$ given by equations (4.37) and (4.38) also satisfies the MFB. Therefore, the optimum BiDFE is not unique.

From equations (4.31), (4.38) and the fact that $q_{-k}^* = q_k$, it follows that:

$$1 + \alpha \sum_{k>0} v_{F,k} z^{-k} + (1-\alpha) \sum_{k>0} v_{R,k}^* z^k = 1 + \frac{1}{q_0 + \sigma_n^2/\sigma_a^2} \cdot \left[\sum_{k>0} q_k z^{-k} + \sum_{k>0} q_k^* z^k \right] \tag{4.41}$$

Equating the powers of z we arrive at :

$$V_F(z) = 1 + \frac{1}{\alpha} \cdot \frac{[Q(z)]_+}{q_0 + \sigma_n^2/\sigma_a^2} \tag{4.42}$$

$$V_R(z) = 1 + \frac{1}{1-\alpha} \cdot \frac{[Q(z)]_+}{q_0 + \sigma_n^2/\sigma_a^2} \tag{4.43}$$

where $[Q(z)]_+ = \sum_{k>0} q_k z^{-k}$. Finally, from equations (4.31), (4.38) we find that :

$$\alpha U_F(z) + (1-\alpha) U_R^*(1/z^*) = \frac{1}{q_0 + \sigma_n^2/\sigma_a^2} \tag{4.44}$$

∎

It follows from Theorem 4.2.1, that the feedback filters are uniquely determined once an appropriate α has been chosen. Large feedback taps are more likely to result in error propagation in the constituent DFEs. If $\alpha \rightarrow 0$ then the feedback taps of the forward DFE will be extremely large, even approaching infinity in the limit. On the other hand, if $\alpha \rightarrow 1$ then the feedback taps of the reverse DFE will be correspondingly large. Clearly, the optimum balance between error propagation for the forward and reverse DFEs is achieved for $\alpha = 1/2$. Therefore, the optimum feedback filters are given by :

$$V_F(z) = V_R(z) = 1 + \frac{2[Q(z)]_+}{q_0 + \sigma_n^2/\sigma_a^2} \tag{4.45}$$

---

[2] The matched filter bound is the performance obtained if only one bit were transmitted, also known as *one-shot* communication. Since no ISI is present, this is the best performance that any receiver can achieve.

Various auxiliary criteria can be adopted to resolve the non-uniqueness of the feed-forward filters. For example, minimizing the mean square error of the constituent DFEs results in :

$$U_R(z) = U_R(z) = \frac{1+\frac{2[Q(z)]_+}{q_0+\sigma_n^2/\sigma_a^2}}{Q(z)+\sigma_n^2/\sigma_a^2} \tag{4.46}$$

Therefore, the feed-forward and feedback filters of the constituent DFEs are identical. The matched filter bound result in [65] was established using this assumption from the beginning.

In this section, we have proved, using an alternate method, that the infinite-length BiDFE achieves the matched filter bound at all SNRs. This was accomplished without any restrictions on the constituent DFEs. Furthermore, we have identified the sources of the non-uniqueness of the optimal BiDFE. In addition, we have established that if the constituent DFEs are expected to have minimum MSE and error propagation, then there exists a unique jointly optimized BiDFE that satisfies the MFB.

4.3 Finite-Length BiDFE

In the previous section, we analyzed the performance of the infinite-length BiDFE. We now consider the finite-length BiDFE, which is more useful for practical implementations.

4.3.1 Performance of the finite-length BiDFE

In this section, we determine the performance of the finite-length BiDFE for a given fixed set of equalizer filters. In later sections, we optimize these filters using various criteria and then evaluate the performance using the tools developed here.

We analyze the performance of the finite-length BiDFE shown in Fig. 4.5. The received signal, $r(t)$, is the output of the front-end filter, $h_{RX}(t)$, Fig. 2.8. Sampling at a rate β/T generates the samples r_l that form the input to the BiDFE.

We assume that the forward and reverse DFEs have the same number of coefficients. The important parameters of these DFEs are :

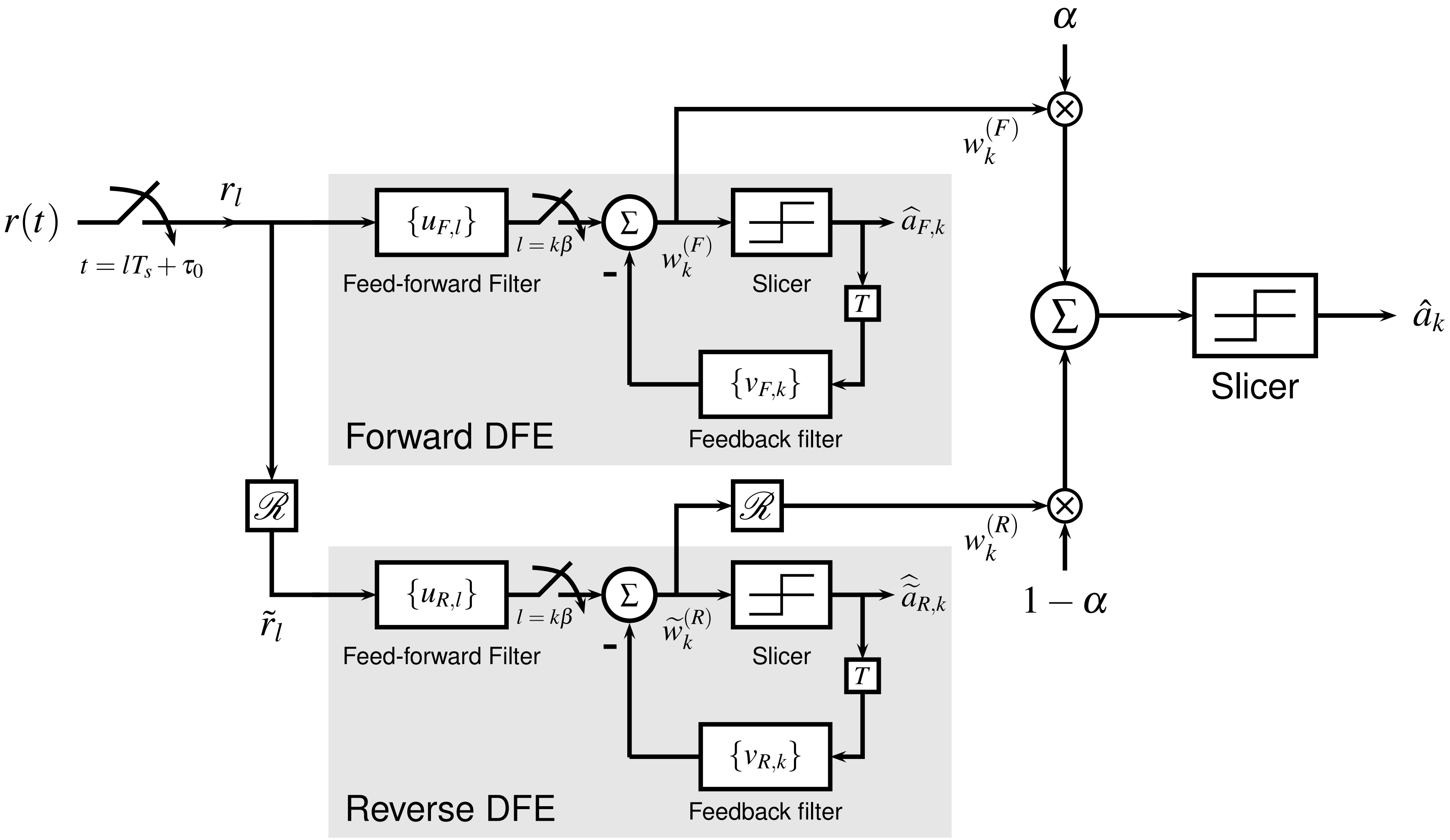

Figure 4.5: The finite-length BiDFE.

1. Forward DFE:
    - Feed-forward taps: $\{u_{F,l}\}, l = 1, 2, \ldots, \beta L_F$
    - Feedback taps: $\{v_{F,k}\}, k = 1, 2, \ldots, L_B$
    - Detection delay: Δ_F
2. Reverse DFE:
    - Feed-forward taps: $\{u_{R,l}\}, l = 1, 2, \ldots, \beta L_F$
    - Feedback taps: $\{v_{R,k}\}, k = 1, 2, \ldots, L_B$
    - Detection delay: Δ_R

Following the approach of Appendix C, the slicer input for the forward DFE is given by :

$$w_k^{(F)} = \mathbf{c}_F^T \begin{bmatrix} \mathbf{R}_{k+\Delta_F,F} \\ -\mathbf{a}_{k-1,F} \end{bmatrix} \tag{4.47}$$

where $\mathbf{c}_F^T = [\mathbf{u}_F^T \ \mathbf{v}_F^T]$ and

$$\mathbf{R}_{k+\Delta_F,F} = H_F \mathbf{A}_{k+\Delta_F,F} + \mathbf{N}_{k+\Delta_F,F} \tag{4.48}$$

$$\mathbf{a}_{k-1,F} = \begin{bmatrix} a_{k-1} & a_{k-2} & \cdots & a_{k-L_B} \end{bmatrix}^T \tag{4.49}$$

Note that $H_F, \mathbf{A}_{k,F}$ and $\mathbf{N}_{k,F}$ are defined in equation (C.9) in Appendix C.

The reverse DFE operates on the time-reversed channel, whose taps are given by :

$$h_{R,l} = h_{(L_h\beta-1)-l} \tag{4.50}$$

where L_h is the number of bit periods spanned by the end-to-end channel response $h(t)$. Applying the results of Appendix C to this channel, the slicer input for the reverse DFE is given by :

$$w_k^{(R)} = \mathbf{c}_R^T \begin{bmatrix} \mathbf{R}_{N-1-k+\Delta_R,R} \\ -\mathbf{a}_{N-1-k-1,R} \end{bmatrix} \tag{4.51}$$

where $\mathbf{c}_R^T = [\mathbf{u}_R^T \ \mathbf{v}_R^T]$, N is the number of bits per transmission block and $\mathbf{R}_{N-1-k+\Delta_R,R}$, $\mathbf{a}_{N-1-k-1,R}$ are defined as follows :

$$\mathbf{R}_{N-1-k+\Delta_R,R} = H_R \mathbf{A}_{N-1-k+\Delta_R,R} + \mathbf{N}_{N-1-k+\Delta_R,R} \tag{4.52}$$

$$\mathbf{a}_{N-1-k-1,R} = \begin{bmatrix} a_{k+1} & a_{k+2} & \cdots & a_{k+L_B} \end{bmatrix}^T \tag{4.53}$$

where $H_R, \mathbf{A}_{k,R}$ and $\mathbf{N}_{k,R}$ are appropriate modifications of equation (C.9) to reflect the reverse channel.

From equations (4.47) and (4.51), it follows that the error across the final slicer is given by :

$$e_k = w_k - a_k = \alpha \mathbf{c}_F^T \begin{bmatrix} \mathbf{R}_{k+\Delta_F,F} \\ -\mathbf{a}_{k-1,F} \end{bmatrix} + (1-\alpha)\mathbf{c}_R^T \begin{bmatrix} \mathbf{R}_{N-1-k+\Delta_R,R} \\ -\mathbf{a}_{N-1-k-1,R} \end{bmatrix} - a_k \tag{4.54}$$

$$= \begin{bmatrix} \alpha \mathbf{c}_F^T & (1-\alpha)\mathbf{c}_R^T \end{bmatrix} \begin{bmatrix} \mathbf{R}_{k+\Delta_F,F} \\ -\mathbf{a}_{k-1,F} \\ \mathbf{R}_{N-1-k+\Delta_R,R} \\ -\mathbf{a}_{N-1-k-1,R} \end{bmatrix} - a_k \tag{4.55}$$

Therefore, the overall mean square error for the BiDFE is given by :

$$\begin{aligned} \xi = E[e_k^2] =& \sigma_a^2 \begin{bmatrix} \alpha \mathbf{c}_F^T & (1-\alpha)\mathbf{c}_R^T \end{bmatrix} \begin{bmatrix} A_F & M \\ M^T & A_R \end{bmatrix} \begin{bmatrix} \alpha \mathbf{c}_F \\ (1-\alpha)\mathbf{c}_R \end{bmatrix} - \\ & -2\sigma_a^2 \begin{bmatrix} \alpha \mathbf{c}_F^T & (1-\alpha)\mathbf{c}_R^T \end{bmatrix} \begin{bmatrix} \mathbf{b}_F \\ \mathbf{b}_R \end{bmatrix} + \sigma_a^2 \end{aligned} \tag{4.56}$$

where A_F and $\mathbf{b}_F$ are defined in equation (C.14) of Appendix C. The same definitions when applied to the reverse channel yield A_R and $\mathbf{b}_R$. The only new parameter is M which determines the interaction between the coefficients of the forward and reverse DFEs. Matrix M is defined as follows :

$$M = \begin{bmatrix} H_F G_{11} H_R^T + \frac{N_0}{2\sigma_a^2} \hat{R}_N & -H_F G_{12} \\ -G_{21} H_R^T & 0_{L_B \times L_B} \end{bmatrix} \tag{4.57}$$

where the matrices G_{11}, G_{12}, G_{21} are succinctly defined through the following Matlab pseudo-code :

Definition 4.1 Various matrix definitions for the BiDFE

Matrix G_{11}:

```
Initialize: $G_{11} = 0_{L \times L}$ where $L = L_h + L_F$. Define $J = \Delta_F + \Delta_R + 1$
if $J \leq L$ then
    $G_{11}(1 : J, 1 : J) = \text{flipud}(\text{eye}(L, L))$
else
    $G_{11}(J - L + 1 : L, J - L + 1 : L) = \text{flipud}(\text{eye}(K, K))$ where $K = 2L - J$
end if
```

Matrix G_{12}:

```
Initialize: $G_{12} = 0_{L \times L_B}$
if $1 \leq \Delta_F \leq L_B$ then
    $G_{12}(1 : \Delta_F, 1 : \Delta_F) = \text{flipud}(\text{eye}(\Delta_F, \Delta_F))$
else if $\Delta_F \geq L_B + 1$ then
    $G_{12}(\Delta_F - L_B + 1 : \Delta_F, 1 : L_B) = \text{flipud}(\text{eye}(L_B, L_B))$
end if
```

Matrix G_{21}:

```
Initialize: $G_{21} = 0_{L_B \times L}$
if $1 \leq \Delta_R \leq L_B$ then
    $G_{21}(1 : \Delta_R, 1 : \Delta_R) = \text{flipud}(\text{eye}(\Delta_R, \Delta_R))$
else if $\Delta_R \geq L_B + 1$ then
    $G_{21}(1 : L_B, \Delta_R - L_B + 1 : \Delta_R) = \text{flipud}(\text{eye}(L_B, L_B))$
end if
```

Note that $\hat{R}_N = E[\mathbf{N}_{k+\Delta_F,F}\mathbf{N}^T_{N-1-k+\Delta_R,R}]$ can be easily determined from the noise autocorrelation given by equations (C.3) and (C.4) in Appendix C. We can now evaluate the overall MSE for the BiDFE from equation (4.56).

Since the input to the BiDFE slicer contains residual ISI, the mean square error may not be a good indicator of the BiDFE bit error rate performance. We can get a better estimate of the BER by explicitly considering the residual ISI. The procedure to determine the residual ISI for the forward DFE is described in Appendix C. The residual ISI for the reverse DFE can also be computed similarly. Once the residual ISI for each DFE is known along with α, the net residual ISI can be determined by aligning the ISI terms for the forward and reverse DFEs appropriately. At this point, we can quickly estimate the bit error rate and hence penalty of the BiDFE using the procedure outlined in Appendix A.

4.3.2 Separate Optimization of the BiDFE

We begin with the separate optimization technique. To summarize, the constituent DFEs are chosen to minimize their respective mean square error. Therefore, the coefficients of the constituent DFEs are given by :

$$\mathbf{c}_F = A_F^{-1}\mathbf{b}_F \tag{4.58}$$

$$\mathbf{c}_R = A_R^{-1}\mathbf{b}_R \tag{4.59}$$

The optimum weighting parameter and corresponding mean square error across the final slicer are again given by equations (4.21) and (4.23). Upon simplification using the definitions of the previous section, we get :

$$\alpha = \frac{\mathbf{c}_F^T\mathbf{b}_F - \mathbf{c}_F^T M\mathbf{c}_R}{\mathbf{c}_F^T\mathbf{b}_F + \mathbf{c}_R^T\mathbf{b}_R - 2\mathbf{c}_F^T M\mathbf{c}_R} \tag{4.60}$$

Once the DFE coefficients and α are known, the tools of the previous section can be used to determine the bit error rate and hence the optical power penalty of the BiDFE. As before, we can then evaluate the coverage curves for the 108-fiber set. As an example, Fig. 4.6 shows the coverage curves for the bidirectional DFE under separatate optimization

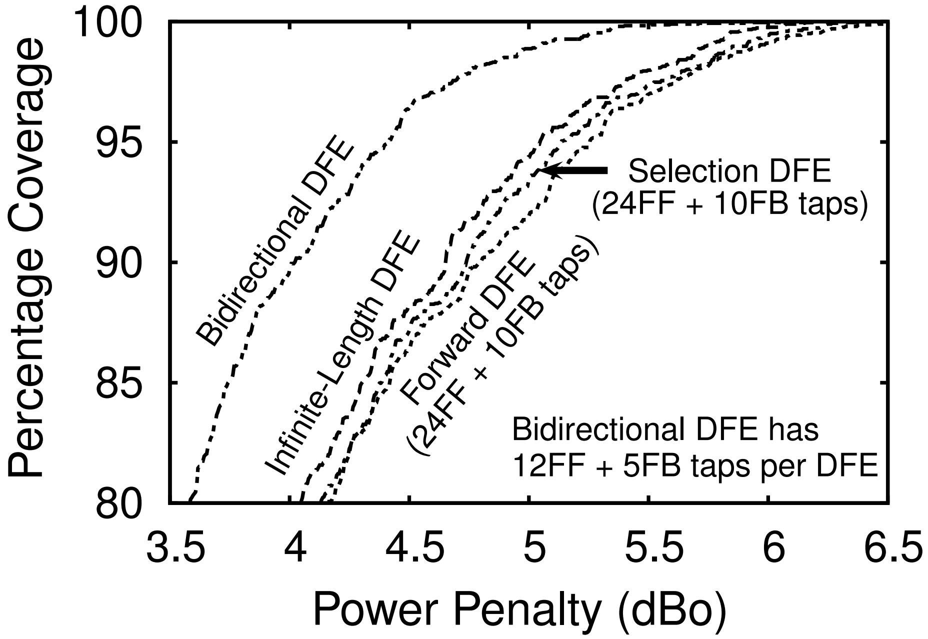

Figure 4.6: Coverage curve for the BiDFE under separate optimization with 12 ($T/2$-spaced) FF taps and 5 FB taps per constituent DFE. Only the 80%-100% coverage range is shown for the sake of clarity. Both the forward DFE and the selection DFE have 24 FF and 10 FB taps in order to have the same complexity as the BiDFE. The coverage curve for the optimum DFE is included for comparison purposes.

with 12 ($T/2$-spaced) feed-forward and 5 feedback taps for each of the constituent DFEs. The forward DFE and the selection DFE have 24 FF and 10 FB taps in order to have the same complexity as the BiDFE. All the coverage curves correspond to 220m links operating at 10Gbps with 2 connectors and joint launch. Clearly, the selection DFE does marginally better than the forward DFE and both are within 0.15 dBo of the optimum DFE performance (at the 80% coverage point). On the other hand, the BiDFE performs 0.4 dBo better than even the optimum DFE.

4.3.3 Joint Optimization of the BiDFE

In the previous section, the forward and the reverse DFEs of the BiDFE were optimized to achieve the minimum mean-square error at their respective slicers. Since the global mean-square error across the final slicer (Fig. 4.5) is indicative of the performance of the BiDFE, we will now optimize the constituent DFEs to minimize this MSE. Clearly, minimizing the

MSE given by equation (4.56) results in the following system of equations :

$$\underbrace{\begin{bmatrix} A_F & M \\ M^T & A_R \end{bmatrix}}_{A} \begin{bmatrix} \alpha \mathbf{c}_F \\ (1-\alpha)\mathbf{c}_R \end{bmatrix} = \begin{bmatrix} \mathbf{b}_F \\ \mathbf{b}_R \end{bmatrix} \tag{4.61}$$

where $\mathbf{c}_F$ and $\mathbf{c}_R$ are the filter coefficients of the forward and reverse DFEs respectively. As with the jointly optimized infinite-length BiDFE, we find that the finite-length BiDFE also is not unique. In the infinite-length case, we chose $\alpha = 0.5$ based on considerations of error propagation. We use the same choice even for the finite-length BiDFE.

For certain combinations of L_F, L_B, Δ_F and Δ_R, we find matrix A to be rank deficient. This is to be expected since we have proved that the jointly optimized BiDFE does not have a unique solution in the infinite-length case.

4.3.3.1 Constrained feedback filter method

As discussed earlier for the infinite-length BiDFE, one way of eliminating this non-uniqueness is to choose the equalizer coefficients such that the “post-cursor” ISI generated by each DFE is canceled by its own feedback filter. Under this assumption, the feed-forward and feedback filters are related as follows :

$$\mathbf{v}_F = -A_{21,F}\mathbf{u}_F \tag{4.62}$$

$$\mathbf{v}_R = -A_{21,R}\mathbf{u}_R \tag{4.63}$$

where A_F has the following block matrix paritioning :

$$A_F = \begin{bmatrix} A_{11,F} & A_{21,F}^T \\ A_{21,F} & I_{L_B} \end{bmatrix} \tag{4.64}$$

The individual block matrices are as defined by equation (C.14). A_R is partitioned similarly. Then the overall mean square error can be expressed in terms of the feed-forward filters as :

$$\begin{aligned}\xi = E[e_k^2] = & \sigma_a^2 \begin{bmatrix} \alpha \mathbf{u}_F^T & (1-\alpha)\mathbf{u}_R^T \end{bmatrix} \underbrace{\begin{bmatrix} P_{11} & P_{12} \\ P_{12}^T & P_{22} \end{bmatrix}}_{P} \begin{bmatrix} \alpha \mathbf{u}_F \\ (1-\alpha)\mathbf{u}_R \end{bmatrix} - \\ & -2\sigma_a^2 \begin{bmatrix} \alpha \mathbf{u}_F^T & (1-\alpha)\mathbf{u}_R^T \end{bmatrix} \underbrace{\begin{bmatrix} \mathbf{b}_{1,F} \\ \mathbf{b}_{1,R} \end{bmatrix}}_{\mathbf{q}} + \sigma_a^2\end{aligned} \tag{4.65}$$

where the various partitions of P are defined as follows :

$$P_{11} = A_{11,F} - A_{21,F}^T A_{21,F} \tag{4.66}$$

$$P_{22} = A_{11,R} - A_{21,R}^T A_{21,R} \tag{4.67}$$

$$P_{12} = M_{11} - M_{12} A_{21,R} - A_{21,F}^T M_{21} \tag{4.68}$$

Again M_{ij} are the appropriate partitions of M, equation (4.57). The vectors $\mathbf{b}_{1,F}$ and $\mathbf{b}_{1,R}$ are the first βL_F elements of $\mathbf{b}_F$ and $\mathbf{b}_R$ respectively.

As an example, we analyze the performance of the fiber with a center dip in its profile used with a 0μm offset launch. The link is 220m long with 2 connectors near the transmitter end. Each DFE is assumed to have 12 ($T/2$-spaced) feed-forward and five feedback taps. The separately optimized forward and reverse DFEs have optical power penalties of 8 dBo and 7.8 dBo respectively and corresponding BiDFE has a penalty of 6.4 dBo. Joint optimization of the BiDFE using the method described in this section results in a penalty of 4.2 dBo, an improvement of $\approx$ 3.6 dBo. But the power penalties of the constituent DFEs of such a BiDFE are 20.1 dBo and 18.6 dBo, a peformance degradation of $\approx$ 11 dBo. Therefore, the dramatic performance improvement of the jointly optimized BiDFE comes at the cost of the inferior performance of the constituent DFEs. Clearly, such poorly designed forward and reverse DFEs will have a significant impact on the overall performance, when practical issues such as error propagation are considered. Therefore, the constrained feedback filter method is not expected to be yield the theoretically predicted performance improvements in practice.

4.3.3.2 Constrained FDFE/RDFE interaction method

From equation (4.61), it is clear that the interaction between the forward and the reverse DFE occurs through the matrix M. The jointly optimized BiDFE results in minimum overall MSE, but it is not uniquely defined and the constituent DFEs are not likely to have the possible minimum MSE. When M is the all zero matrix, the forward and reverse DFE coefficients are identical to the case when they minimize their respective mean square errors. In this case, the BiDFE performance is the same as that of the separately optimized BiDFE. Furthermore, the constituent DFEs are uniquely defined and they also achieve their respective minimum MSEs. If somehow we can control the degree to which the forward and reverse DFEs impact each other, then we are likely to have better control over the tradeoff between individual MSEs and the overall MSE. Based on this heuristic reasoning, we propose a weighting factor λ :

$$\begin{bmatrix} A_F & \lambda M \\ \lambda M^T & A_R \end{bmatrix} \begin{bmatrix} \alpha \mathbf{c}_F \\ (1-\alpha)\mathbf{c}_R \end{bmatrix} = \begin{bmatrix} \mathbf{b}_F \\ \mathbf{b}_R \end{bmatrix} \tag{4.69}$$

Note that $\lambda = 0$ corresponds to independent optimization of the forward and reverse DFEs whereas $\lambda = 1$ is equivalent to the unconstrained joint optimization of the BiDFE. Furthermore, λ also controls the transition from a unique solution for the constituent DFEs to a non-unique solution.

We illustrate the performance of the BiDFE with this new optimization method for the center-dip fiber. We sweep λ from zero to one and determine the penalty improvement for the jointly optimized BiDFE compared to the separately optimized one, Fig. 4.7. We also show the penalty increase for the forward and reverse DFEs compared to their penalties under separate optimization. The corresponding quantities for the constrained feedback filter method, labeled "Method 1", have been added for comparison purposes. The constrained

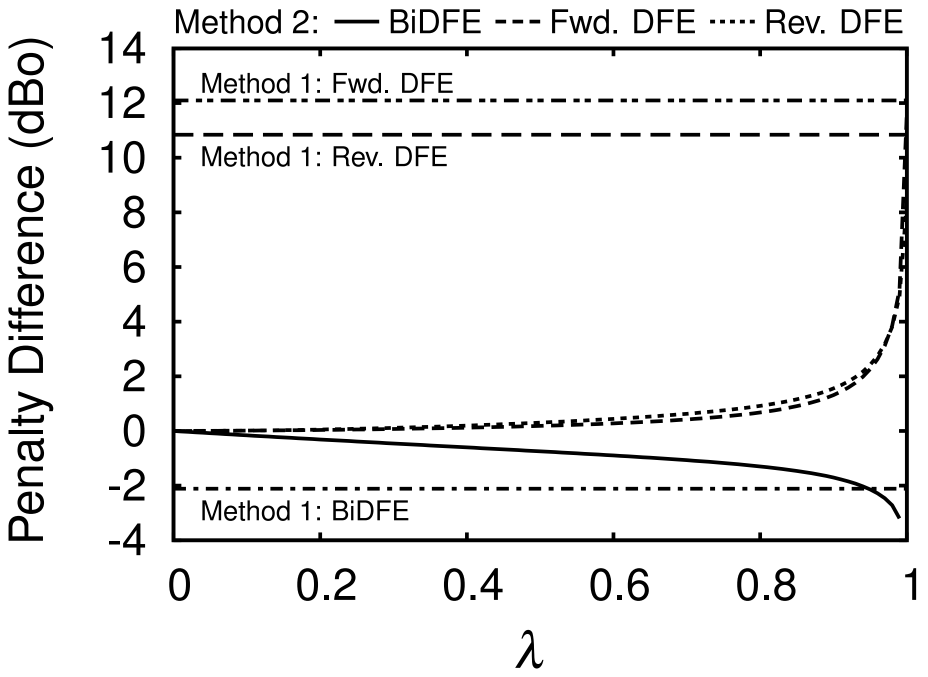

Figure 4.7: Penalty improvement for the jointly optimized BiDFE compared to the separately optimized BiDFE for the two design methods. Method 1 is the constrained feedback filter method whereas Method 2 is the constrained FDFE/RDFE interaction method. The penalty degradation for the forward and reverse DFEs for each method are also shown. The penalties are for the fiber with a center dip. The link is 220m long, has two connectors and is used wit a 0μm offset launch. Each constituent DFE has 12 ($T/2$-spaced) FF and 5 FB taps.

FDFE/RDFE interaction method is called "Method 2" in Fig. 4.7. Clearly, method 1 results in better BiDFE performance compared to method 2 for most values of λ. However, the forward and reverse DFEs under method 1 have penalties that are approximately 10 dBo worse than the corresponding penalties with method 2.

Several interesting observations can be made from Fig. 4.7. As λ approaches unity, the BiDFE penalty decreases with method 2. This is expected since the more aware each DFE is of the other DFE's impact, the lower the overall penalty. Interestingly, as λ increases, the forward and reverse DFE penalties also increase under method 2. Basically, the more the interaction between the constituent DFE taps, the more they deviate from their respective optimum settings. Therefore, if one requires any improvement over the separately optimized BiDFE, then a loss in performance for the FDFE/RDFE has to be tolerated. Unlike

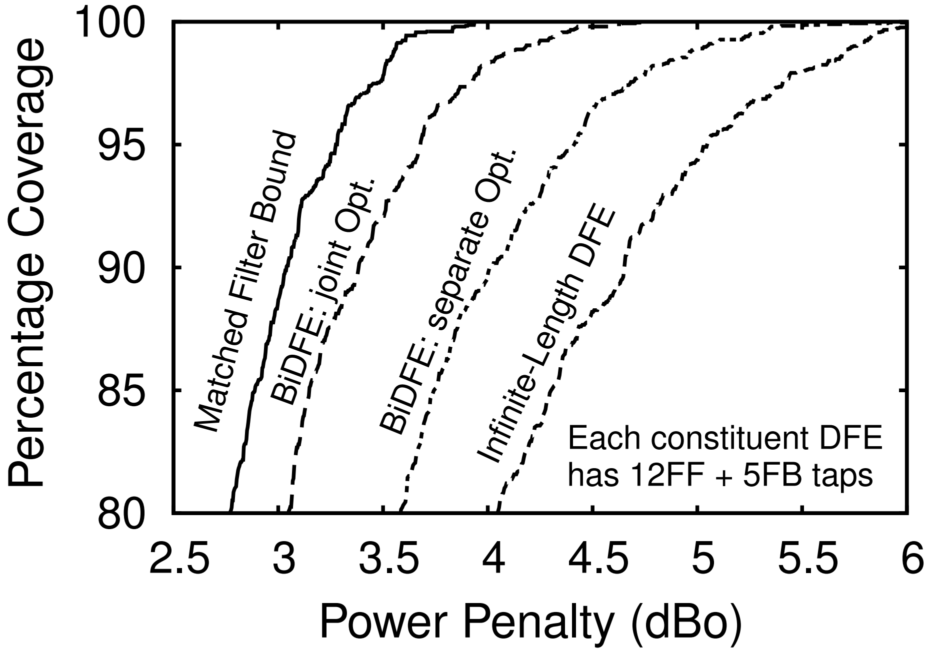

Figure 4.8: Coverage curve for the BiDFE under joint optimization with 12 ($T/2$-spaced) FF taps and 5 FB taps per constituent DFE. Only the 80%-100% coverage range is shown for the sake of clarity.

method 1, the λ parameter allows the designer to make this trade-off in a graceful manner. We will employ the constrained FDFE/RDFE interaction technique (method 2) for optimizing the BiDFE in the rest of this research. Based on simulations using the 108-fiber set, we find that a choice of $\lambda = 0.9$ achieved the right balance between the BiDFE penalty and the constituent DFE penalties.

Figure 4.8 shows the coverage curves for the bidirectional DFE under joint optimization with 12 ($T/2$-spaced) feed-forward and 5 feedback taps for each of the constituent DFEs. Also included are the coverage curves corresponding to the matched filter bound, the infinite-length DFE and the separately optimized BiDFE. Clearly, the jointly optimized BiDFE performs better than the optimum DFE by as much as 1 dBo and is within 0.2 dBo of the matched filter bound at the 80% coverage point, Table 4.1. Furthermore, simply changing the optimization procedure (from separate to joint) without changing the receiver structure has resulted in a performance gain of 0.6 dBo.

Table 4.1: Joint launch power penalty at the 80% coverage point for the BiDFE under separate and joint optimizations. Also shown are the improvements over the optimum DFE and the gap from the matched filter bound. The penalties for the conventional (forward) DFE are provided for comparison purposes.

Equalizer	Joint Launch	Improvement over the Optimum DFE	Gap from the Matched filter bound
Optimum DFE	4.0 dBo	-	1.2 dBo
12FF + 5FB DFE	4.5 dBo	-0.5 dBo	1.7 dBo
24FF + 10FB DFE	4.2 dBo	-0.2 dBo	1.4 dBo
BiDFE: Separate Opt. (12FF + 5FB per DFE)	3.6 dBo	0.4 dBo	0.8 dBo
BiDFE: Joint Opt. (12FF + 5FB per DFE)	3.0 dBo	1 dBo	0.2 dBo

4.4 Complexity Reduction

The analysis and results of the previous sections have established the superior performance of the BiDFE for MMF links. In this section, we demonstrate that given a finite number of filter taps, the BiDFE utilizes them better than the conventional (forward) DFE.

Figure 4.9 shows the coverage curves for the jointly optimized BiDFE with 8 ($T/2$-spaced) feed-forward taps per constituent DFE. The number of feedback taps per DFE is gradually reduced from 3 to 1. Clearly, the performance of the 2 feedback tap DFE is very close to that of the 3 FB tap case and both are better than the optimum DFE. Even the BiDFE with 8 FF and 1 FB taps per DFE performs as well as the optimum DFE (at the 80% coverage point). Of course, each of these BiDFE configurations performs better than any finite-length forward DFE.

We now reduce the number of feed-forward taps per DFE keeping the number of feedback taps fixed at 2 coefficients per DFE, Fig. 4.10. The 6 FF + 2 FB tap BiDFE performs slightly better than the optimum DFE. For comparison purposes, the 12 FF + 5 FB tap forward DFE performs 0.5 dBo worse than the optimum DFE. Therefore, given approximately the same number of filter taps (12 FF and 4-5 FB coefficients), the BiDFE utilizes

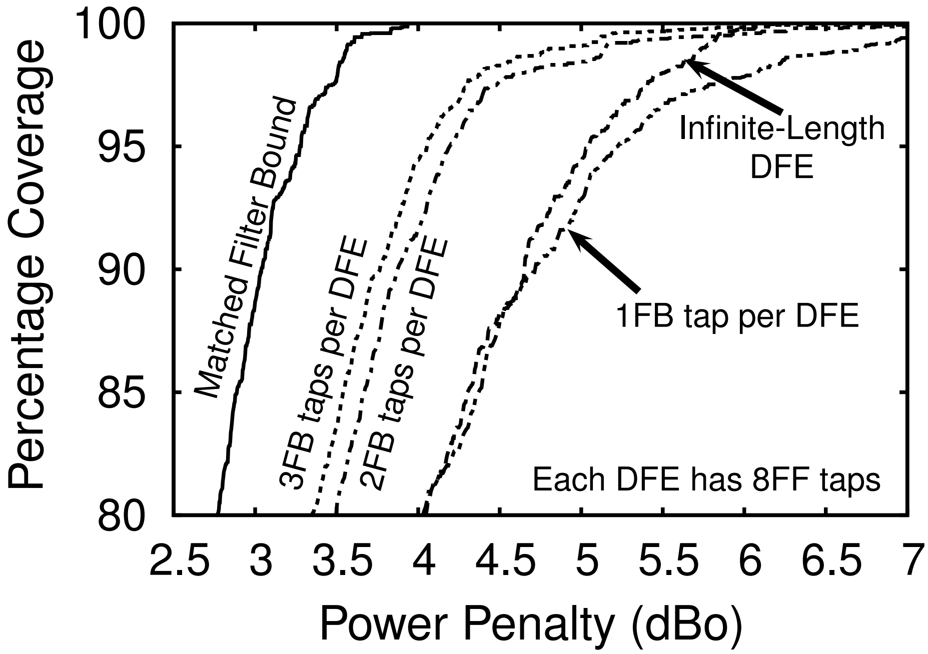

Figure 4.9: Impact of reducing the number of feedback taps on the jointly optimized BiDFE performance. Each constituent DFE has 8 ($T/2$-spaced) feed-forward taps.

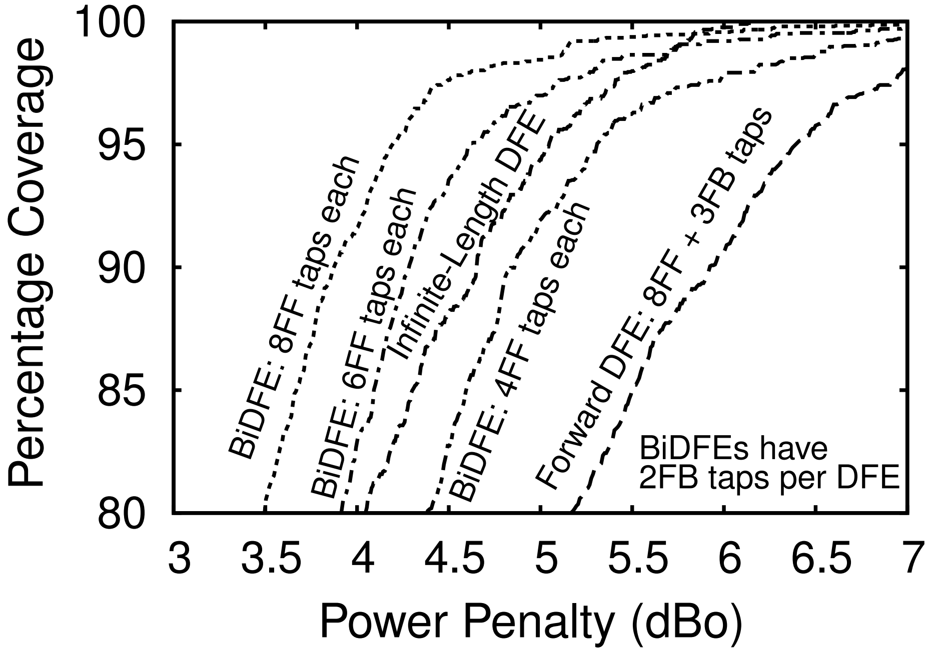

Figure 4.10: Impact of reducing the number of feed-forward taps on the jointly optimized BiDFE performance. Each constituent DFE has 2 feedback taps. The coverage curve for the 8 FF + 3 FB tap forward DFE is included for comparison purposes.

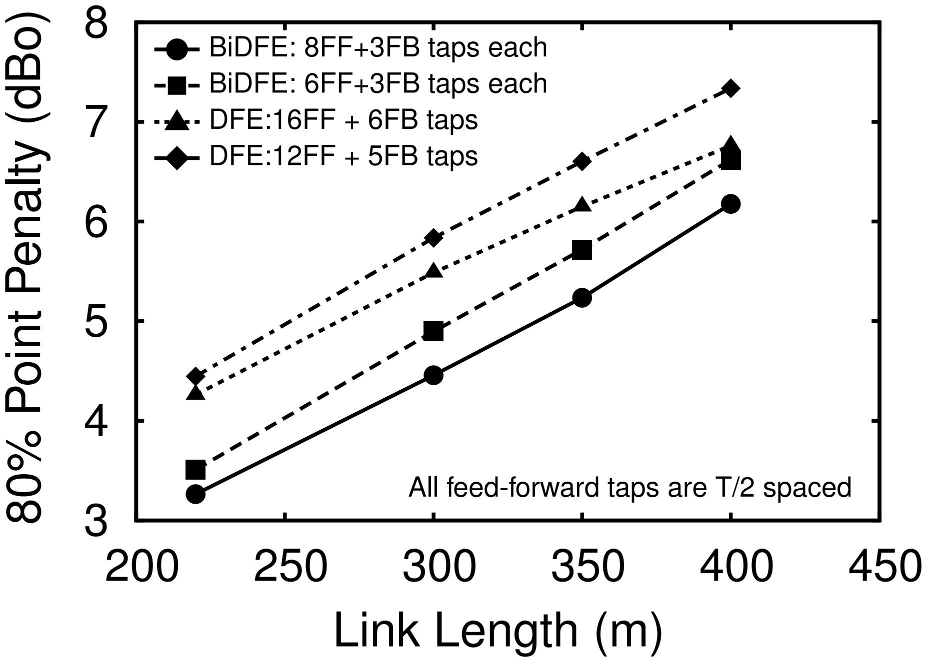

Figure 4.11: Link length extension with the jointly optimized BiDFE.

them better to yield superior performance the forward DFE. A further example is the case of the 4 FF + 2 FB tap BiDFE which performs 0.8 dBo better than the 8 FF + 3 FB tap forward DFE.

Although these examples do not constitute a rigorous proof, they do indicate that the BiDFE utilizes the available filter coefficients in a more efficient manner than the conventional (forward) DFE. Therefore, achieving a BER of 10^{-12} or lower is easier with two short DFEs configured as the BiDFE than one long forward DFE for multi-mode fiber links.

4.5 Can reach be extended to 300m?

In this section, we explore the possibility of link length extension using the jointly optimized BiDFE. We consider BiDFEs with constituent DFEs that are feasible with current technology [16]. Specifically, we evaluate the performance of BiDFEs with 3 FB taps per DFE and six or eight ($T/2$) feed-forward taps per DFE.

Figure 4.11 shows the power penalty at the 80% coverage point of the 108-fiber set with two connectors in the link. We have also included the 12 FF + 5 FB tap DFE and 16 FF + 6 FB tap DFE for comparison purposes. The BiDFE with 6 FF + 3 FB taps per DFE has a penalty of 5.7 dBo for a 350m long link. Using two additional FF taps per DFE allows the BiDFE to equalize even a 400m link with a penalty of 6.2 dBo. In contrast, the 12 FF + 5 FB tap DFE has a penalty of 5.8 dBo at 300m. The 16 FF + 6 FB tap DFE has the same number of coefficients as the BiDFE with 8 FF + 3 FB taps per DFE. Even such a long DFE does not support a reach of 400m since the penalty is 6.8 dBo. Clearly, the jointly optimized BiDFE permits a reach in the 350-400m range compared to only 220-300m for the conventional DFE with comparable complexity.

CHAPTER V

CAPACITY OF OPTICAL INTENSITY CHANNELS

Thus far we have considered the practical problem of equalizing multi-mode fiber links. In this chapter, we will determine the channel capacity of intensity modulated channels. Such a figure of merit establishes fundamental communication limits for such channels and also enables a quick comparison of different transmission schemes as will be done in the next chapter. After establishing how intensity channels are different from conventional electrical channels such as wired and wireless links, we proceed to estimate a lower bound on the capacity.

5.1 Capacity of the band-limited, AWGN Channel

At an intuitive level, channel capacity is the maximum rate at which bits can be sent across a noisy channel with arbitrarily low probability of error. Exploration of the fundamental transmission limits of communication channels began with the seminal work of Shannon [69].

Consider a channel with bandwidth W that does not result in any inter-symbol interference. The transmit signal $x(t)$ and the corresponding received signal $r(t)$ are then related by :

$$r(t) = x(t) + \eta(t) \tag{5.1}$$

where $\eta(t)$ is additive, white, Gaussian noise of power spectral density $N_0/2$. The capacity of such a channel assuming an average electrical transmit power P_{av} is then given by [70]:

$$C(W) = W \log_2 \left[1 + \frac{P_{av}}{N_0 W} \right] \quad \text{bits/sec} \tag{5.2}$$

This capacity is achieved when $1/(2W)$-spaced samples of $x(t)$ have a Gaussian distribution, thereby implying both positive and negative values for the transmit waveform, $x(t)$.

This is the case with wired and wireless channels. Unfortunately, this assumption is not true for intensity modulated optical channels. In this case, the transmit waveform is constrained to be non-negative.

Furthermore, the capacity of equation (5.2) was derived by assuming that the transmitter was constrained to a maximum electrical power of P_{av}, which is a function of the mean of $|x(t)|^2$. In contrast, optical channels have a constraint on the average optical power which is proportional to the mean of $x(t)$.

In view of these two differences, the channel capacity of equation (5.2) is not directly applicable to intensity modulated optical channels.

5.2 Intensity Modulated Optical Channels

Various researchers have investigated the problem of determining the capacity of intensity modulated channels when the non-negativity and average optical power constraints are imposed.

You and Kahn [71] consider a subcarrier modulation (SCM) scheme together with the non-negativity and average optical power constraints. They assume that each of the subcarriers uses quadrature amplitude modulation (QAM) signaling. During each symbol period, the non-negativity constraint restricts the transmit vector to belong to certain trigonometric moment spaces, which will be defined later. An upper bound on the mutual information for such a transmission scheme is then determined by assuming that the transmit vector is equally likely to lie anywhere in this trigonometric moment space. The asymptotic behavior of this upper bound on the mutual information when the number of subcarriers is increased is then briefly explored in [71]. One limitation of [71] is that only a finite alphabet signaling scheme is investigated. Capacity bounds when the transmit vector can be continuous over the specified trigonometric moment space is not explored. In addition, the transmission scheme uses a fixed bias term, which is equivalent to not allowing the average optical amplitude to vary from symbol to symbol. Such a restriction implies a reduction in capacity since there is one less degree of freedom. This point will be explained in more detailed later.

Hranilovic and Kschischang [72, 73] consider a general framework of time-disjoint signaling, where each symbol is restricted to a duration of T seconds with independent transmission across multiple symbol periods. They also relax the restriction of finite alphabet signaling and determine upper and lower bounds for the capacity of optical intensity channels. The upper bound is estimated using sphere packing arguments similar to those originally used by Shannon [69], but now applied to the trigonometric moment spaces. The lower bound is estimated using the source probability density function (PDF) that maximizes the transmit differential entropy. Finally, convergence of these bounds to the actual capacity of the channel is established [72, 73].

Through examples, Hranilovic and Kschischang illustrate that their capacity bounds depend on the basis set chosen for signaling. One of their examples, the raised-QAM set, is nothing but the subcarrier modulation scheme of [71]. However, only the two subcarrier case is considered in [72,73]. Asymptotic behavior of the capacity bounds when the number of subcarriers is increased is not explored, although it is suggested that there may not be much benefit in doing so. Finally, the capacity upper and lower bounds determined in [72, 73] require extensive numerical computation.

In this research, we will determine lower bounds on the capacity of optical intensity channels. We build on the previous two efforts, with the following differences :

- We will first establish that any time-disjoint signaling scheme can be expressed canonically as a subcarrier modulation scheme. Therefore, capacity for time-disjoint signaling can be estimated by assuming an SCM transmission framework, without loss of generality.

- We relax the assumption of finite alphabet, overcoming the drawback of [71].

- Since optical channels such as multi-mode fiber links operate in the high SNR regime, we will focus only on a lower bound for the capacity. We then determine a capacity lower bound using the max-entropic source PDF with an arbitrary number of subcarriers. It can be shown that the entropy of the received waveform is lower bounded by the entropy of the transmit waveform. This property allows derivation of capacity lower bounds that have closed-form expressions, thereby facilitating a clearer understanding of capacity dependence on various parameters. This is in contrast to the results of Hranilovic and Kschischang [72, 73] where numerical integration is necessary even for the simplest examples.

- We then explore the asymptotic behavior of this lower bound as the number of subcarriers is increased. As we show later, this asymptotic capacity is very similar in form to the capacity given in equation (5.2). The implications of this result are discussed further.

5.3 *Time-Disjoint Signaling and Subcarrier Modulation*

Following the approach of [72, 73], we assume that the transmit waveform $x(t)$ is time-limited to $|t| \leq T/2$ where T is the symbol period :

$$x(t) = 0 \qquad \text{for} \qquad |t| > \frac{T}{2} \tag{5.3}$$

Let $X(f)$ be the corresponding frequency response. From the Nyquist sampling theorem, we know that such an $X(f)$ can be uniquely represented by samples at $T_s = T$:

$$X(f) = \sum_{k=-\infty}^{\infty} X_k \delta\left(f - \frac{k}{T}\right) \bigstar \operatorname{sinc}(fT) \tag{5.4}$$

where $\bigstar$ denotes the convolution operation. Assuming $x(t)$ to be real, we have :

$$x(t) = \begin{cases} \frac{X_0}{T} + \frac{2}{T}\sum\limits_{k=1}^{\infty}\left[X_{k,r}\cos\left(\frac{2\pi kt}{T}\right) - X_{k,i}\sin\left(\frac{2\pi kt}{T}\right)\right] & |t| \leq \frac{T}{2} \\ 0 & |t| > \frac{T}{2} \end{cases} \tag{5.5}$$

where $X_{k,r}, X_{k,i}$ are the real and imaginary parts of X_k. This is similar to equation (5) from [71] and is nothing but subcarrier modulation. Thus, time-disjoint signaling is equivalent to subcarrier modulation.

It is straight-forward to show that :

$$X_k = \int_{-T/2}^{T/2} x(t) \exp\left(-\frac{j2\pi kt}{T}\right) dt, \qquad k = 0, 1, 2, \ldots \tag{5.6}$$

Clearly, to satisfy the non-negativity constraint, $x(t) \geq 0$, only certain combinations of X_k's are permitted in each symbol period T. This admissible region of the transmit vector $[X_k]_{k=0}^{\infty}$ is called the *trigonometric moment space* in [71] and is defined as :

$$\chi = \left\{ [X_k]_{k=0}^{\infty} : \quad x(t) \geq 0, \quad X_k = \int_{-T/2}^{T/2} x(t) \exp\left(-\frac{j2\pi kt}{T}\right) dt \right\} \tag{5.7}$$

We will restrict ourselves to a finite number of subcarriers, say K including the DC term X_0. This condition will be relaxed later when the asymptotic behavior of the capacity bound is explored. We can parametrize the non-negativity constraint in terms of X_0 as follows :

$$\Gamma_{X_0} = \left\{ (X_1, X_2, \ldots, X_{K-1}) \ : \sum_{k=1}^{K-1} \mathscr{R}e \left\{ X_k \exp\left(\frac{j2\pi kt}{T}\right) \right\} \geq -\frac{X_0}{2}; \quad |t| \leq \frac{T}{2} \right\} \tag{5.8}$$

One can visualize Γ_{X_0} as a cross-section of the trigonometric moment space χ. As shown later, what is more important is the volume, $V(\Gamma_{X_0})$, of the space Γ_{X_0}. It can be shown that [73] :

$$V(\Gamma_{X_0}) = V(\Gamma_1) X_0^{2(K-1)} \tag{5.9}$$

where the volume $V(\Gamma_1)$ is given by [71] :

$$V(\Gamma_1) = \frac{(2\pi)^{K-1}(K-1)!}{(2K-2)!} \tag{5.10}$$

The average optical power at the transmitter can be expressed as :

$$P_{opt.} = E\left[\frac{1}{T} \int_{-T/2}^{T/2} x(t) dt \right] \tag{5.11}$$

which is equivalent to :

$$E[X_0] = P_{opt}.T \tag{5.12}$$

Thus the optical power depends on only the DC term X_0 and not on the other subcarriers.

Hranilovic and Kschischang [72,73] define bandwidth as the band of frequencies where 99% of the signal energy is concentrated. However, we will use a more practical definition of bandwidth which is related to spectral nulls. From equation (5.4) it is clear that there are nulls at $\pm 1/T$ above and below each subcarrier, resulting in a bandwidth of $1/T$ for each subcarrier. Therefore, with K subcarriers, the bandwidth of the SCM scheme is :

$$W = \frac{K}{T} \tag{5.13}$$

This is similar to the definition used in [71].

5.4 Receiver Structure and Noise Statistics

The transmit waveform is then corrupted by additive white Gaussian noise in the channel. The corresponding received waveform is again given by equation (5.1). The receiver front-end simply extracts the noisy estimates of X_k required for the detection process. Such a front-end can be mathematically described as follows :

$$Y_k = \int_{-T/2}^{T/2} y(t) \exp\left(-\frac{j2\pi kt}{T}\right) dt, \qquad k = 0, 1, 2, \ldots \tag{5.14}$$

$$= X_k + N_K \tag{5.15}$$

where N_k is given by :

$$N_k = \int_{-T/2}^{T/2} \eta(t) \exp\left(-\frac{j2\pi kt}{T}\right) dt \tag{5.16}$$

Since $\eta(t)$ is assumed to be real, white and Gaussian with zero mean and power spectral density $N_0/2$, it can be shown that for $k \geq 1$, the samples N_k are independent and identically distributed and complex with zero mean and variance $N_0T/2$. Therefore, the real and imaginary components of N_k have a variance $N_0T/4$ when $k \geq 1$. The sample N_0 is also independent of the other noise samples but is real, with variance $N_0T/2$.

The detection process then reduces to choosing the appropriate transmit vector $\mathbf{X}$ given the received vector $\mathbf{Y}$:

$$\underbrace{\begin{bmatrix} Y_0 \\ Y_{1,r} \\ Y_{1,i} \\ \vdots \\ Y_{K-1,r} \\ Y_{K-1,i} \end{bmatrix}}_{\mathbf{Y}} = \underbrace{\begin{bmatrix} X_0 \\ X_{1,r} \\ X_{1,i} \\ \vdots \\ X_{K-1,r} \\ X_{K-1,i} \end{bmatrix}}_{\mathbf{X}} + \underbrace{\begin{bmatrix} N_0 \\ N_{1,r} \\ N_{1,i} \\ \vdots \\ N_{K-1,r} \\ N_{K-1,i} \end{bmatrix}}_{\mathbf{N}} \tag{5.17}$$

5.5 Channel Capacity

The reduction from a waveform channel to a discrete-time channel, equation (5.17), enables the use of several tools from information theory. The capacity of such a channel is given by [69] :

$$C = \frac{1}{T} \sup_{f_{\mathbf{X}}, \mathbf{X} \in \chi} I(\mathbf{X};\mathbf{Y}) \quad \text{bits/sec} \tag{5.18}$$

where the supremum is taken over all probability distributions of $\mathbf{X}$, $f_{\mathbf{X}}$, that satisfy the non-negativity constraint. Since the noise is independent of the transmit vector, we use following expression for the mutual information $I(\mathbf{X};\mathbf{Y})$:

$$I(\mathbf{X};\mathbf{Y}) = h(\mathbf{Y}) - h(\mathbf{N}) \tag{5.19}$$

where $h(\mathbf{N})$ is the differential entropy of the noise. Definitions of differential entropy, mutual information and channel capacity are provided in Appendix D along with an intuitive explanation. The entropy power inequality implies that [70] :

$$h(\mathbf{Y}) \geq h(\mathbf{X}) \tag{5.20}$$

Therefore, a lower bound for the capacity is given by :

$$C \geq \frac{1}{T} \sup_{f_{\mathbf{X}}, \mathbf{X} \in \chi} [h(\mathbf{X}) - h(\mathbf{N})] \tag{5.21}$$

Clearly, this capacity lower bound is maximized for the PDF $f_{\mathbf{X}}$ that maximizes the differential entropy of the transmit vector $\mathbf{X}$. Following the notation of [72, 73], we denote the transmit vector corresponding to such a max-entropic distribution by $\mathbf{X}^*$. Therefore, the capacity lower bound reduces to :

$$C \geq \frac{1}{T} [h(\mathbf{X}^*) - h(\mathbf{N})] \quad \text{bits/sec} \tag{5.22}$$

5.6 Max-Entropic Source Distribution

In this section, we determine the probability density that maximizes the entropy of the transmit vector $\mathbf{X}^*$ given the non-negativity and average optical power constraints. This problem can be mathematically expressed as :

$$\text{Maximize } h(\mathbf{X}) = -\underset{\mathbf{X} \in \chi}{\int \cdots \int} f_{\mathbf{X}} \log_2 [f_{\mathbf{X}}] \, d\mathbf{X} \tag{5.23}$$

$$\text{subject to } \underset{\mathbf{X} \in \chi}{\int \cdots \int} f_{\mathbf{X}} d\mathbf{X} = 1 \tag{5.24}$$

$$\text{and } \quad \underset{\mathbf{X} \in \chi}{\int \cdots \int} X_0 f_{\mathbf{X}} d\mathbf{X} = P_{opt} T \tag{5.25}$$

Using the method of Lagrange multipliers and equations (5.9) and (5.10), it can be shown that the entropy maximizing distribution $f_{\mathbf{X}}$ is given by :

$$f_{\mathbf{X}}(\mathbf{X}) = C e^{-\alpha_0 X_0} \tag{5.26}$$

$$C = \frac{\alpha_0^{2K-1}}{(2K-2)! V(\Gamma_1)} \tag{5.27}$$

$$\alpha_0 = \frac{2K-1}{P_{opt} T} \tag{5.28}$$

Thus the transmit vector $\mathbf{X}$ has an exponential distribution. The corresponding entropy is then :

$$h(\mathbf{X}^*) = \log_2 \left[\frac{e^{2K-1}}{C} \right] \tag{5.29}$$

From equations (5.10),(5.27) and (5.28), we have :

$$h(\mathbf{X}^*) = \log_2 \left[\frac{(P_{opt}Te)^{2K-1}(2\pi)^{K-1}(K-1)!}{(2K-1)^{(2K-1)}} \right] \quad \text{bits/symbol} \tag{5.30}$$

5.7 Capacity Lower Bound

Using the noise statistics from section 5.4, the differential entropy of the noise vector $\mathbf{N}$ can be shown to be :

$$h(\mathbf{N}) = \log_2 \left[\frac{(\pi N_0 Te)^{K-\frac{1}{2}}}{2^{K-1}} \right] \quad \text{bits/symbol} \tag{5.31}$$

Therefore from equations (5.22),(5.30) and (5.31), the capacity lower bound can be expressed as :

$$C \geq \frac{1}{T} \log_2 \left[\left(\frac{P_{opt}^2 Te}{N_0} \right)^{K-\frac{1}{2}} \cdot \frac{2^{2K-2}(K-1)!}{\sqrt{\pi}(2K-1)^{(2K-1)}} \right] \quad \text{bits/sec} \tag{5.32}$$

Using Stirling's approximation, $n! \approx \sqrt{2\pi n} n^n / e^n$, this bound reduces to :

$$C \geq \frac{1}{T} \log_2 \left[\left(\frac{P_{opt}^2 T}{N_0 K} \right)^{K-\frac{1}{2}} \cdot \sqrt{\frac{e}{2}} \cdot \frac{\left(1-\frac{1}{K}\right)^{K-\frac{1}{2}}}{\left(1-\frac{1}{2K}\right)^{2K-1}} \right] \quad \text{bits/sec} \tag{5.33}$$

Since the bandwidth $W = K/T$, it follows that :

$$C \geq W \log_2 \left[\left(\frac{P_{opt}^2}{N_0 W} \right)^{1-\frac{1}{2K}} \cdot \left(\frac{e}{2}\right)^{\frac{1}{2K}} \cdot \frac{\left(1-\frac{1}{K}\right)^{1-\frac{1}{2K}}}{\left(1-\frac{1}{2K}\right)^{2-\frac{1}{K}}} \right] \quad \text{bits/sec} \tag{5.34}$$

Thus we have derived a closed-form expression for the capacity lower bound with arbitrary number of subcarriers. The term $P_{opt}^2/(N_0 W)$ is the equivalent electrical signal-to-noise ratio (SNR). The spectral efficiency is nothing but C/W with units of bits/sec per Hz.

Unlike the results of Hranilovic and Kschischang [72, 73], dependence on the SNR and the number of subcarriers is explicitly available and does not require any numerical integration. The variation of the capacity with the number of subcarriers can be explained via two effects: i) the exponent $1 - 1/(2K)$ of the SNR and ii) a multiplier made up of the remaining terms in the argument of the logarithm in equation (5.34). This multiplier lies in the range (1,1.08) independent of the number of subcarriers. Therefore, the dominant effect is due to the exponent and so the capacity bound can be further approximated as :

$$C \geq W \cdot \left(1 - \frac{1}{2K}\right) \cdot \log_2 \left[\frac{P_{opt}^2}{N_0 W}\right] \quad \text{bits/sec} \tag{5.35}$$

It can be concluded that the capacity does increase with increasing number of subcarriers K. However, the capacity increment decreases inversely with $K^2 + K$.

In the limit of infinite number of subcarriers, the capacity bound of equation (5.34) approaches :

$$C_{LB} = W \log_2 \left[\frac{P_{opt}^2}{N_0 W}\right] \quad \text{bits/sec} \tag{5.36}$$

Therefore, every 3 dB increase in the equivalent electrical SNR results in an increase of 1 bits/sec/Hz in the spectral efficiency.

Going back to the band-limited, AWGN channel of equations (5.1) and (5.2), the capacity at high SNR is given by :

$$C_{AWGN} \approx W \log_2 \left[\frac{P_{av,AWGN}}{N_0 W}\right] \quad \text{bits/sec} \tag{5.37}$$

Note that the SNR in this case is $P_{av,AWGN}/(N_0 W)$. Therefore, the capacity of the intensity modulated optical channel and the conventional band-limited, AWGN channel are identical at high SNR, provided that the SNR is defined appropriately in both cases.

5.8 Summary

In this chapter, we have determined a lower bound for the capacity of intensity modulated optical channels. The closed-form nature of the bound permits easier analysis of the capacity variation than that possible with the bounds considered in [72, 73]. This bound implies that for any intensity modulated optical channel, we only need to determine the equivalent electrical SNR and directly use the capacity expression for the conventional band-limited, AWGN channel. This bound asymptotically converges to the actual channel capacity at high SNR.

We point out that capacity estimation for intensity channels in the presence of intersymbol interference is an open problem. One simple upper bound on the capacity can be determined by directly using the capacity expressions for a conventional (electrical) ISI channel, but with the equivalent electrical SNR. Based on the results of this chapter, we believe that such a bound can at least be used for comparing different transmission systems, as will be discussed in the next chapter. However, analysis of the tightness of such a bound is beyond the scope of the present research.

CHAPTER VI

MIMO CHARACTERIZATION & EQUALIZATION OF MMF LINKS

The multi-mode fiber links considered thus far have a single source of excitation and a single photo-detector that collects the received light, and so can be classified as single-input, single-output (SISO) channels. In this chapter, we formulate a multiple-input, multiple-output (MIMO) characterization of the multi-mode fiber channel. We establish the potential benefits of such a transmission scheme over the conventional SISO system using channel capacity bounds. We further investigate equalization of such MIMO-MMF links using a MIMO version of the DFE.

6.1 MMF Links as MIMO channels

Although 10 Gbps transmission over MMF links is challenging, there is already a push for higher data rates, even as high as 100 Gbps [24]. The most common approach being discussed is parallel transmission where a ribbon cable with ten fibers, each supporting a serial data rate of 10 Gbps, will be employed. While putting together such a system is relatively easy, it is likely to be expensive. Before embarking on a parallel solution, a fundamental question needs to be addressed. Has the upper limit of transmission over a single multi-mode fiber been reached?

As discussed earlier, light travels along multi-mode fiber via different propagation modes, which are orthogonal to each other. These modes are not unlike the multi-path environment that typically characterizes wireless channels. The diversity provided by these multiple paths has been exploited in wireless systems to increase the data rate and/or improve link reliability through the use of multiple transmit and receive antennas [74]. Such a channel characterization is known as a *multiple-input, multiple-output* (MIMO) channel. In principle, one can can increase the data rate by transmitting a separate data stream via each mode and detecting it separately at the receiver.

The first parallel between the multi-mode fiber channel and wireless systems was drawn by Stuart [25] where the advantages of MIMO processing in the context of MMF links were demonstrated. The experiment involved driving multiple lasers with modulated RF carriers and then coupling the laser outputs to the multi-mode fiber via splitters. Coherent detection at the receiver using multiple photo-detectors retrieves the RF signal which is demodulated to arrive at the final baseband signals. Further signal processing is done numerically via software. Yet another effort involving coherent detection is that of Shah et al [26, 75, 76]. Another common feature of these research efforts is that they operate at a sufficiently low symbol rate such that the channel response is *not* frequency selective. In other words, all the mode groups arrive within a symbol period. Since coherent detection is employed, the channel response between transmitter m and receiver n can then be modeled by a single complex number, h_{mn}. Thus high data rates are achieved, in principle, through a combination of coherent detection, advanced modulation schemes and MIMO processing. Although such a formulation has been shown to result in linear growth in channel capacity with increasing number of transmit/receive antennas in wireless systems [77], the additional complexity is significant for MMF links. Therefore, we propose to investigate the benefits of MIMO processing in the multi-mode fiber context with minimal changes to the existing links.

6.1.1 Multiple Inputs via Multiple Launch Offsets

We have already seen that bad center launch performance is correlated with good offset launch performance (and vice versa) for quite a few multi-mode fibers. Indeed, joint launch exploits this correlation in performance through the optimal selection of the launch condition. In this research, we generalize the launch further by proposing simultaneous use of

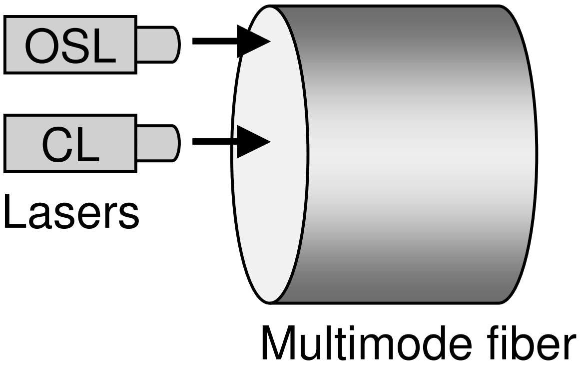

Figure 6.1: Multiple inputs via multiple launch offsets.

both CL and OSL, Fig. 6.1. In order to maintain the same aggregate data rate ($1/T$) each launch will operate at $1/(2T)$.

6.1.2 Multiple Outputs via Multi-Segment Photodetector

It is well known that the lower order mode groups propagate closer to the fiber axis than the higher order mode groups [40]. A multi-segment photo-detector that exploits this inherent spatial diversity of the mode groups was proposed by Miller [78]. In the case of the two-segment photo-detector, the lower order mode groups are primarily collected by the inner photo-detector while the higher order mode groups are collected by the outer photo-detector, Fig. 6.2. After the initial patent on multi-segment detectors, no further performance characterization was reported in the open literature till the recent efforts by Patel et al [7, 27–33, 45], where a two-segment photo-detector was fabricated. Such a device is called the *spatially resolved equalizer* (SRE) [31, 33]. A multimode fiber link using such a detector can be viewed as a 1×2 system, since there is one input data stream and two output photo-currents. While further electronic processing of the photo-currents from the multi-segment detector is possible, simple subtraction of the photo-currents results in a channel response with less ISI. Such an implementation of the two-segment detector is called the *SRE with subtraction*. Further performance improvements can be realized by employing an electronic equalizer after the SRE [34]. Optimal combining of the inner and

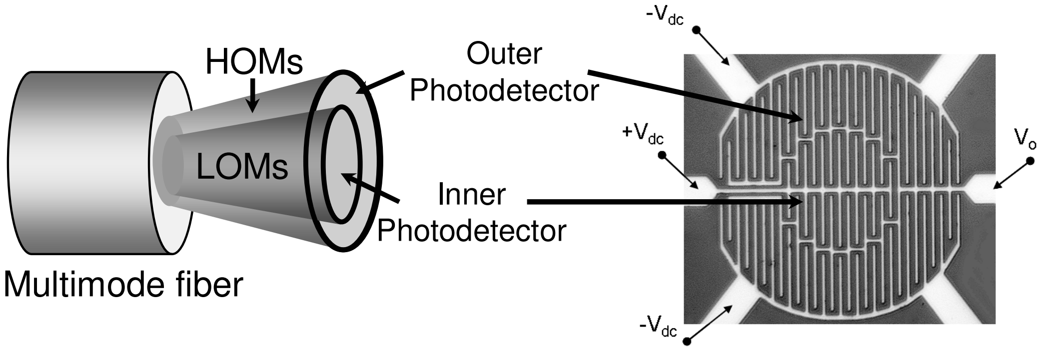

Figure 6.2: Spatial diversity and the two-segment photo-detector. The lower order mode groups (LOMs) are primarily collected by inner photo-detector whereas the higher order mode groups (HOMs) are collected by the outer photo-detector.

outer photo-detector outputs together with equalization has been shown to result in improved performance for over-filled launch [36]. In this research, such a receiver will be referred to as the *SRE with combiner*.

Subsequent to our research group's work on practical multi-segment photo-detectors, they were once again proposed in [79, 80] as a source of receive diversity. Furthermore, the multi-segment detector proposed in [80] intentionally introduces gap between the inner and outer segments. Although the resulting ISI spans fewer bits, the associated power loss is expected to impact the overall performance significantly.

In this research, we propose the simultaneous use of center and offset launch together with the two-segment detector discussed earlier, Fig. 6.3. The two launches couple optical power into different mode groups. Similarly, the two segments of the photo-detector collect power from different mode groups. The photo-currents from these two segments are then amplified (via the TIA) and further processed electronically. Such a system effectively has two transmit "antennas" and two receive "antennas". Although the number of launches and number of segments in the photo-detector can be increased, we believe the best trade-off between cost and performance is obtained for the configuration in Figure 6.3. We point out that this MIMO system is significantly less complex than the coherent detection schemes discussed earlier [25, 26, 75, 76].

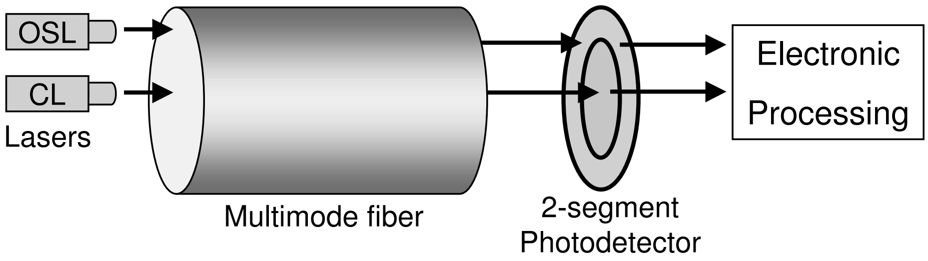

Figure 6.3: Multiple-input, multiple-ouptut (MIMO processing of multi-mode fiber links.

Yet another approach to improving the performance of MMF links is to selectively excite only the desired modes via spatial light modulators (SLM) [81]. This technique has been generalized to include the MIMO processing of MMF links by allocating sets of desired mode groups to separate channels. The desired mode groups are chosen to minimize the differential delay and/or create parallel channels in the case of MIMO processing. Conceptually, the use of SLMs for finer control of the modes is the limiting case of launch diversity where sets of mode groups are excited selectively. Clearly, the SLM approach is significantly more complex than the MIMO scheme shown in Fig. 6.3. Furthermore, we believe that the choice of the desired mode groups and the associated optimization become complicated when non-ideal effects such as index perturbations, connector offsets, fiber eccentricity, and micro-bending are considered.

One simple way of increasing the throughput of MMF links is to use parallel fibers, possibly in the form of ribbon cables. While this approach does not require any sophisticated technology, the cost does go up linearly with the number of parallel links. Another straightforward approach is the simultaneous use of multiple wavelengths on the same fiber [82]. Since these techniques can always be used in conjunction with MIMO processing of serial MMF links, we will not consider them in this research.

6.2 Capacity of MMF Links

In this section, we use channel capacity as a figure of merit to compare the MIMO system with the conventional single-input, single-output multimode fiber link. In addition to providing a quick estimate of the potential benefits of MIMO processing, such a measure establishes fundamental limits of the proposed scheme.

A general MIMO system with M_t transmit and M_r receive antennas can be mathematically formulated as :

$$r_i(t) = \sum_{j=1}^{M_t} h_{i,j}(t) \bigstar a_j(t) + n_i(t) \tag{6.1}$$

where $a_j(t)$ is the transmit waveform at the j^{th} antenna, $r_i(t)$ is the received waveform at the i^{th} antenna and $n_i(t)$ is the corresponding additive white gaussian noise. Such a MIMO system is shown in Figure 6.4. We assume that the noise at each of the receivers is independent of the other branches and has a power spectral density of $N_0/2$. The channel response from the j^{th} transmit antenna to the i^{th} receive antenna is denoted by $h_{i,j}(t)$. In the context of multimode fiber links, $h_{i,j}(t)$ is defined by the modal delays and the mode power distribution (MPD) for this transmission path. Given the launch offset and the radius of the inner and outer photo-detectors along with any gap between these two segments, the mode solver developed as part of this research can compute the MPD for $(j,i)^{th}$ path.

The capacity of the (M_t, M_r) frequency-selective MIMO channel can be shown to be [74, 83]:

$$C(W) = \int_0^W \log_2 \left[\det \left(I_{M_r \times M_r} + \frac{1}{M_t} \cdot \frac{P_{av}}{N_0 W} \cdot H(f) H^*(f) \right) \right] df \quad \text{bits/sec} \tag{6.2}$$

where W is the allocated bandwidth, P_{av} is the average (equivalent electrical) transmit power summed over all transmit antennas and $H(f)$ is the Fourier transform of the matrix representation of the channel :

$$H(f) = \mathscr{F} \left\{ \begin{bmatrix} h_{1,1}(t) & h_{1,2}(t) & \cdots & h_{1,M_t}(t) \\ h_{2,1}(t) & h_{2,2}(t) & \cdots & h_{2,M_t}(t) \\ \vdots & \vdots & \ddots & \vdots \\ h_{M_r,1}(t) & h_{M_r,2}(t) & \cdots & h_{M_r,M_t}(t) \end{bmatrix} \right\} \tag{6.3}$$

Note that $H(f)$ is a matrix of size $M_r \times M_t$. and $H^*(f)$ denotes the conjugate transpose of $H(f)$. Also the determinant of any matrix A is denoted by $\det(A)$. This capacity was

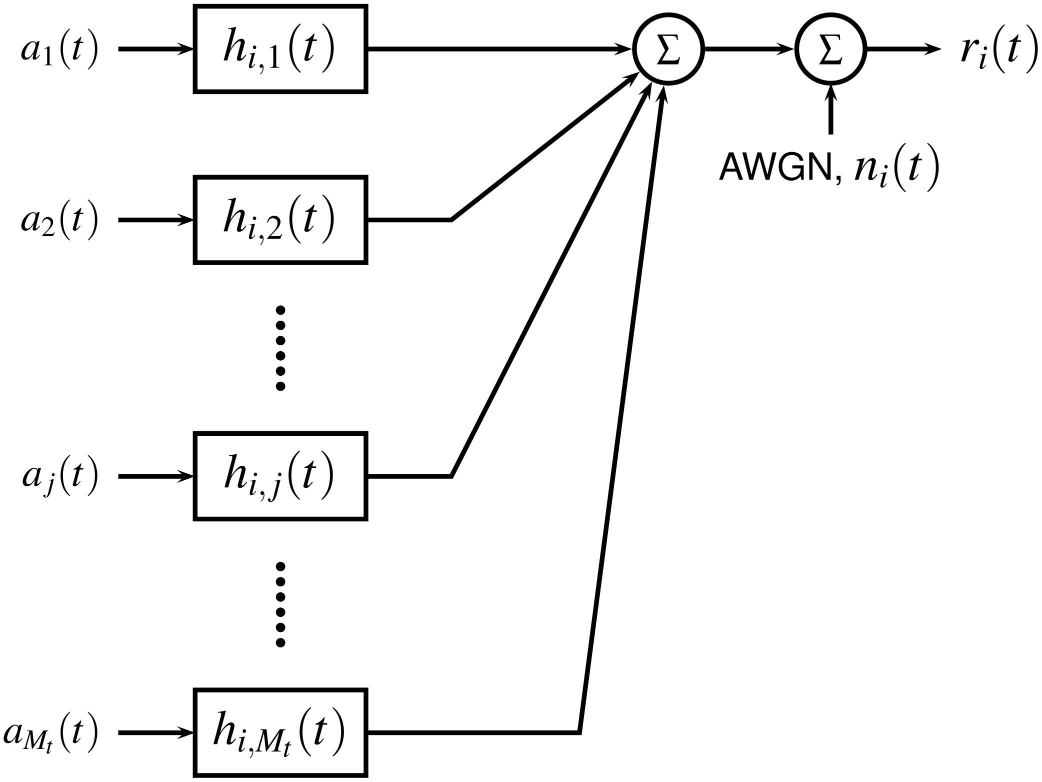

Figure 6.4: Mathematical representation of the MIMO system with M_t transmit antennas and M_r receive antennas.

determined by dividing the channel response into non-overlapping frequency bins. The bins are sufficiently narrow that the frequency response in each bin can be assumed to be flat. This capacity formulation assumes that the transmitter does not have any channel state information available and therefore the best it can do is to allocate equal power to each frequency bin and to each transmit antenna. At the same time, this capacity is very close to that arrived by optimal power allocation, particularly for high signal-to-noise ratios which is the case for MMF links. As explained in the previous chapter, this capacity serves as an upper bound on the actual capacity of intensity modulated optical channels and is used only for comparison purposes.

Using the relationship between average transmit power and the operating SNR from equation (B.9), we get :

$$C(W) = \int_0^W \log_2 \left[\det \left(I_{M_r \times M_r} + \frac{1}{M_t} \cdot \frac{SNR_r}{2WT_r} \cdot H(f)H^*(f) \right) \right] df \quad \text{bits/sec} \tag{6.4}$$

The bandwidth W is chosen to be the same as that of the reference channel for MMF links. Since the ISI-free channel uses ideal rectangular pulse shapes, its bandwidth is nominally $1/T_r$. Therefore, $W = 1/T_r$ even for the MIMO system. Note that for the 10 Gbps Ethernet system, $W = 10.3125$ GHz and $SNR_r \approx 30$ dBe, Appendix B.

In the following analysis, we denote the capacity of the capacity of the single-segment detector based link (1×1 system) by C_{SPD}, the capacity of the SRE based link (1×2 system) C_{SRE} and the capacity of the SRE link with photo-current subtraction (1×1 system) by $C_{SRE+Sub.}$. The capacity of the two input, two output system is denoted by C_{MIMO}.

6.2.1 Capacity for the 108 Fiber Set

We are now in a position to determine the capacity for the 108 fiber set. Each link is 220m long with two connectors at the transmit end. The mode solver was used to determine the mode power distributions for the 108 fibers with the proposed MIMO system. We assume that the two-segment photo-detector is coupled directly to the receive end of the fiber and has an inner photo-detector radius of 10μm. In practical realizations, the size of the inner

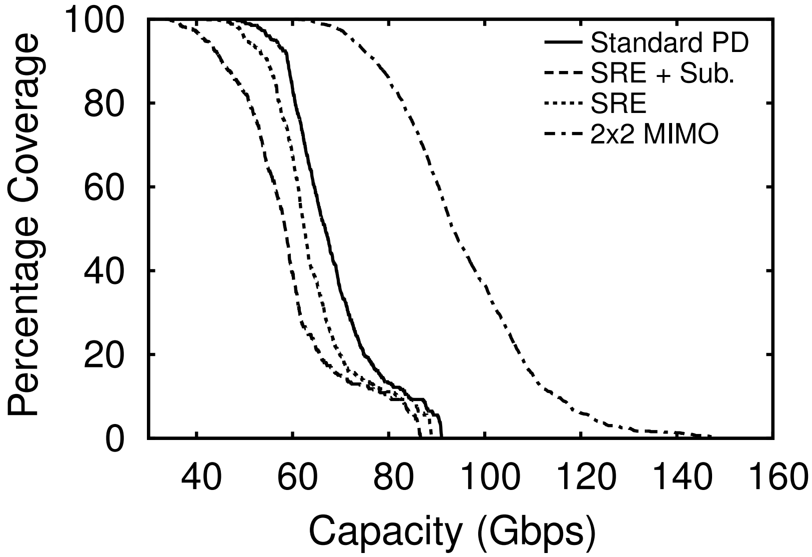

Figure 6.5: Cumulative distribution of the capacity of MMF Links for various transceivers. Each link is 220m long and has two connectors at the transmit end.

detector can be adjusted proportionately to accommodate a larger spacing between the fiber and the photo-detector thereby resulting in almost the same performance.

Figure 6.5 shows the capacity coverage curves for four types of transceivers: the standard system, the SRE, the SRE with photo-current subtraction, and the 2×2 MIMO system. The capacity curves for the standard and the SRE based links correspond to joint launch. Note that the y-axis denotes the percentage of links with capacity less than the abscissa.

Consistent with our worst-case design philosophy, we use the capacity at the 80% coverage point to compare the various transmission schemes. The standard 1×1 system has a 80% coverage capacity of $\approx$ 60 Gbps while the SRE has a capacity of $\approx$ 57 Gbps. The SRE with photo-current subtraction reduces the capacity further to 50 Gbps. The superior performance of the 2×2 MIMO channel is clearly demonstrated by its 80% coverage capacity of 83 Gbps. Interestingly, both SRE based systems have smaller capacities than the standard 1×1 system. Although we have shown the coverages curves for the joint launch case, this observation holds for center launch and offset launch individually also.

6.3 Equalization of MIMO MMF Links

Having established the potential benefits of MIMO processing for MMF links from a channel capacity point of view, we next consider practical receiver structures.

6.3.1 Spatially Resolved Equalizer with Optimal Combining

The spatially resolved equalizer produces two received waveforms both corresponding to the same transmit bit sequence. Each of these received signals exhibits inter-symbol interference caused by modal dispersion. Clearly, further electronic processing is required to efficiently combine the two received waveforms and mitigate the impact of ISI. The SRE with photo-current subtraction is a very basic combiner. Argon et al considered another simple combiner where the output of the inner photo-detector is delayed and added to the output of the outer photo-detector [36]. A conventional decision feedback equalizer was employed after combining the two received waveforms. While significant performance improvement was reported, only one fiber was considered. Furthermore, the fiber data did not correspond to center/offset launch, which are the standard launch conditions in modern MMF links.

In this section, we explore the performance of the SRE with the optimum combiner and decision-feedback equalizer. A thorough statistical assessment of the benefits of the SRE is conducted for center and offset launches using the 108-fiber set.

The optimum diversity combiner with decision feedback equalizer for a 1×2 channel consists of two feed-forward filters, one for each diversity path, followed by the slicer and the feedback filter [84]. In this chapter, we will focus on the performance of infinite-length equalizers. In this case, the optimum combiner/DFE has the structure shown in Figure 6.6. The transmit filter is denoted by $h_{TX}(t)$ and the fiber impulse responses at the two segments of the photo-detector outputs are $h_1(t)$ and $h_2(t)$. Define $g_j(t) = h_{TX}(t) \bigstar h_j(t)$ for $j = 1, 2$. The optimum combiner consists of two matched filters, one for each of the diversity paths,

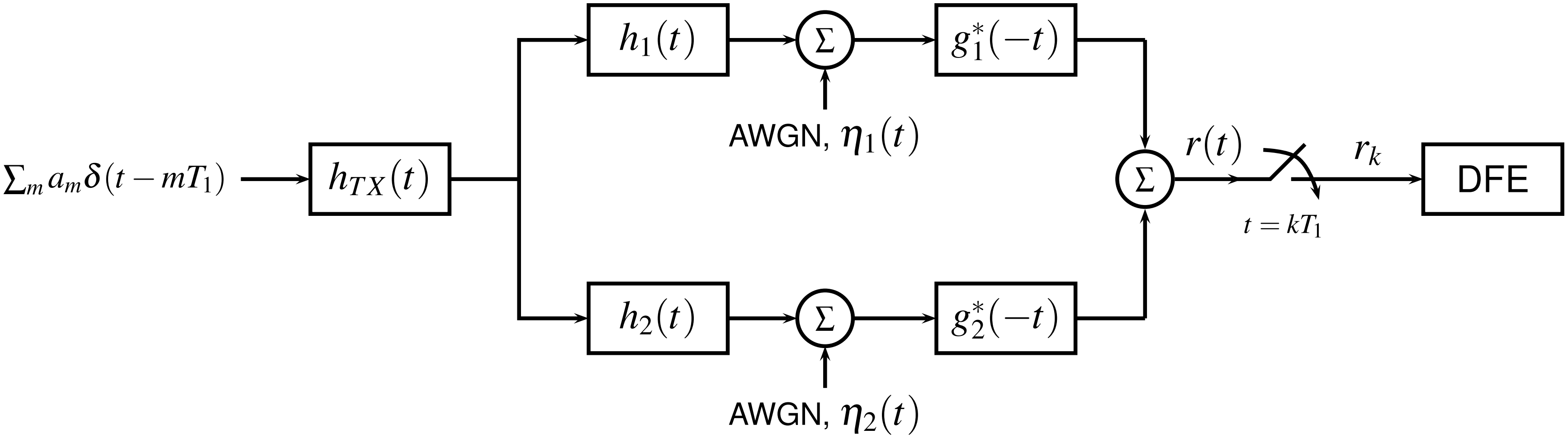

Figure 6.6: Sampled matched filter front-end for the 1×2 SIMO link followed by the infinite-length DFE.

followed by a simple adder. The output of the combiner, $r(t)$, is then given by :

$$r(t) = \sum_m a_m p(t - mT_1) + \nu(t) \tag{6.5}$$

$$p(t) = g_1(t) \bigstar g_1^*(-t) + g_2(t) \bigstar g_2^*(-t) \tag{6.6}$$

$$\nu(t) = \eta_1(t) \bigstar g_1^*(-t) + \eta_2(t) \bigstar g_2^*(-t) \tag{6.7}$$

where $g_i(t) = h_{TX}(t) \bigstar h_i(t)$ for $i = 1, 2$. The T_1-spaced samples of the combiner output are fed to an infinite-length decision feedback equalizer. The power penalty for such a receiver is given by :

$$Penalty_{1\times 2} = \exp\left[-T_1 \int_{-\frac{1}{2T_1}}^{\frac{1}{2T_1}} \ln\left\{ \frac{1}{T_1} \sum_l P\left(f - \frac{l}{T_1} \right) + \frac{N_0}{2\sigma_a^2} \right\} df \right] \tag{6.8}$$

Note that the penalty for the SRE with photo-current subtraction is given by PIE-D defined in equation (3.5).

6.3.2 MIMO Decision Feedback Equalization

One direct advantage of multiplexing two independent data streams via the dual launch is that the ISI for each stream spans fewer bits compared to the non-multiplexed link with the same aggregate data rate. On the other hand, part of the optical power from the modes excited by CL is collected by the outer photo-detector and power from the modes excited by OSL is collected by the inner photo-detector. This will generate co-channel interference (CCI). In order to mitigate the effect of both ISI and CCI in MIMO MMF links, we propose using the MIMO version of the decision feedback equalizer (MIMO-DFE) [85–87]. We will again consider an infinite-length MIMO-DFE. In this case, the optimum front-end is the matched-filter followed by T_2-spaced samplers, the outputs of which are fed to the MIMO-DFE, Fig. 6.7. The feed-forward and feedback filters of the MIMO-DFE jointly process their vectors inputs and so have four filters each.

For the 2×2 system, the MIMO-DFE will result in a different power penalty for each data stream. The performance of the overall system can be reduced to a single figure

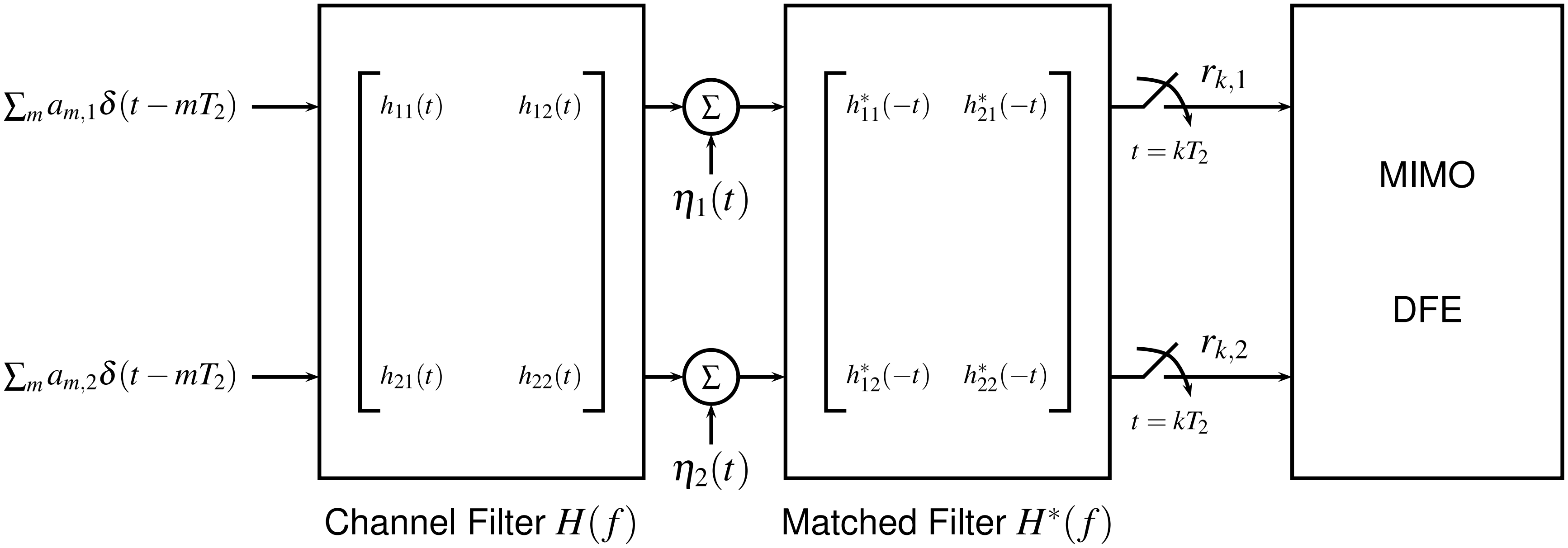

Figure 6.7: Sampled matched filter front-end for the 2×2 MIMO link followed by the infinite-length MIMO DFE.

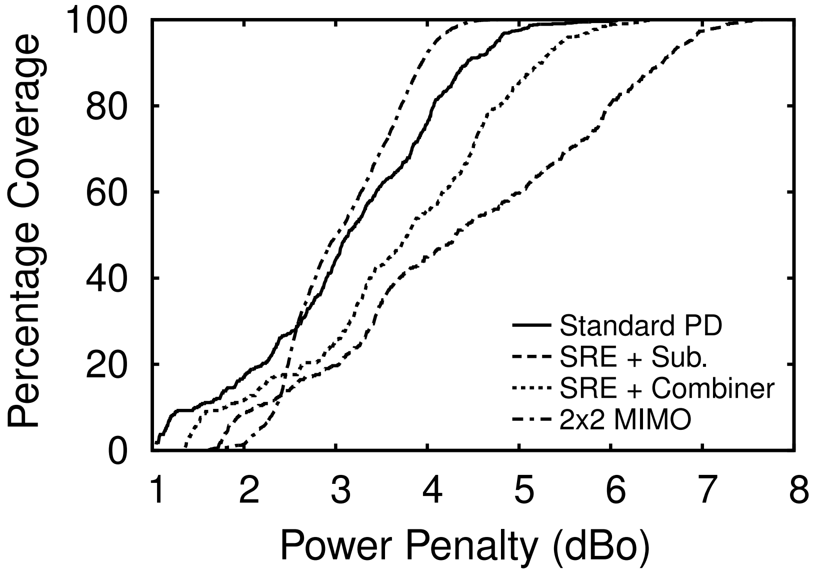

Figure 6.8: Coverage curves for equalization penalty for MIMO links. Each link is 220m long and has two connectors at the transmit end. Curves for the standard link and the SRE based links correspond to joint launch.

of merit using either the arithmetic or the geometric average of these individual penalties. Since the geometric average results in a closed-form expression for the MIMO-DFE penalty, we adopt this approach [85]. In this case, the power penalty is given by :

$$Penalty_{2\times 2} = \frac{1}{\left\{\exp\left[T_2 \int_{-\frac{1}{2T_2}}^{\frac{1}{2T_2}} \ln\left\{\det\left(\frac{1}{T_2}\sum_l P\left(f-\frac{l}{T_2}\right)+\frac{N_0}{2\sigma_a^2}I\right)\right\} df\right]\right\}^{1/2}} \tag{6.9}$$

where $P(f) = H^*(f)H(f)$ and T_2 is the bit period for each data stream.

6.3.3 Equalization Results for 108-Fiber Set at 10 Gbps

We assess the performance of MIMO MMF links at an aggregate data rate of 10 Gbps. Each links is 220m long with two connectors at the transmit end. We determine the power penalty after equalization for the 108-fiber set using each of the three transmission schemes discussed thus far: SRE with subtraction, SRE with optimum combining and the MIMO-DFE. The results are compared with the standard 1×1 system.

Figure 6.8 shows the coverage curves for the equalization penalty for various transmission schemes. We will again use the penalty at the 80% coverage point for comparison purposes. The SRE with photo-current subtraction has an equalized penalty of 6 dBo at the 80% coverage point. As a point of reference, the standard 1×1 link has an 80% coverage point penalty of 4 dBo. Clearly, the SRE with subtraction performs poorly compared to the standard single-segment photodetector. The SRE with combining followed by the infinite-length DFE reduces this penalty to 4.8 dBo at the 80% coverage point, but is still unable to match the performance of the standard 1×1 link.

The 2×2 MIMO system has an equalization penalty of 3.7 dBo at the 80% coverage point, a 0.35 dBo improvement over the standard link with joint launch. The MIMO system reduces the penalty for the "bad" links where the 1×1 penalty is large. This performance improvement results from the fact that the inter-symbol interference spans fewer bit periods for the 2×2 system. The associated penalty reduction is sufficient to even offset any co-channel interference. However, the 2×2 penalty actually increases for the "good" links where the 1×1 penalty is small. In this case, the ISI, if present, already spans very few bits. Therefore, the advantage of reduced data rate per bit stream is not useful anymore. At the same time, the co-channel interference proves more detrimental, thereby causing a net increase in penalty.

6.3.4 Practical Implementation of Joint Launch and MIMO Processing

We have assessed joint launch performance of various systems by optimally choosing between center and offset launch. Such a process requires access to either power penalties or bit error rates. Practical implementation of joint launch is more likely to involve a less than optimal procedure. For example, the technician can first try center launch. If some performance metric such as penalty or BER is within allowed thresholds, then center launch is the preferred launch for that link. If the desired criterion is not satisfied, then the technician switches to offset launch. If the performance criterion is still not met, then the technician as the option of selecting the launch with the smaller penalty, if it is accessible. We refer to such a launch as "JL with CL first". A similar practical joint launch, denoted by

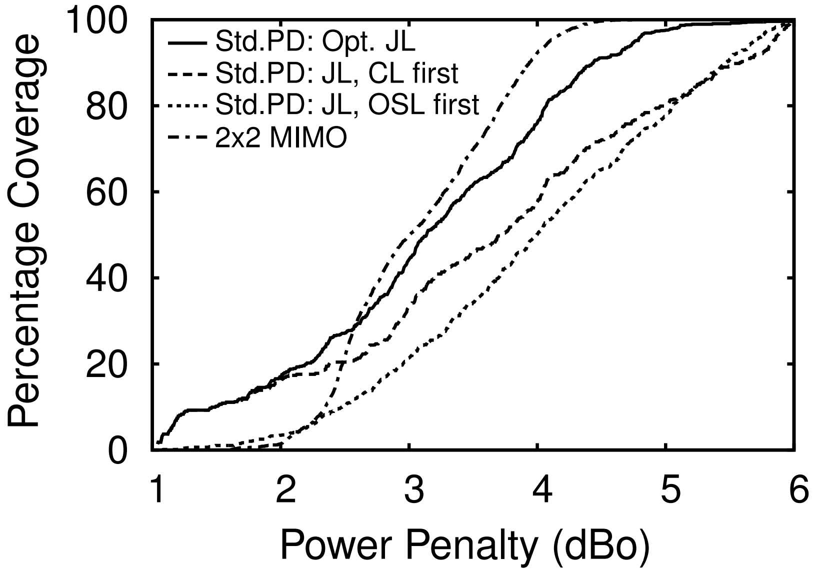

Figure 6.9: Performance for different implementations of joint launch with single-segment photodetector.

"JL with OSL first", begins with offset launch first and then optionally switches to center launch depending on the offset launch penalty. Figure 6.9 shows the coverage curves for these three types of joint launch for the standard single-segment photodetector link. The penalty at the 80% coverage point for both sub-optimal joint launches is 5 dBo. Clearly, the implementation of joint launch can have a severe impact on the performance. While the coverage curves for these two sub-optimal methods intersect near the 80% point, the OSL first method has a larger penalty compared to the CL first method for almost 80% of the links. Therefore, based on the 108-fiber set, trying center launch first seems to be statistically favored.

If we compare these sub-optimal joint launches to the 2×2 MIMO system, the penalty improvement is about 1.35 dBo for the MIMO link. Note that the MIMO system uses both center and offset launch and yet does not require the technician to optimize the launch. Furthermore, no quantitative feedback is required by the MIMO system.

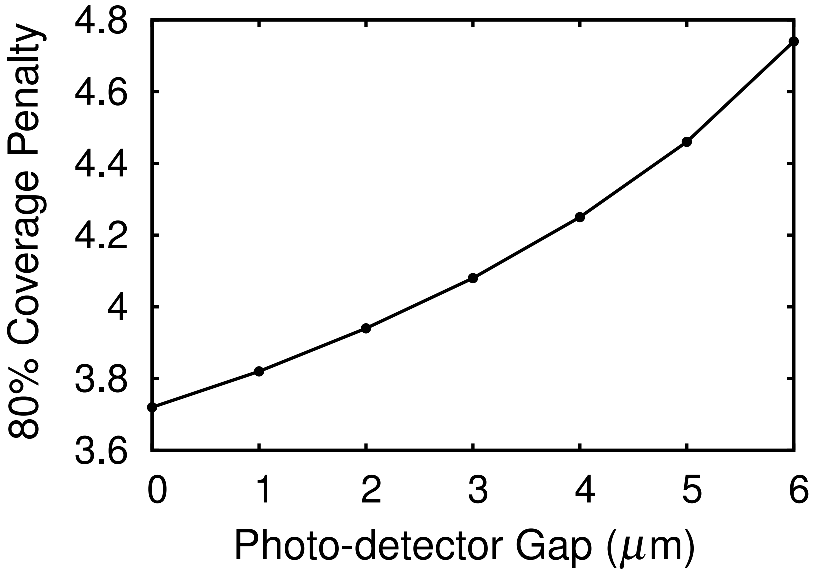

Figure 6.10: Performance for different implementations of joint launch with single-segment photodetector.

6.3.5 Impact of Gap between Photo-detector Segments

The performance results discussed so far were based on a two segment photodetector with no gap between the segments. Introducing a gap between these segments may result in less co-channel interference, thereby reducing the dispersion penalty. However, such a gap results in loss of optical power. Therefore, it is possible that there may not be any net benefit in introducing a gap. We investigate the performance of the 2×2 MIMO system by keeping the inner detector radius fixed at 10μm and increasing the inner radius of the outer segment in steps of 1μm from 0μm to 6μm. In each case, we determine the coverage curve and then the penalty at the 80% coverage point. Figure 6.10 shows this penalty as the gap is increased. Note that this is the net penalty, including the dispersion penalty and the loss associated with the gap. Clearly, the net penalty increases steadily as the gap is increased. The penalty can degrade by as much as 1 dBo when the gap is 6μm.

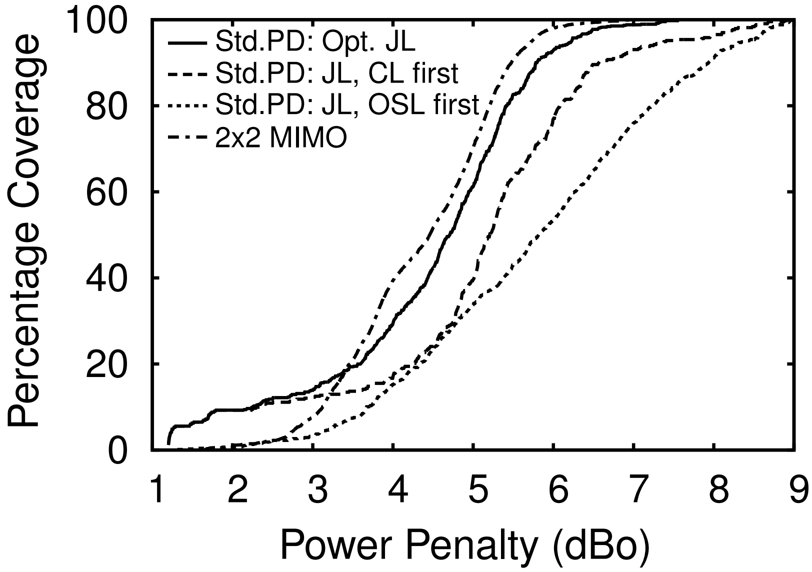

Figure 6.11: Performance for different implementations of joint launch with single-segment photodetector at 20 Gbps.

6.3.6 Can we increase the data rate 20 Gbps?

In this section, we increase the data rate to 20 Gbps and investigate the performance of the 2×2 MIMO system, Fig. 6.11. The penalty at the 80% coverage point for the MIMO system is 5.2 dBo whereas it is 5.4 dBo for the standard single-segment photodetector with optimum joint launch. Note that at a data rate of 10 Gbps, the additional ISI suffered by the 1×1 link is more detrimental than the additional co-channel interference in the 2×2 system for the "bad" links, Fig. 6.9. This results in a larger performance gap between the two systems in the large penalty regime. In contrast, at a data rate of 20 Gbps, the additional co-channel interference for the MIMO link is significant enough that the performance gap between the two systems is more uniform.

The performance of the 1×1 system degrades to 6.1 dBo with the CL first method of implementing joint launch. If the OSL first technique is used, the penalty increases to 7.2 dBo. Therefore, again the 2×2 MIMO system exhibits a performance improvement of 1 dBo or larger compared the standard 1×1 system with practical joint launch.

6.4 Summary

We have considered a multiple-input, multiple-output formulation of the multimode fiber channel via the simultaneous use of center and offset launch together with a two-segment photodetector. We compared the improvement in capacity bounds for such a MIMO scheme with a conventional 1×1 channel, an SRE with photo-current subtraction and an SRE with combining. We then investigated the impact of equalization for these transmission schemes compared to the 1×1 channel. While the 2×2 MIMO system had only a 0.35 dBo improvement in the 80% coverage point penalty for 220m links at 10 Gbps, it is about 1.35 dBo better than the 1×1 channel with practical joint launch. Furthermore, we observed that the gap between photo-detector segments can result in penalty degradation as large as 1 dBo. When the data rate is increased to 20 Gbps, the MIMO scheme results in a performance improvement of 1 dB compared to the conventional channel with practical joint launch.

CHAPTER VII

MULTI-KM MMF LINKS: MODE COUPLING EFFECTS

Thus far, we have considered multi-mode fiber links that are 220m long. One of the long-term objectives of the MMF community is to extend the reach to 1 km and beyond [38]. In this research, we show that in order to assess the performance of multi-km links the channel model needs to be extended to include mode coupling effects. We investigate the ability of electronic equalization to compensate for modal dispersion in the presence of mode coupling in multimode fibers at 10Gb/s. Using a new time domain experimental method we quantify mode coupling in multimode fiber. These results, together with a comprehensive link model, allow us to determine the impact of mode coupling on the performance of multimode fiber. Equalizer performance on links from 300m to 8km is quantified with and without modal coupling. We show that mode coupling effects are influenced by the specific index profile and increase the equalizer penalty by as much as 1dBo for 1km links and 2.3dBo for 2 km links when using the 108 fiber set at 1310nm.

7.1 Mode Coupling in Multi-mode fibers

Optical fibers are known to exhibit random micro-bending along their length, primarily due to the non-uniformities in the properties of the core/cladding and buffering materials. These small bends induce coupling among the different modes of the fiber. In single mode fiber this results in coupling to radiative modes. In multi-mode fiber, there is also coupling among the guided modes that in turn alters the channel response. Since most launch conditions excite fewer modes than are supported in the fiber, coupling results in energy transfer to additional modes and the link response may be significantly different than its zero mode-coupling counterpart. In general, mode coupling reduces the energy in the initially excited modes, broadens the response of the distinct mode groups, and broadens the entire response by coupling energy to modes that otherwise would have little or no energy. Therefore, channel models that ignore modal coupling, such as those typically used to evaluate EDC, are likely to underestimate the optical penalty after equalization. The strength of the coupling determines the impact on the channel response, for example, fibers with extremely strong mode coupling respond with an average group delay (after reaching an equilibrium mode distribution) and therefore exhibit a slower pulse broadening compared to moderate mode coupling. Therefore, we have developed a new and particularly simple experimental method to quantify the mode coupling strength in multi-mode fibers.

Through simulation, we quantify the additional EDC penalty for links from 300m to 8km using the experimentally measured mode coupling coefficient. We examine center and offset launches [1] and show that some fiber index profiles are more susceptible to significant additional penalty due to coupling and that lengths as short as 300m may be impacted although most fibers of 300m length exhibit small mode coupling EDC penalties. We demonstrate that ignoring mode coupling effects can lead to under estimation of equalizer penalty by as much as 1dBo for 1 km fibers for the Cambridge fiber set. Importantly, we find that mode coupling effects in 8 km length and shorter modern MMF have a small impact on the channel 3dB frequency and the DMD temporal span, yet may have a strong impact on equalizer performance. We begin with a description of our numerical modeling of mode coupling effects in MMF links.

7.2 Mode Coupling and its Numerical Modeling

We use the coupled power equations [88] to study the power P_j in the j^{th} mode at time t and axial distance z [88] :

$$\frac{\partial P_j}{\partial z} + \tau_j \frac{\partial P_j}{\partial t} = -\gamma_j P_j + \sum_k d_{j,k} \left(P_k - P_j \right) \tag{7.1}$$

where γ_j is the power loss per unit length, τ_j is the modal delay per unit length and $d_{j,k}$ is the coupling coefficient between mode j and mode k. In using the coupled power equations instead of the coupled electric field equations, we have indirectly assumed that the field amplitude at a particular axial location is uncorrelated with the physical displacement of the fiber axis due to micro-bending at a sufficiently distant location [88]. This is not to say that phase effects have been ignored, indeed, the derivation of equation (7.1) requires a phase matching condition to be satisfied among the interacting modes which results in coupling only between modes where the azimuthal mode numbers differ by unity. We reduce the formulation of the coupling coefficient $d_{j,k}$, between modes j and k given in [89], to a simpler form in terms of the radial component of the electric field:

$$d_{j,k} = A \cdot \left[\frac{(\pi k_0 c \varepsilon_0)^2}{8} \cdot \rho_{j,k}^2 \cdot \frac{1}{(\Delta\beta_{j,k})^8} \right] \tag{7.2}$$

$$\rho_{j,k} = \int_0^\infty r E_j(r) E_k(r) \frac{\partial n^2}{\partial r} dr \tag{7.3}$$

where $E_j(r)$ is the radial component of the normalized electric field for mode j; $\Delta\beta_{j,k}$ is the difference in the propagation constants of modes j and k; $n(r)$ is the refractive index profile and A is the mode coupling strength[1].

The propagation constants and the radial component of the electric fields are obtained numerically via the Georgia Tech mode solver developed as part of this research. The formulation of the mode coupling coefficients by equation (7.2) assumes the normalization of the electric fields [89]:

$$\int_0^\infty r E_j^2(r) dr = \frac{k_0}{\pi} \sqrt{\frac{\mu_0}{\varepsilon_0}} \cdot \frac{1}{\beta_j} \tag{7.4}$$

Since the different modes within a mode group travel with approximately the same propagation constant and (7.2) suggests strong coupling among modes with small $\Delta\beta_{j,k}$, we assume complete coupling within each mode group. Mode groups that differ by one mode group number have the smallest $\Delta\beta_{j,j}$ for pure alpha profiles. Furthermore, we show later that this holds for typical index profile variations. We therefore assume that mode coupling occurs only between adjacent mode groups [89]. Thus, the average coupling coefficient between mode groups g and $g+1$, denoted by d_g, is determined by the power

---

[1] Although $\Delta\beta^4$ and $\Delta\beta^6$ have been suggested in place of $\Delta\beta^8$ in equation (7.2), $\Delta\beta^8$ is supported by the disussion in [90].

coupling equations for the mode groups are given by :

$$\frac{\partial P_g}{\partial z} + \tau_g \frac{\partial P_g}{\partial t} = \begin{cases} -\gamma_g P_g + d_g \left(P_{g+1} - P_g\right) + \left(\frac{g-1}{g}\right) d_{g-1} \left(P_{g-1} - P_g\right) & \text{for } g \text{ even} \\ -\gamma_g P_g + \left(\frac{g}{g+1}\right) d_g \left(P_{g+1} - P_g\right) + \left(\frac{g-1}{g+1}\right) d_{g-1} \left(P_{g-1} - P_g\right) & \text{for } g \text{ odd} \end{cases} \tag{7.5}$$

where P_g denotes the average power in mode group g. The fractions $(g-1)/g$, $(g-1)/(g+1)$ and $g/(g+1)$ confirm the intuition that a given mode group couples with slightly fewer individual modes from the adjacent lower mode group $(g-1)$ when compared to the modes from the next higher mode group $(g+1)$. Equation (7.5) is numerically solved via a split-step method [91, 92] where within each axial step Δz, the mode propagation and mode coupling steps are alternated. Using the mode coupling strength found experimentally, and described later, a step size of 25m provides accurate results while reducing the computational burden.

In the coupling-free case, we model mode dependent attenuation by retaining only the lower 18 mode groups for a 62.5μm core multi-mode fiber at 1310nm. When mode coupling is present, the extreme higher order mode groups couple power to the lossy modes and eventually this power is radiated out. We approximate this scenario by coupling power between the lower 19 mode groups along the fiber length and then eventually discarding the 19$^{\text{th}}$ mode group while computing the received waveform.

7.3 Propagation Constants and Coupling Coefficients

The variation in modal delays and mode power distribution with mode group number was illustrated earlier in sections 2.3 and 2.5 for four of the 108 fibers in the model. Specifically, we had chosen the pure alpha profile fiber, a fiber with a center dip, a fiber with a center peak and finally a fiber with a kink its refractive index profile. The base α for all four fibers is $\alpha = 1.97$. For center launch, the fiber with a center dip has less power in the fundamental mode compared to the other fibers, Fig. 2.5. This results in a higher equalization penalty for this fiber even without mode coupling. For offset launch, all the different fibers have

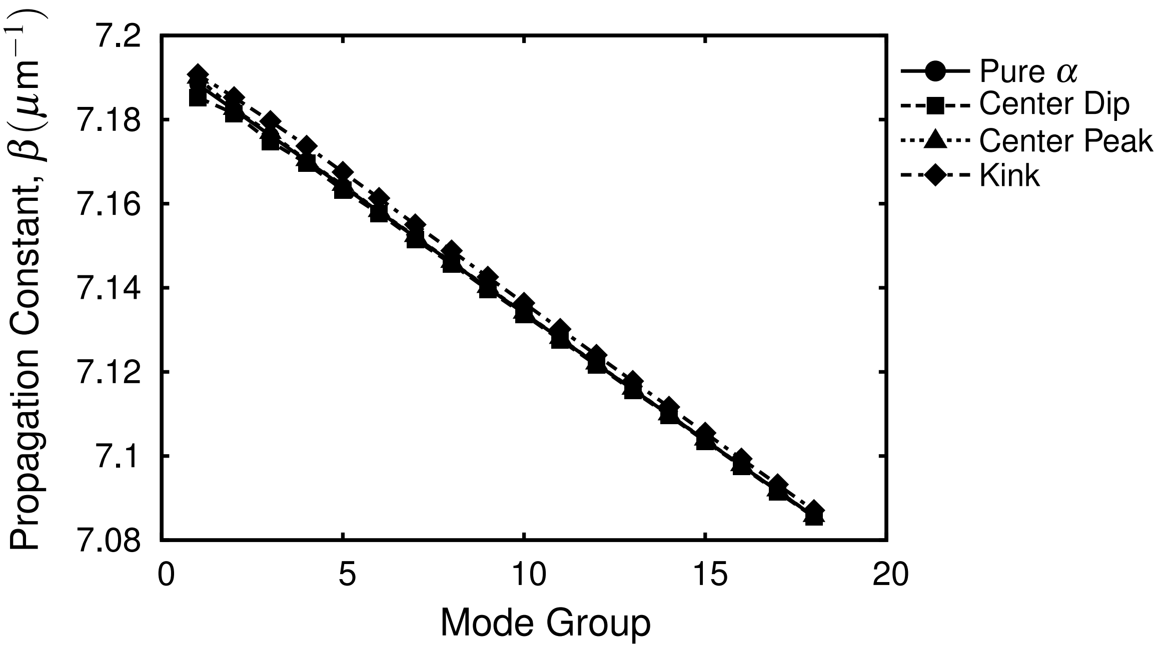

Figure 7.1: Propagation constants for four illustrative fibers. In general, the propagation constant decreases linearly with mode group number.

almost identical mode power distributions, Fig. 2.6. In this case, the significantly larger delay spreads for the fibers with index irregularities, Fig. 2.3, result in higher equalization penalties. In addition, the non-monotonic modal delays of the fiber with a center dip reorder the power distribution generally causing an increased net broadening of the received impulse response. For these illustrative fibers, the propagation constant, β, decreases linearly with mode group number, Fig. 7.1, thereby justifying the use of adjacent mode group coupling in the numerical model.

As we have seen earlier, center launch predominantly excites the lower order mode groups whereas offset launch excites a comparatively larger number of primarily higher order mode groups, Figs. 2.5 2.6. Thus, it may be expected that CL will exhibit more dramatic mode coupling effects since any power transfer from the initially excited LOMs to the adjacent mode groups substantially broadens the received pulse. However, there is significant variation of the mode coupling coefficients with mode group number, Fig. 7.2. The fact that coupling coefficients increase almost linearly with mode group number for

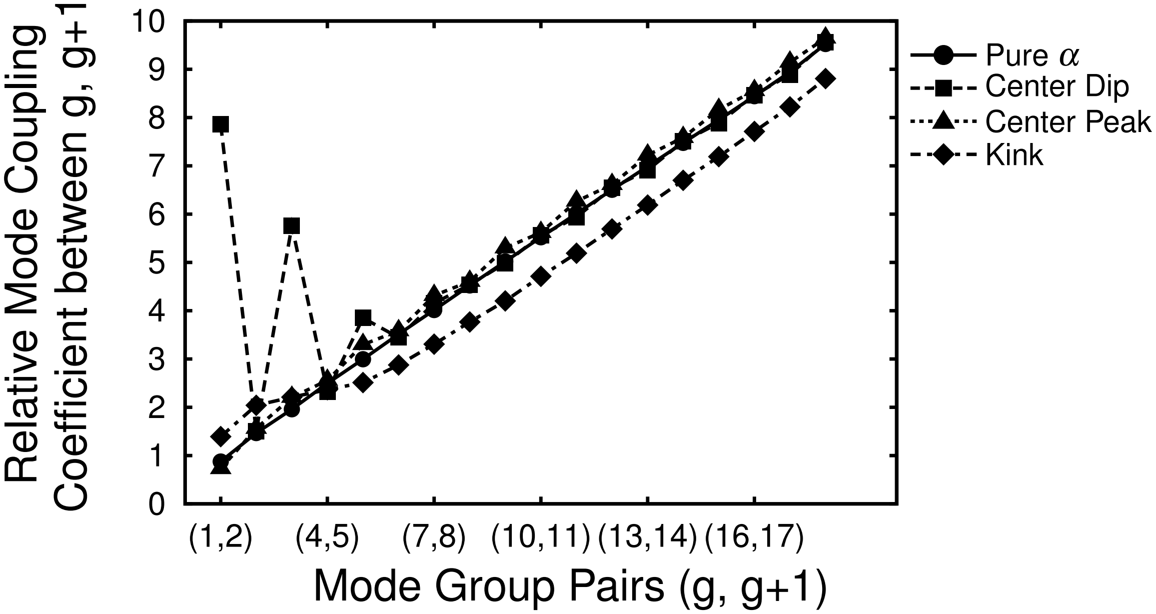

Figure 7.2: Variation of the relative mode coupling coefficients with different refractive index perturbations. In general, the coupling coefficient for these pairs of mode groups increases linearly with mode group number.

most of the fibers [89], indicates that the rate of power exchange between the LOMs is considerably slower than that between the HOMs. This suggests that the mode coupling effects for center launch may not be as dramatic as expected.

7.4 Mode Coupling Strength: Impact on Link Response

In the presence of mode coupling, the fiber impulse response strongly depends on the coupling strength, A. We use the pure alpha profile fiber with center launch to illustrate the received waveform for various coupling strengths for an 8km fiber, Fig. 7.3. The launched pulse shape corresponds to a 10Gbps pulse with 47.1ps rise-time (20%-80%).

In the extremely weak coupling regime, for example for $A \leq 10^4$, the simulated responses matches the coupling-free result. On the other hand, when extremely strong mode coupling is present, for example at $A = 10^{12}$, the received pulse becomes Gaussian and propagates with an average group velocity. This observation agrees well with the dominant eigenvalue framework of [88] where eventually only one eigenmode propagates with the

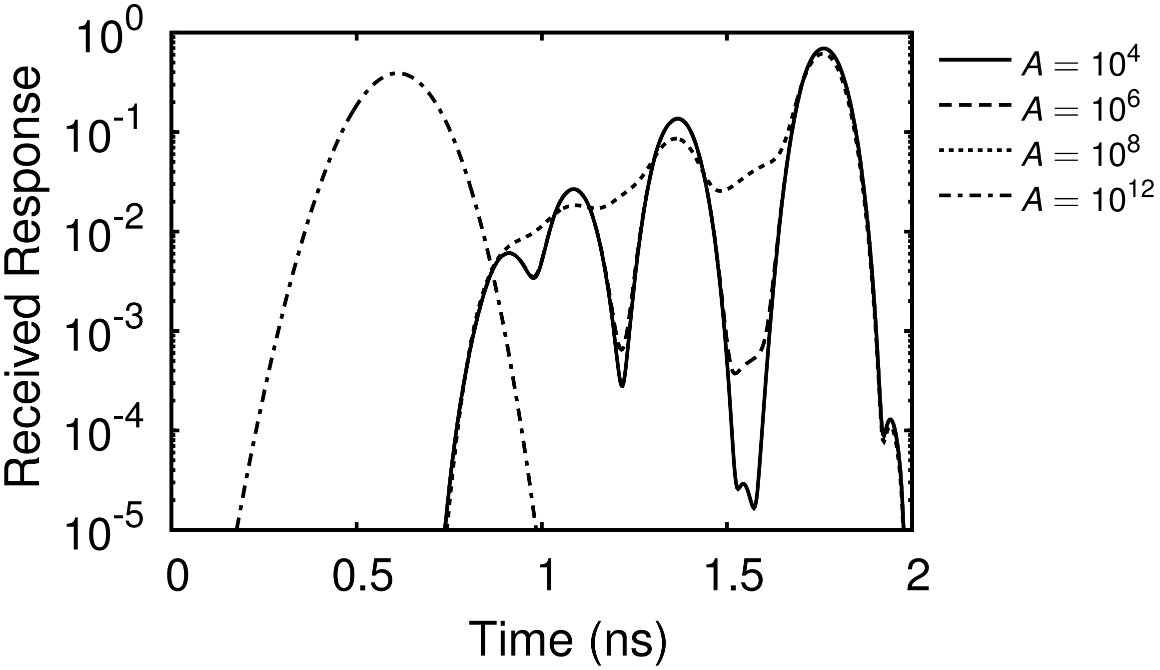

Figure 7.3: Impact of mode coupling on the received pulse for an 8km fiber. The responses correspond to the pure alpha index profile.

average group velocity when the coupling is strong or the fiber is sufficiently long. This agreement between our simulation results and the expected analytical results for these two limiting cases of coupling serves to validate our mode coupling simulation methodology. We note that the position of the Gaussian pulse of Fig. 7.3 results from the presence of faster modes with negligible initial power.

At intermediate coupling strengths, mode coupling causes sufficient energy exchange between the modes resulting in energy arrival at times other than that of the distinct mode groups and the“valleys” are gradually filled in. The relative power in the valleys between the amplitude peaks is a strong function of the coupling strength. While the pulse width is known to increase as $\sqrt{\text{fiber length}}$ in the extremely severe coupling regime, it still increases linearly with fiber length at intermediate and lower coupling strengths, which is the case for the fibers measured. Thus, the temporal span of the DMD and the channel 3 dB frequency, which are typically used to characterize MMF, are not appreciably impacted by modal coupling for intermediate coupling strengths. Therefore, fiber models which are "calibrated" by adjusting the DMD span or 3 dB performance to match that of measured fibers but do not include mode coupling underestimate the EDC penalty for longer links. In the next section, we demonstrate how to exploit these observations to experimentally determine the coupling strength of typical multimode fibers.

7.5 Experimental Evaluation of Mode Coupling Strength

Given the sensitivity of the received waveform to the coupling strength, it is important to quantify modal coupling in multimode fiber. Techniques based on the steady state mode power distribution at the input and output of the fiber [93], evolution of the static mode power distribution with increasing fiber length [94] and analysis of the temporal moment of modal response [95] have been used previously to evaluate mode coupling efficiency. These efforts were in the context of fibers and wavelengths supporting a larger number of mode groups. Therefore, an approximation of mode continuum was made and far field analysis methods were used to spatially resolve the modes. In contrast, our method directly uses the coupled power theory of the discrete mode groups [88]. The proposed method is fundamentally different in that it temporally resolves the mode groups and thereby determines the impulse response of the fiber. Thus, we directly measure the mode coupling effect that impacts the data transmission the most, namely the impulse response and, in particular, the power filling between the mode groups.

We perform a high temporal resolution modal delay measurement with sufficient dynamic range to quantify the energy arriving at times other than that of the primary mode groups. Examination of the modal delay and the amount of "valley filling" observed for the fibers examined reveals that $\approx$ 10ps resolution and 3 orders of dynamic range is sufficient to experimentally determine mode coupling in km length fibers. Chromatic dispersion is avoided by use of transform-limited 16ps FWHM pulses at 1550nm that are launched at different offsets via a single mode fiber. The response is measured with a photodetector/oscilloscope with 20GHz bandwidth[2]. We are careful to ensure that all MMF modes are collected and detected by a sufficiently small detector. However, considering the larger numerical aperture of the HOMs, the numerical aperture of the detector GRIN lens and the detector diameter we find that the HOMs are detected with somewhat lower efficiency than the LOMs and consequently the lower order mode groups are weighted higher when comparing with the numerically generated responses.

Experimentally, the use of 1550nm helps to insure that a number of the primary modes are sufficiently temporally separated due to the larger differential modal delay at 1550nm for fiber optimized for 850nm and 1300nm operation, thereby permitting clear identification of the mode groups from the measured response. The coupling strength, A, is relatively independent of the wavelength since it mainly depends on the spacing of the micro-bending perturbation and mechanical properties such as Young's modulus of the fiber material [90]. Thus, these results are applicable across a wide wavelength range including 1300nm.

To best fit the numerical result to that measured, the individual mode groups and the associated modal delays and mode power distributions are estimated from the experimentally measured response. Together with the measured response of the photodetector/oscilloscope, we then determine the expected received waveform assuming different coupling strengths, A. The coupling strength is varied to best fit the energy in the valleys of the measured response. We note that in practice this estimation process achieves a unique optimum combination of modal delays, mode power distribution and coupling strength.

Figure 7.4 shows the experimental response together with the numerical estimates of the response for two multimode fibers. These measurements were performed by A. Polley. For fiber (a), Fig. 7.4a, the best fit is found with a coupling strength of $7 \times 10^7 \mathrm{m}^{-9}$ whereas for fiber (b), Fig. 7.4b, a coupling strength of $2 \times 10^7 \mathrm{m}^{-9}$ provides a better match with the measured response. We note that these fibers were manufactured in 2000 and 2001 by

---

[2] Tekronix TDS8200 sampling oscilloscope with sampling module 80E03.

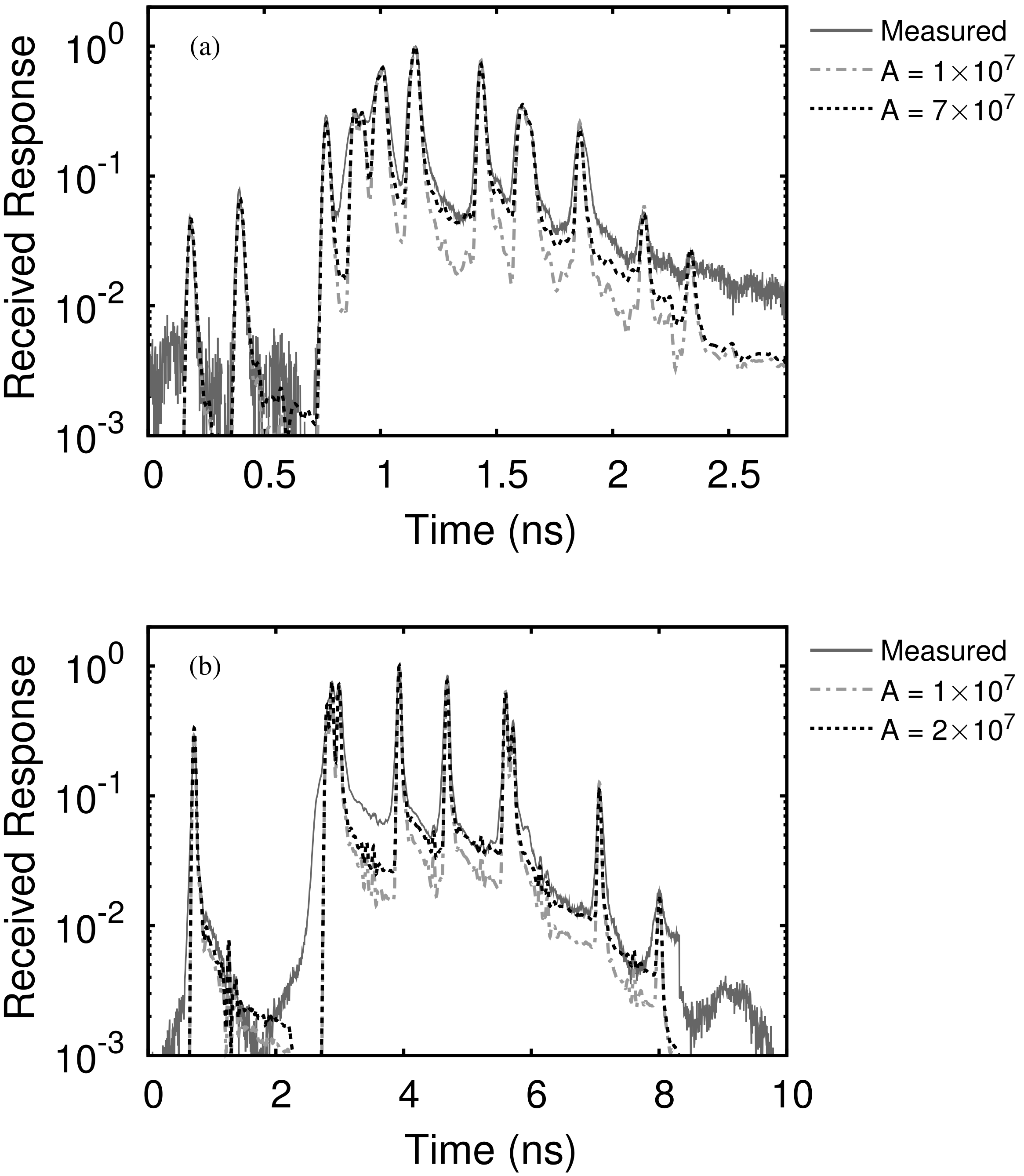

Figure 7.4: Mode coupling strength estimation via high resolution, high dynamic range measurement of MMF responses: (a) 1.1 km fiber (b) 9 km fiber. Mode coupling is identified by the strength of the response between the arrival of the primary mode groups.

different vendors that use different technologies for fabricating the fiber preform. Other fibers that we have measured, exhibit similar coupling strengths. We thus estimate that the coupling strength in typical multimode fibers of recent vintage is $A = 5 \times 10^7 \mathrm{m}^{-9}$ although variation is expected. We note that these are uncabled fibers and that installed cabled fibers may exhibit larger modal coupling. The equalizer penalty computations are carried out using 5×10^7 and, in order to evaluate the sensitivity of the penalty to coupling strength, we also consider a coupling strength of $A = 10^8 \mathrm{m}^{-9}$. The physical interpretation of $A = 5 \times 10^7 \mathrm{m}^{-9}$ can be determined by evaluating the corresponding coupling coefficient d_g, averaged across the mode group pairs, which for the pure alpha fiber is $0.15 \mathrm{km}^{-1}$. Thus, 15% of the power is transferred from one mode group in 1 km.

We note that there are few reports of mode coupling coefficients in the literature and most apply to pre-1985 fibers. For example, the mode coupling coefficient of step-index MMF extracted from the measurement reported in 1978 [95] is $4.8 \mathrm{m}^{-1}$, which is orders of magnitude larger than reported here. However, our results compare well with the coupling coefficients of $0.7 \mathrm{km}^{-1}$ reported in 1993 [96]. The general decrease in coupling coefficients with time suggests an improved manufacturing capability.

7.6 Impact of Mode Coupling on PIE-D: Illustrative Fibers

In this section we will quantify the impact of coupling effects on the power penalty of equalized links of various lengths. Although we have considered various kinds of equalizers in earlier chapters, we will employ the infinite-length DFE for this purpose. Furthermore, we will not consider the effect of connectors in this investigation. We illustrate the variations in PIE-D with reach by examination of the pure alpha fiber and the fiber with a center dip, both for center and offset launches, Fig. 7.5. We note that for both launches, the 300m link performance is not affected significantly by the presence of mode coupling effects for these two fiber profiles.

If mode coupling effects are ignored, then the DFE penalty for the pure alpha fiber

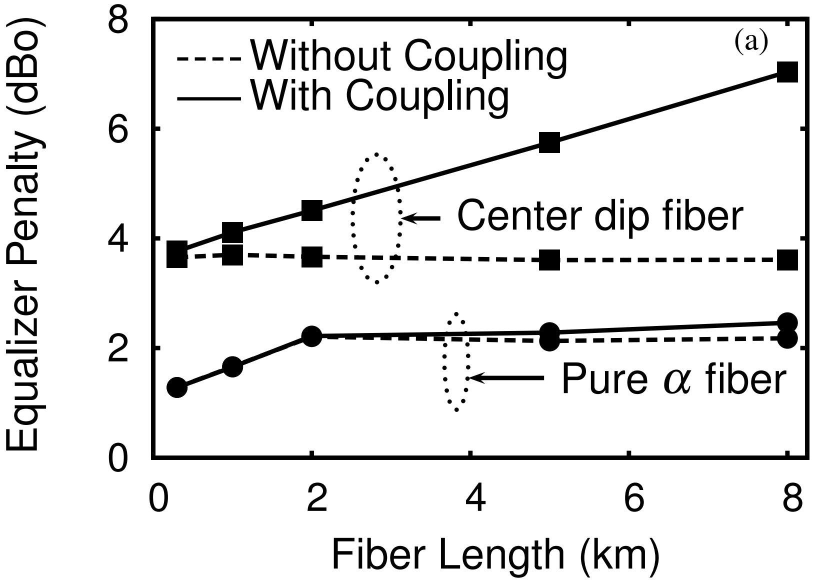

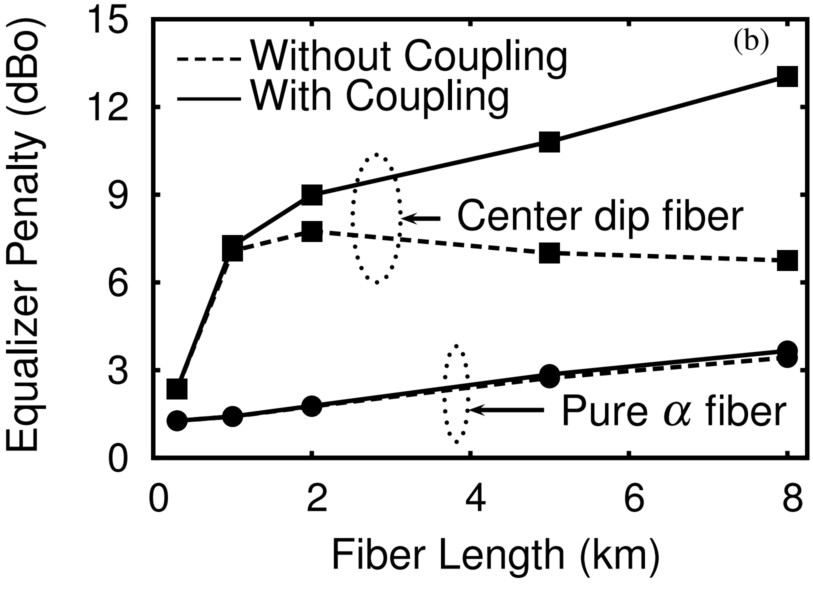

Figure 7.5: Impact of mode coupling on the optimum DFE penalty as the fiber length is increased for $A = 5 \times 10^7$: (a) Center launch (0μm) (b) Offset launch (20μm). For each launch condition, the pure alpha fiber and the fiber with the center dip are shown.

with center launch gradually increases over the first 2km from 1.28dBo to 2.2dBo and then remains almost independent of fiber length, Fig. 7.5a. The distinct mode groups are always sufficiently narrow to arrive within one bit period since chromatic dispersion is negligible. Therefore, once the primary mode group is separated from the other mode groups by one bit slot, the equalization penalty will not increase further. The fiber with a center dip has modal dispersion such that the modes are already mostly separated by 300m in the coupling free case. The penalty reached after the modes have spread out of one time slot, 3.6dBo, is larger compared to the pure alpha fiber penalty, 2.2dBo, due to the lower power in the dominant mode group. In the presence of coupling, the energy fills in between the different mode groups further removing energy from the dominant mode group and thereby resulting in an increasing penalty with increasing fiber length. Beyond 2km, the center dip fiber penalty increases almost linearly at a rate of ≈0.42dBo/km whereas the pure alpha fiber penalty suffers a more modest increase of ≈0.04dBo/km. This results from the larger mode coupling strength of the lower order modes for the center dip fiber compared to the pure alpha fiber.

With offset launch, Fig. 7.5b, the pure alpha fiber has closely spaced modes with a low DMD hence the penalty continues to increase almost linearly with fiber length both with and without coupling. In the absence of mode coupling, the penalty increases from 1.27dBo at 300m to 3.4dBo at 8km whereas coupling results in an additional 0.2dBo penalty at 8km. On the other hand, the fiber with the center dip has non-monotonic modal delays Fig. 2.3. For this fiber complete temporal separation of the modes beyond one bit slot actually reduces the EDC penalty. In the presence of mode coupling, power leaks away from the main part of the signal thereby increasing the penalty significantly. For this fiber, mode coupling can cause increases in the equalizer penalties by as much as 1.24dBo at 2km to 6.3dBo at 8km.

The analysis of mode coupling effects shows that with sufficiently strong mode coupling and sufficient length of fiber, a steady state response independent of the initial mode

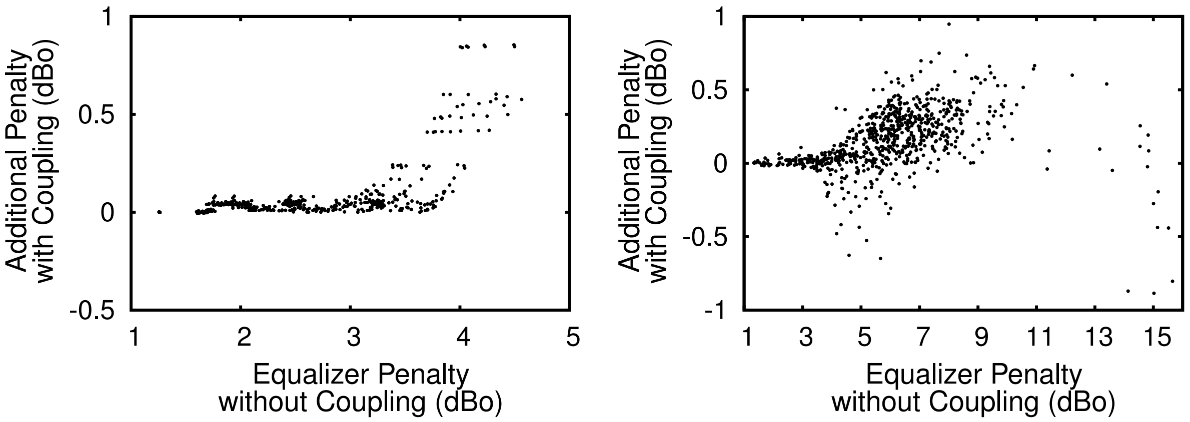

(a) $A = 5 \times 10^7$, Center Launch

(b) $A = 5 \times 10^7$, Offset Launch

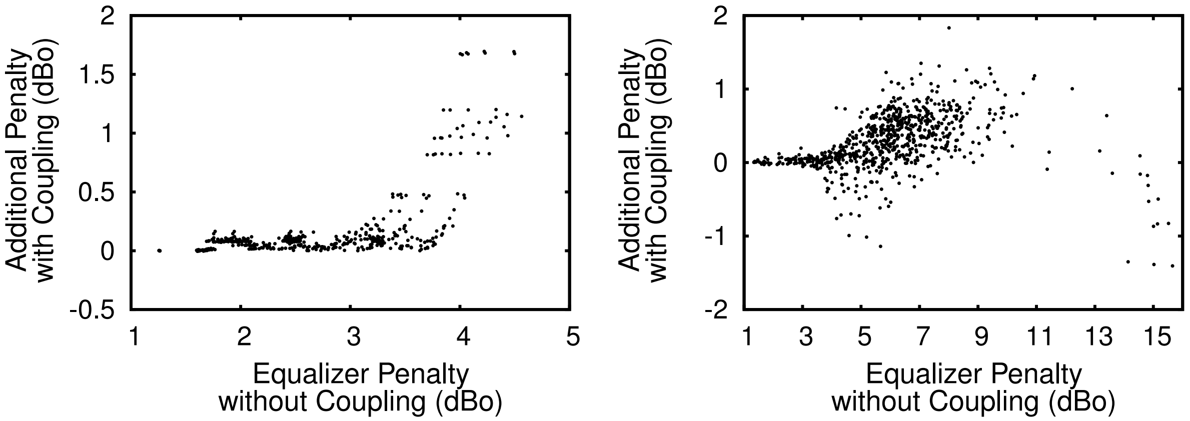

(c) $A = 10^8$, Center Launch

(d) $A = 10^8$, Offset Launch

Figure 7.6: Additional equalizer penalty due to mode coupling for a 1km link for the entire 108 fiber set: (a) $A = 5 \times 10^7$ with center (b) $A = 5 \times 10^7$ with offset launch (c) $A = 10^8$ with center (b) $A = 10^8$ with offset launch.

power distribution will be achieved [88, 89]. This equilibrium pulse shape is not attained in typical silica multimode fibers for the link lengths considered due to the weak-to-moderate mode coupling strength. We also note that the rate at which this equilibrium shape is approached depends on the initially excited mode groups. Therefore, center and offset launch are expected to achieve the steady-state pulse shape at different fiber lengths.

7.7 Statistical Variation of EDC Penalties

Although the foregoing analysis reveals some useful intuition for specific fiber profiles, the goal of EDC is to extend the reach of a large percentage of the installed fibers. We use the complete 108 fiber set to analyze the impact of mode coupling on the DFE penalties. We now define center launch to encompass the launch offsets 0-3μm and offset launch to include 17-23μm. Figure 7.6 shows the additional EDC penalty due to mode coupling compared to the coupling-free penalty on a link-by-link basis for a 1km fiber for two different coupling strengths $A = 5 \times 10^7, 10^8$. With center launch, Figs. 7.6a, 7.6c, the equalizer penalty increases for all the fibers with mode coupling compared to the coupling-free case. Furthermore, the higher the coupling-free EDC penalty, the more adverse is the effect of mode coupling on the penalty. With offset launch, Figs. 7.6b, 7.6d, essentially all of the 108 fibers show an increase in the DFE penalty. But for a few fibers the penalty decreases with mode coupling. The equalizer penalty decreases by modest amounts with increasing fiber length via one of two mechanisms:

1. The ISI for the longer fiber occupies time intervals other than the sampling instant whereas it coincides with the sampling instant for the shorter fiber.

2. The ISI at the sampling instant is smaller while the main peak amplitude remains the same, possibly due to coupling to radiative modes.

While the first mechanism is applicable even to the coupling-free case, mode coupling can produce both scenarios. For example, the penalty reduces due to coupling when the mode groups with larger mode coupling coefficients have either extremely large or small modal delays and at the same time most of the power is in the mode groups with smaller coupling coefficients. At larger fiber lengths, even the main peak of the response loses power through coupling and so the EDC penalty increases. Comparison of the equalizer penalty on a fiber-by-fiber basis with and without mode coupling indicates that PIE-D can be under-estimated by as much as 0.25dBo for 300m links, 1dBo for 1km links and 2.3dBo for 2km links for

$A = 5 \times 10^7$.

Increasing the coupling strength to $A = 10^8$ from $A = 5 \times 10^7$ for 1km links results in an additional penalty of 0.25dBo or greater in 8% of the links for center launch. For offset launch, a coupling strength of $A = 10^8$ causes the penalty to increase by 0.5dBo or greater in 26% of the links compared to the $A = 5 \times 10^7$ case. In fact, the worst-case increase is 0.84dBo for center launch and 0.9dBo for offset launch. Thus, even a small increase in the coupling strength can notably increase the equalizer penalty.

For each fiber length, we also determine the cumulative distribution of the EDC penalty without and with mode coupling. Figure 7.7 shows the corresponding coverage curves, which are the percentage of fibers that can be equalized while incurring a penalty less than that given by the abscissa. For clarity, we show only the 300m, 1km and 5km data. In the coupling-free case with center launch, Fig. 7.7a, the equalizer penalty increases systematically with increasing fiber length. For the worst-case fibers, typically the center dip fibers, the coverage curves overlap, Fig. 7.7a (inset), indicating that the coverage remains essentially unchanged with increasing fiber length. In the presence of coupling, the 300m coverage is almost unchanged compared to the no coupling case. For longer fibers, the presence of coupling systematically increases the penalty with a more severe increase at higher coverages. Again, these higher penalty links, often center dip profiles, exhibit the larger coupling penalty due to power being coupled away from the dominant peak, Fig. 7.5a.

With offset launch, Fig. 7.7b, there is significant power launched into a larger number of modes compared to center launch. In the absence of mode coupling, the equalizer penalty increases significantly due to increasing effects of DMD with increasing fiber length. Interestingly, the higher percentage coverage of the 5km link is better than that of the 1km link. The longer fiber is better in this case since the individual mode groups are sufficiently separate so as to be distinct on the time scale of a bit slot. On the other hand, mode coupling causes significant power to be coupled away from the dominant peak, resulting in a large increase in penalty so that the penalty always increases with fiber length.

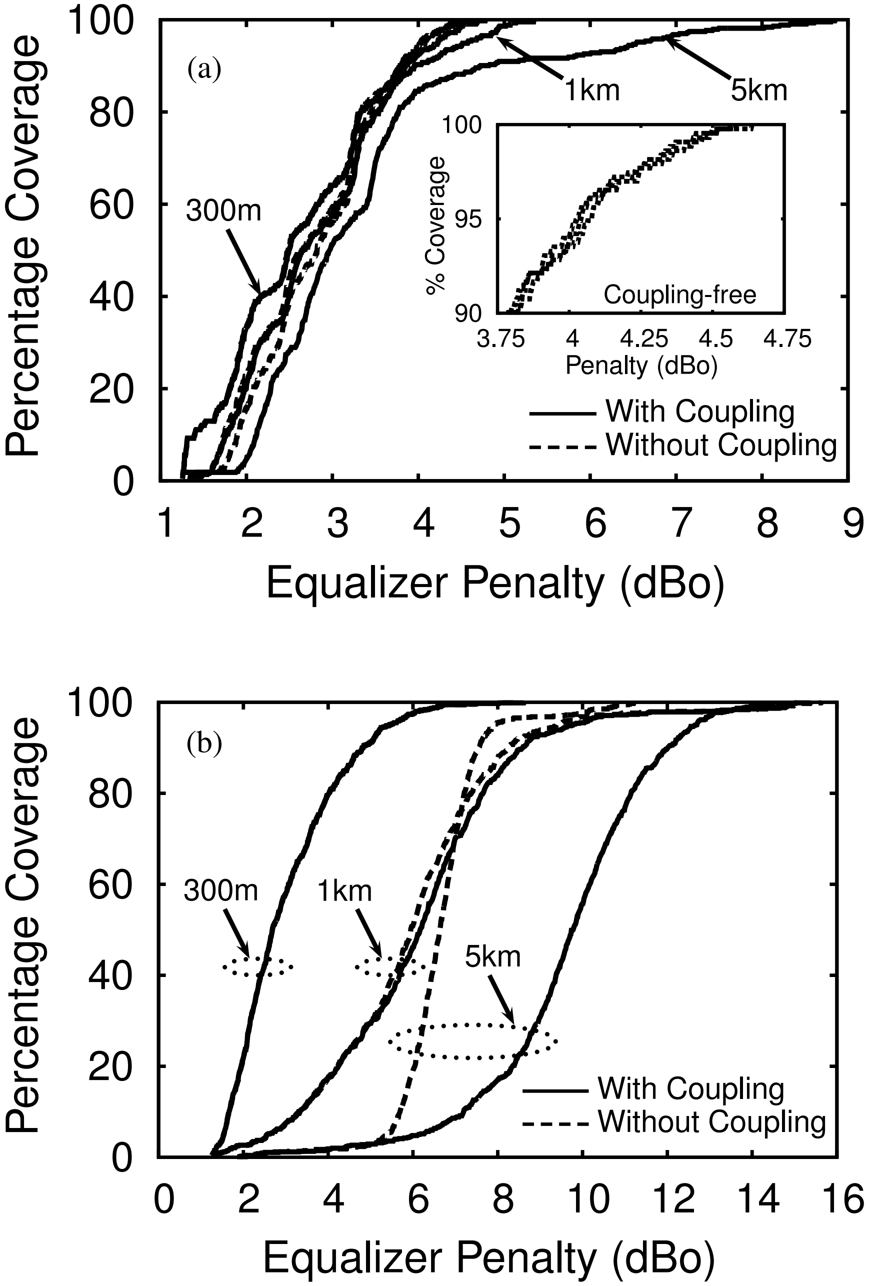

Figure 7.7: Statistical impact of mode coupling on equalizer penalty at 10Gbps with $A = 5 \times 10^7$. (a) Center Launch (b) Offset launch. Dashed lines represent the coupling-free case whereas solid lines denote results with coupling.

It is noted that center launch suffers a smaller deterioration of the equalizer penalty when coupling is included compared to offset launch. This characteristic is mainly attributable to the mode coupling coefficient for the HOMs being significantly larger than those for the LOMs.

7.8 Worst-Case DFE Penalties

In section 2.10, we have discussed how the worst-case performance of the 108 fiber set is characterized by the 95% coverage point in the connector-less case and by the 80% coverage point when connectors are present. Although the multimode fiber links discussed in this chapter do not have any connectors, we will still consider the equalizer penalties at both coverage points for the sake of completeness, Fig. 7.8.

With center launch, neglecting mode coupling effects results in an under-estimation of the 95th percentile PIE-D by 0.14dBo for 300m links, 0.5dBo for 1km links and 1dBo for fibers that are 2 km long, Fig. 7.8a. On the other hand, the 80th percentile PIE-D remains virtually unchanged for 300m links but increases by 0.1dBo for 1km links and 0.15dBo for 2km long fibers due to mode coupling.

With offset launch, mode coupling causes an additional increase of 0.4-1.3dBo for the 1-2km fibers at the 95th percentile point, Fig. 7.8b. Even at the 80% coverage point, the penalty increases by 0.3-1.1dBo for fibers that are 1-2km long. The 300m link penalties at the 95th and 80th percentiles are not affected by mode coupling for offset launch.

For the 108 fiber set, joint launch primarily follow center launch and has a penalty degradation in the 0.35-1dBo range for the 1-2km long fibers. At the 80th percentile point, the penalty increases only by 0.1dBo for the 1-2km fibers, consistent with the corresponding center launch performance. At longer lengths, the 95th percentile equalizer penalty can be under-estimated by as much as 2-4 dBo due to mode coupling for joint launch. This penalty degradation reduces to 0.3-0.5 dBo at the 80th percentile point.

While connector effects have not been considered in this work as mentioned earlier, we point out that having two connectors at the transmitter with a worst-case offset of 7μm each results in an additional penalty of 2.5dBo for both center and offset launch at the 80% coverage point for 300m links with the 108 fiber set. Clearly, connector effects are more significant than coupling effects for such short links. Furthermore, the penalty increase due to connectors is not expected to change significantly for longer MMF links so that mode coupling effects are likely to dominate connector effects for fibers longer than a few km.

7.9 Summary

We have experimentally determined the coupling strength for multimode fibers using a novel, high-resolution measurement of the received impulse response. We find that the typical coupling strength due to random micro-bending in MMF fibers is near 5×10^7. Armed with this estimate of the mode coupling strength, we have investigated the applicability of decision feedback equalization to extending the reach of 10Gbps Ethernet links to the multi-km range. We have demonstrated that ignoring mode coupling effects leads to an under estimation of equalizer penalty by as much as 0.25dBo for 300m, 1dBo for 1km fibers and 2.3dBo for fibers that are 2km long. These significant deviations in EDC penalty underscore the necessity of accurate and realistic fiber models in assessing the performance of electronic equalizers.

An assessment of current equalizer technology requires evaluation of the performance of finite-length equalizers. Importantly, the additional penalties due to mode coupling primarily arise from the continuum of energy which appears between the arrivals of the primary mode groups. Since the equalizer penalties reported here correspond to the optimum DFE with infinite number of taps, the net penalties of real equalizers are expected to be worse.

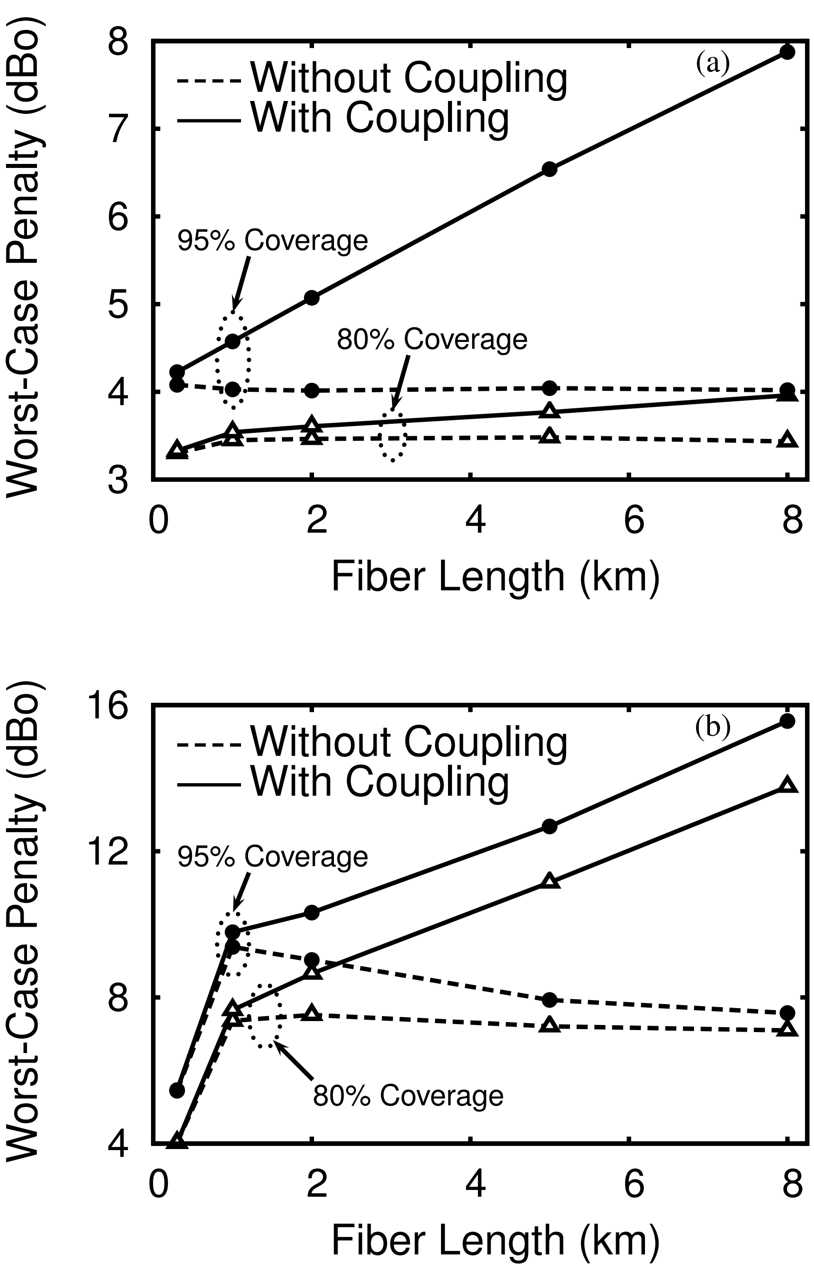

Figure 7.8: Equalizer penalties at the 80% and 95% coverage points for $A = 5 \times 10^7$: (a) Center launch (b) Offset launch. Dashed lines represent the coupling-free case whereas solid lines denote results with coupling.

CHAPTER VIII

CONCLUSIONS

The unifying theme of this thesis is the electronic equalization of multi-mode fiber links with the objective of increasing the data rate and possibly extend the reach. We first summarize the important contributions of this thesis and then point out some future research directions.

8.1 Contributions

The broad methodology of channel modeling, followed by base-lining the performance currently used receivers and then investigation of electronic equalizers was adopted in this research. We have also investigated the performance of some novel equalizers such as the bidirectional DFE and MIMO transmission as applied to the MMF channel. Some of the significant contributions of this research are described below :

- *Fiber Modeling:* A robust mode solver that can handle arbitrary refractive index profiles, launch conditions and wavelengths was developed. It is currently in use by one of the largest fiber manufacturers for their internal R&D work.
- *FFE/DFE Performance and IEEE 802.3aq std.:* A detailed performance assessment of the impact of decision feedback equalizers has been conducted using an extensive model of the installed fiber base. The finite-length DFE results were instrumental in influencing the IEEE 802.3aq standardization effort. In particular, we were able to achieve a reach of 220m but the original goal of 300m was unattainable on 99% of the installed fiber base using DFEs of moderate complexity.

- *Bidirectional DFE:* A low-cost equalizer that has excellent performance, the bidirectional DFE, was applied to the MMF channel for the first time. The performance of the infinite-length BiDFE was characterized without any constraints on the signal-to-noise ratio and on the receiver front-end, as has been previously done in the literature. A new joint optimization technique that helps the finite-length BiDFE perform significantly better than the infinite-length DFE was developed. It was shown that given a finite number of filter coefficients, the BiDFE utilizes them better than the conventional DFE. Furthermore, a reach of 350-400m at a data rate of 10 Gbps was shown to be feasible with equalizers of complexity similar to that currently available.
- *MIMO MMF Links:* A multiple-input, multiple-output (MIMO) characterization of the MMF channel was developed through the simultaneous use of both center and offset launch together with the two-segment photo-detector. The potential benefits of MIMO processing for MMF links was demonstrated by computing Shannon capacity bounds. It was established that the 2×2 MIMO channel performs about 1.4dBo better than the conventional 1×1 link at 10 Gbps with practical joint launch. The MIMO scheme still has a performance improvement of 1dBo at 20 Gbps thereby indicating that 20 Gbps transmission is feasible.
- *Extended Reach MMF Links and Mode Coupling:* Performance evaluation of multi-km MMF links was conducted using a comprehensive model that accounts for mode coupling effects. It was determined that ignoring mode coupling can result in underestimation of the optimum DFE penalty by as much as 1 dBo for 1km links.

8.2 Future Directions

Several exciting possibilities for future investigations have emerged during this research. One interesting problem with both theoretical and practical implications is the joint design of the multi-mode fiber and equalizers. We have investigated the impact of electronic equalizers on the installed fiber base. Can better performance and/or lower complexity be achieved if the fiber design phase is cognizant of the equalizer to be used in the link? Or will optimizing the fiber and the equalizer separately be sufficient? A thorough understanding of this issue will be of immense value to both researchers and practicing engineers.

The capacity analysis of intensity modulated optical channels in Chapter 5 was restricted to the ISI-free case. Determining capacity bounds in the presence of ISI is still an open problem and needs to be explored.

MIMO equalization of MMF links was explored using infinite-length MIMO-DFEs. Performance characterization using finite-length DFEs will be useful in assessing practical extensions of this work.

APPENDIX A

BIT ERROR RATE ESTIMATION FOR LINEAR ISI CHANNELS

At the heart of any communication receiver, is the decision device, where a soft estimate of the transmitted bit is compared with a threshold to determine the transmit bit. This decision device is more commonly known as the *slicer* or thresholder in the literature. Since the output of the decision device is a bit estimate, we will assume that its input is at the baud rate (= data rate). Figure A.1 shows the effective end-to-end channel as seen by the slicer. The transmit bits, a_k, pass through an FIR filter, h_k, representing the effective channel and then get corrupted by noise, n_k, before entering the slicer. Mathematically this is equivalent to :

$$w_k = h_0 a_k + \underbrace{\sum_{i \neq 0} h_i a_{k-i}}_{q_k} + n_k \tag{A.1}$$

where q_k denotes the residual inter-symbol interference seen by the slicer. As is commonly done in the literature we assume that the noise, n_k, is white and Gaussian with zero mean and variance σ_n^2. Although such an assumption is not always valid, the resulting performance numbers are still reasonably accurate. We note that a commonly used methodology is to assume that the residual ISI *and* the noise together are modeled as a white, Gaussian process. Although this approximation results in a very fast computation technique, the accuracy of its results are suspect, particularly when moderate amount of ISI is present.

Let I denote the number of bits spanned by the ISI. Since MMF links use binary signaling, this implies 2^I possible values for q_k. We denote each of these possibilities by $q^{(i)}, i = 1, 2, \ldots, 2^I$. Therefore, the probability of a bit error is given by :

$$P_e = \sum_{i=1}^{2^I} P\left[\text{error} \middle| q_k = q^{(i)}\right] \cdot P\left[q_k = q^{(i)}\right] \tag{A.2}$$

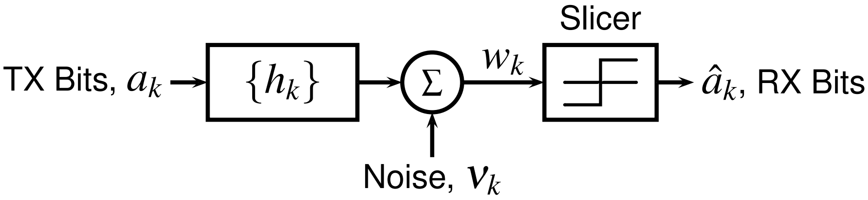

Figure A.1: Effective channel seen by the slicer

where $P[\cdot]$ denotes the probability of the event. The conditional error probability can be easily determined for binary signaling :

$$P\left[\text{error}\middle| q_k = q^{(i)}\right] = Q\left(\frac{h_0 - q^{(i)}}{\sigma_n}\right) \tag{A.3}$$

where $Q(\cdot)$ is the well known Q-function [15]. Therefore, the final bit error rate for the ISI channel in Fig. A.1 is given by :

$$P_e = \sum_{i=1}^{2^I} P\left[q_k = q^{(i)}\right] \cdot Q\left(\frac{h_0 - q^{(i)}}{\sigma_n}\right) \tag{A.4}$$

For independent and identically distributed transmit bits, this expression reduces to :

$$P_e = \frac{1}{2^I} \sum_{i=1}^{2^I} Q\left(\frac{h_0 - q^{(i)}}{\sigma_n}\right) \tag{A.5}$$

When the ISI spans a limited number of bits, the bit error rate is most efficiently computed using (A.5) by determining all possible values of q_k. On other hand when I is large, we resort to characteristic functions to compute the probability mass function which effectively becomes a continuous function.

The characteristic function of q_k, $\Phi_q(f)$, is given by :

$$\Phi_q(f) = E\left[e^{-j2\pi f q_k}\right] = E\left[e^{-j2\pi f \sum_{i\neq 0} h_i a_{k-i}}\right] \tag{A.6}$$

$$= \prod_{i\neq 0} E\left[e^{-j2\pi f h_i a_{k-i}}\right] \qquad \text{from the independence of } a_k\text{'s} \tag{A.7}$$

Since the a_k's are equally likely to be ± 1, we have :

$$E\left[e^{-j2\pi f h_i a_{k-i}}\right] = \cos(2\pi f h_i) \tag{A.8}$$

And therefore the characteristic function is given by :

$$\Phi_q(f) = \prod_{i \neq 0} \cos(2\pi f h_i) \tag{A.9}$$

Note that the probability density function (PDF) of q_k is nothing but the inverse Fourier transform of $\Phi_q(f)$ [15], which can be efficiently computed via FFTs. Once the PDF of q_k is known, the bit error rate is determined by :

$$P_e = \sum_{n=0}^{N-1} P\left[q_k = \hat{q}^{(n)}\right] \cdot Q\left(\frac{h_0 - \hat{q}^{(n)}}{\sigma_n}\right) \tag{A.10}$$

where N is the number of points used in the FFT and $\hat{q}^{(n)}$ are the different values of q_k as approximated by the FFT. Since the ISI spans a large number of bits, the error in this approximation is negligible.

To summarize, we use the direct enumeration method of (A.5) for the limited ISI cases and the Fourier transform method of (A.10) when the ISI spans a large number of bits.

APPENDIX B

OPERATING SNR FOR ISI LINKS

As explained in the main text, the desired bit error rate for the ISI-free link along with an SNR margin determine the SNR at which communication over the ISI link takes place. In this chapter, we summarize the key results for ISI-free links and determine the operational SNR for the ISI channel.

The reference channel without inter-symbol interference is shown in Figure B.1. The transmitter sends bits a_m of variance σ_a^2 at a bit rate of $1/T_r$. The subscript r denotes that the corresponding parameter is specific to the reference channel. The transmit filter, $\phi_r(t)$, is assumed to have energy $\varepsilon_{\phi,r}$. The noise, $\eta(t)$, is assumed to be additive white Gaussian with a power spectral density of $N_0/2$. Clearly, the received sample ρ_k is given by :

$$\rho_k = \sum_m a_m q_{k-m} + n_k \tag{B.1}$$

where $q_k = q(kT_r)$ and $q(t) = \phi_r(t) \bigstar \phi_r^*(-t)$. The corresponding noise sample is $n_k = n(kT_r)$ where $n(t) = \eta(t) \bigstar \phi_r^*(-t)$. Since the reference channel is assumed to be ISI-free, $\phi_r(t)$ has to satisfy :

$$q_k = \varepsilon_{\phi,r} \delta_k \tag{B.2}$$

It follows that :

$$\rho_k = \varepsilon_{\phi,r} a_k + n_k \tag{B.3}$$

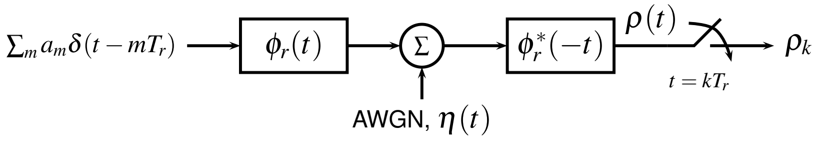

Figure B.1: Reference channel without inter-symbol interference.

where the noise samples n_k are independent and Gaussian with a variance $\varepsilon_{\phi,r} N_0/2$. It is straight-forward to show that the bit error rate for such a link with binary signaling is given by :

$$P_e = Q\left(\sqrt{\frac{\sigma_a^2 \varepsilon_{\phi,r}}{N_0/2}}\right) \tag{B.4}$$

Defining the signal-to-noise ratio as :

$$SNR \triangleq \frac{\sigma_a^2 \varepsilon_{\phi,r}}{N_0/2} \tag{B.5}$$

we get $P_e = Q\left(\sqrt{SNR}\right)$ which is the standard form of the BER expression for ISI-free binary signaling [15].

For multimode fiber links, the desired BER for the ISI-free case is $P_e = 10^{-12}$. Therefore, the corresponding SNR is :

$$SNR_{\textit{ISI-free}} = \left[Q^{-1}(P_e)\right]^2 \approx 17 \text{ dBe} \tag{B.6}$$

Since the power budget for 10 Gbps Ethernet allows for a margin of 6.5 dBo = 13 dBe [16], the SNR at which the actual ISI link is operated is :

$$SNR_{ISI} \triangleq SNR_r = SNR_{\textit{ISI-free},\mathrm{dBe}} + \mathrm{Margin}_{\mathrm{dBe}} \approx 30 \text{ dBe} \tag{B.7}$$

We will now establish the relationship between the average transmit power, P_{av}, and the operating SNR. Note that the average transmit power is given by :

$$P_{av} = \frac{\sigma_a^2 \varepsilon_{\phi,r}}{T_r} \tag{B.8}$$

Expressing σ_a^2 in terms of SNR_r from (B.5), we get :

$$\frac{P_{av}}{N_0/2} = \frac{SNR_r}{T_r} \tag{B.9}$$

For the 10 Gbps Ethernet power budget, this simplifies to :

$$P_{av,\mathrm{dBm}} \approx (N_0/2)_{\mathrm{dBm/Hz}} + 130 \tag{B.10}$$

Note that the ratio on the left-hand side of equation (B.9) is applicable to any transceiver system, not just ones operating at a specific signaling rate and SNR. The reference channel simply provides a way of determining the ratio $P_{av}/(N_0/2)$. In fact, we use this ratio to compute the Shannon capacity of the multimode fiber channel. Furthermore, different communication schemes will be compared at the same P_{av} assuming that the noise power spectral density remains unchanged.

APPENDIX C

FINITE-LENGTH DFE OPTIMIZATION & RESIDUAL ISI

We give a brief overview of the main results in the optimization of the finite-length decision feedback equalizer, which is shown in Fig. C.1. We also describe an efficient and accurate procedure to estimate the performance of the finite-length DFE without processing any bits.

C.1 Minimum Mean Square Error Optimization of the DFE

In this section, we optimize the finite-length DFE coefficients to minimize the mean square error (MSE) between the slicer input, w_k and the corresponding transmit bit, $a_{k-\Delta}$ where Δ is an appropriately chosen delay. Our approach, based on the one outlined in [59], is summarized next.

C.1.1 Equalizer Input

The input to the equalizer, $r(t)$, can be written as :

$$r(t) = \sum_m a_m h(t - mT) + n(t) \tag{C.1}$$

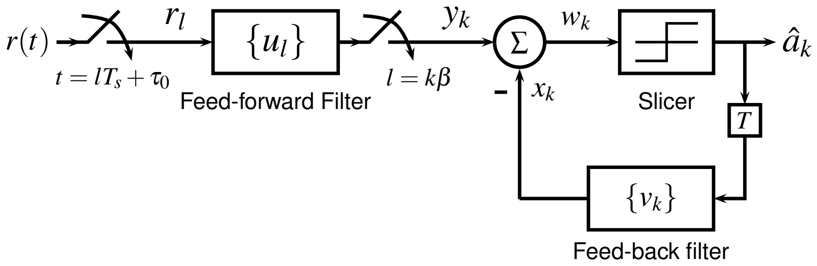

Figure C.1: Structure of the decision feedback equalizer.

where $h(t) = h_{TX}(t) \bigstar h_{MMF}(t) \bigstar h_{RX}(t)$ and $n(t) = \eta(t) \bigstar h_{RX}(t)$, with $\bigstar$ denoting convolution. The output of the $1/T_s$ sampler is then given by:

$$r_l = \sum_m a_m h_{l-m\beta} + n_l \tag{C.2}$$

where $h_l = h(lT_s + \tau_0)$ and $n_l = n(lT_s + \tau_0)$, with $\tau_0 \in [0, T)$ being the sampling instant. Note that β is the over-sampling factor, i.e. the feed-forward filter taps are spaced T/β apart.

Assuming $\eta(t)$ has a power-spectral density of $N_0/2$, the autocorrelation of the noise samples, n_l, can be shown to be :

$$R_{nn,c}(\tau) = \frac{N_0}{2} h_{RX}(\tau) \bigstar h^*_{RX}(-\tau) \tag{C.3}$$

$$R_{nn}(m) = R_{nn,c}(mT_s) \tag{C.4}$$

where $R_{nn,c}(\tau)$ is the autocorrelation of the continuous-time noise, $n(t)$, at a lag of τ.

One bit period of the samples, r_l, can be written as:

$$\underbrace{\begin{bmatrix} r_{k\beta} \\ r_{k\beta-1} \\ \vdots \\ r_{k\beta-(\beta-1)} \end{bmatrix}}_{\mathbf{r}_k} = \begin{bmatrix} \mathbf{h}_0 & \mathbf{h}_1 & \cdots & \mathbf{h}_{L_h} \end{bmatrix} \begin{bmatrix} a_k \\ a_{k-1} \\ \vdots \\ a_{k-L_h} \end{bmatrix} + \underbrace{\begin{bmatrix} n_{k\beta} \\ n_{k\beta-1} \\ \vdots \\ n_{k\beta-(\beta-1)} \end{bmatrix}}_{\mathbf{n}_k} \tag{C.5}$$

where $\mathbf{h}_i$ is defined as follows :

$$\mathbf{h}_i = \begin{bmatrix} h_{i\beta} \\ h_{i\beta-1} \\ \vdots \\ h_{i\beta-(\beta-1)} \end{bmatrix} \qquad i = 0, 1, \ldots, L_h \tag{C.6}$$

We have assumed that the composite channel impulse response, $h(t)$, has a duration of L_h bit periods, i.e. $0 \le t < L_h T$. Therefore, the last $\beta - 1$ elements of $\mathbf{h}_0$ and the first element of $\mathbf{h}_{L_h}$ are zero.

C.1.2 Feed-forward filter

The sampled output of the feed-forward filter, y_k, can then be written as :

$$y_k = \mathbf{u}^T \underbrace{\begin{bmatrix} \mathbf{r}_k \\ \mathbf{r}_{k-1} \\ \vdots \\ \mathbf{r}_{k-(L_F-1)} \end{bmatrix}}_{\mathbf{R}_k} \tag{C.7}$$

where $\mathbf{u}^T$ is the transpose of $\mathbf{u}$, and is defined as :

$$\mathbf{u}^T = \begin{bmatrix} u_{0,0} & \cdots & u_{0,\beta-1} & u_{1,0} & \cdots & u_{1,\beta-1} & \cdots & u_{L_F-1,0} & \cdots & u_{L_F-1,\beta-1} \end{bmatrix} \tag{C.8}$$

with $u_{i,j} = u_{i\beta+j}$ being the taps of the feed-forward filter. Note that we have assumed that the feed-forward filter spans L_F bit periods with β taps per bit period. From equation (C.5) it follows that :

$$\mathbf{R}_k = \underbrace{\begin{bmatrix} \mathbf{h}_0 & \mathbf{h}_1 & \cdots & \mathbf{h}_{L_h} & \mathbf{0}_\beta & \cdots & \mathbf{0}_\beta \\ \mathbf{0}_\beta & \mathbf{h}_0 & \mathbf{h}_1 & \cdots & \mathbf{h}_{L_h} & \cdots & \mathbf{0}_\beta \\ \vdots & \ddots & \ddots & \ddots & \ddots & \ddots & \vdots \\ \mathbf{0}_\beta & \cdots & \mathbf{0}_\beta & \mathbf{h}_0 & \mathbf{h}_1 & \cdots & \mathbf{h}_{L_h} \end{bmatrix}}_{H} \underbrace{\begin{bmatrix} a_k \\ a_{k-1} \\ \vdots \\ a_{k-(L_h+L_F-1)} \end{bmatrix}}_{\mathbf{A}_k} + \underbrace{\begin{bmatrix} \mathbf{n}_k \\ \mathbf{n}_{k-1} \\ \vdots \\ \mathbf{n}_{k-(L_F-1)} \end{bmatrix}}_{\mathbf{N}_k} \tag{C.9}$$

Note that H is a $\beta L_F \times (L_h + L_F)$ matrix and $\mathbf{0}_\beta$ denotes a column vector of β zeros.

C.1.3 Feedback Filter

We assume that the decision in the k^{th} bit period, $\hat{a}_k$, corresponds to the transmit bit $a_{k-\Delta}$ where the delay Δ is appropriately chosen. The feedback filter synthesizes the ISI caused by the previously detected bits, $\hat{a}_{k-1}, \hat{a}_{k-2}, \ldots, \hat{a}_{k-L_B}$ where L_B is the number of feedback taps. While a practical DFE feeds back actual decisions, the optimization is carried out assuming correct decisions. Therefore, the output of the feedback filter, x_k, is given by :

$$x_k = \mathbf{v}^T \underbrace{\begin{bmatrix} a_{k-\Delta-1} \\ a_{k-\Delta-2} \\ \vdots \\ a_{k-\Delta-L_B} \end{bmatrix}}_{\mathbf{a}_{k-\Delta-1}} \tag{C.10}$$

C.1.4 Slicer Input

Therefore, the input to the slicer, w_k, can be expressed as :

$$w_k = y_k - x_k = \mathbf{u}^T \mathbf{R}_k - \mathbf{v}^T \mathbf{a}_{k-\Delta-1} \tag{C.11}$$

Defining $\mathbf{c}^T = [\mathbf{u}^T \quad \mathbf{v}^T]$, we get :

$$w_k = \mathbf{c}^T \begin{bmatrix} \mathbf{R}_k \\ -\mathbf{a}_{k-\Delta-1} \end{bmatrix} \tag{C.12}$$

C.1.5 Mean Square Error

The mean square error, $\xi = E\left[(w_k - a_{k-\Delta})^2\right]$, can then be written as :

$$\xi = \mathbf{c}^T \begin{bmatrix} E\left[\mathbf{R}_k \mathbf{R}_k^T\right] & -E\left[\mathbf{R}_k \mathbf{a}_{k-\Delta-1}^T\right] \\ -E\left[\mathbf{a}_{k-\Delta-1} \mathbf{R}_k^T\right] & E\left[\mathbf{a}_{k-\Delta-1} \mathbf{a}_{k-\Delta-1}^T\right] \end{bmatrix} \mathbf{c} - 2\mathbf{c}^T \begin{bmatrix} E\left[\mathbf{R}_k a_{k-\Delta}\right] \\ -E\left[\mathbf{a}_{k-\Delta-1} a_{k-\Delta}\right] \end{bmatrix} + E\left[a_{k-\Delta}^2\right] \tag{C.13}$$

where $E[\cdot]$ is the expectation operator. Upon evaluation of the various correlation matrices, we get :

$$\frac{\xi}{\sigma_a^2} = \mathbf{c}^T \underbrace{\begin{bmatrix} HH^T + \frac{N_0}{2\sigma_a^2} R_N & -HJ_\Delta \\ -J_\Delta^T H^T & I_{L_B} \end{bmatrix}}_{A} \mathbf{c} - 2\mathbf{c}^T \underbrace{\begin{bmatrix} H\mathbf{1}_\Delta \\ \mathbf{0}_{L_B} \end{bmatrix}}_{\mathbf{b}} + 1 \tag{C.14}$$

where $\mathbf{0}_{L_B}$ is a column vector of L_B zeros and I_{L_B} is the $L_B \times L_B$ identity matrix. Note that we have assumed that the transmit bits are independent and equally likely and have a variance of σ_a^2. J_Δ and $\mathbf{1}_\Delta$ are defined in Matlab pseudo-code as follows :

Definition C.1 Various matrix/vector definitions

Matrix J_Δ:

```
Initialize: $J_\Delta = 0_{L \times L_B}$ where $L = L_h + L_F$
if $0 \leq \Delta \leq L - 2$ then
    $J_\Delta(\Delta + 2 : \Delta + K + 1, 1 : K) = \text{eye}(K, K)$ where $K = \min(L_B, L - \Delta - 1)$
end if
```

Vector $\mathbf{1}_\Delta$:

```
Initialize: $\mathbf{1}_\Delta = 0_{L \times 1}$
if $0 \leq \Delta \leq L - 1$ then
    $\mathbf{1}_\Delta(\Delta + 1) = 1$
end if
```

Note that $R_N = E\left[\mathbf{N}_k \mathbf{N}_k^T\right] / (N_0/2)$ and can be easily determined from the noise autocorrelation given by equations (C.3) and (C.4).

Minimizing the mean square error given in equation (C.14), we get the optimum DFE coefficients :

$$\mathbf{c}_{opt} = A^{-1}\mathbf{b} \tag{C.15}$$

The corresponding minimum mean square error is then :

$$\xi_{\text{min}} = \sigma_a^2 \cdot \left(1 - \mathbf{c}_{opt}^T \mathbf{b}\right) \tag{C.16}$$

The sampling instant τ_0 and the delay Δ are chosen to minimize ξ_{min}.

C.2 Residual ISI and Noise Variance after the DFE

Once the DFE coefficients are known, we need to determine the bit error rate and the power penalty for the link. The most common approach is to assume that the error $e_k = w_k - a_{k-\Delta}$ is Gaussian with variance ξ_{min}. In this case, the bit error rate is given by $Q(\sqrt{\sigma_a^2/\xi_{\text{min}}})$. Note that the DFE that minimizes the mean square error strikes an optimum balance between residual ISI and noise enhancement. This residual ISI may cause e_k to be non-Gaussian.

Our approach is to determine the effective channel at the input to the slicer. This can be done by assuming zero error propagation, which is usually valid at bit error rates of 10^{-12}

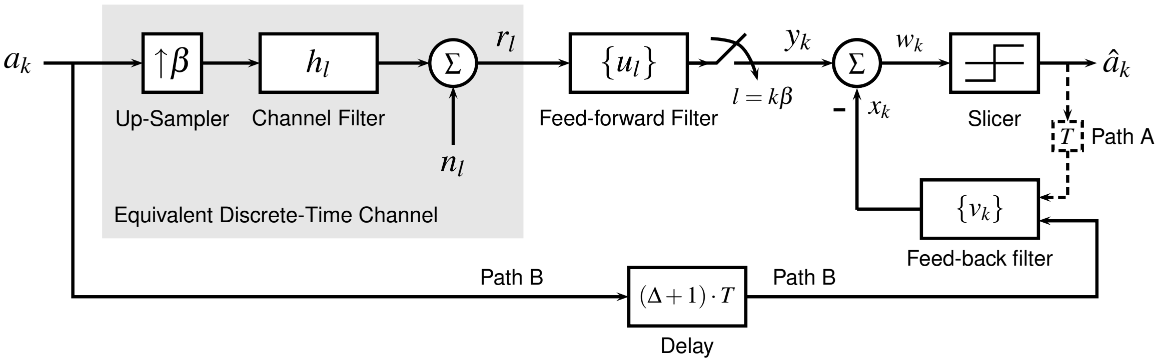

Figure C.2: End-to-End DFE Link with and without error propagation

and lower. In this case, the input to the feedback filter is the appropriately delay transmit bit sequence, as shown in Fig. C.2. So the dashed path labeled Path A is replaced by that marked Path B.

Given the channel filter and the DFE coefficients, it is straightforward to determine the effective channel from a_k to w_k in Fig. C.2. From equation (C.11), which assumes correct feedback decisions, the slicer input w_k can be written as :

$$w_k = \mathbf{u}^T H \mathbf{A}_k - \mathbf{v}^T \mathbf{a}_{k-\Delta-1} + \mathbf{u}^T \mathbf{N}_k \tag{C.17}$$

Therefore, the effective channel is determined by $H^T\mathbf{u}$ and $\mathbf{v}$. The method is summarized in Procedure C.2 via Matlab pseudo-code.

Procedure C.2 Residual ISI Estimation

```
Initialize the effective channel taps to zero:
    $\mathbf{q} = \mathrm{zeros}(L, 1)$ where $L = \max(L_h + L_F, L_B + \Delta + 1)$
Determine the contribution of the feed-forward filter to the effective channel:
    $\tilde{\mathbf{u}} = H^T \mathbf{u}$
    $\mathbf{q}(1 : L_h + L_F) = \tilde{\mathbf{u}}$
If applicable, subtract the contribution of the feedback filter from the effective channel estimated thus far:
    if $L_B \neq 0$ then
        $\mathbf{q}(\Delta + 2 : L_B + \Delta + 1) -= \mathbf{v}$
    end if
Then $\mathbf{q}(\Delta + 1)$ is the coefficient for the desired bit and remaining terms are the residual ISI coefficients.
```

The variance of the residual noise $v_k = \mathbf{u}^T \mathbf{N}_k$ is given by :

$$\sigma_v^2 = \frac{N_0}{2} \mathbf{u}^T R_N \mathbf{u} \tag{C.18}$$

Given the residual ISI and the noise variance, the bit error rate can be quickly estimated using the procedure outlined in Appendix A.

APPENDIX D

CHANNEL CAPACITY

Consider the vector channel :

$$\mathbf{Y} = \mathbf{X} + \mathbf{N} \tag{D.1}$$

where $\mathbf{X}$ is an L-dimensional transmit vector, $\mathbf{N}$ is the noise vector and $\mathbf{Y}$ is the corresponding received vector. The capacity of such a channel is given by [69] :

$$C = \frac{1}{T} \sup_{f_{\mathbf{X}}} I(\mathbf{X};\mathbf{Y}) \quad \text{bits/sec} \tag{D.2}$$

where the supremum is taken over all probability distributions of $\mathbf{X}$, $f_{\mathbf{X}}$, and T is time interval occupied by the transmit vector $\mathbf{X}$. The mutual information between $\mathbf{X}$ and $\mathbf{Y}$, denoted by $I(\mathbf{X};\mathbf{Y})$, is defined as :

$$I(\mathbf{X};\mathbf{Y}) = h(\mathbf{X}) - h(\mathbf{X}|\mathbf{Y}) \tag{D.3}$$

where the differential entropy $h(\mathbf{X})$ is computed via :

$$h(\mathbf{X}) = -\underset{\mathbf{X}\in\chi}{\int \cdots \int} f_{\mathbf{X}} \log_2 [f_{\mathbf{X}}]\, d\mathbf{X} \tag{D.4}$$

At an intuitive level, the differential entropy $h(\mathbf{X})$ is a measure of the uncertainty or randomness associated with $\mathbf{X}$. The mutual information is then a measure of the uncertainty remaining in the transmit vector $\mathbf{X}$ even after we have eliminated the uncertainty associated with $\mathbf{X}$ given the received vector $\mathbf{Y}$. Channel capacity is nothing but the maximum possible value of this residual uncertainty over all possible probability distributions for the transmit vector.

An alternate expression for the mutual information that is practically more useful is :

$$I(\mathbf{X};\mathbf{Y}) = h(\mathbf{Y}) - h(\mathbf{Y}|\mathbf{X}) \tag{D.5}$$

When the noise is independent of the transmit vector, this can be simplified further :

$$I(\mathbf{X};\mathbf{Y}) = h(\mathbf{Y}) - h(\mathbf{N}) \tag{D.6}$$

Another useful inequality is the entropy power inequality that states :

$$e^{2h(\mathbf{X}+\mathbf{N})} \geq e^{2h(\mathbf{X})} + e^{2h(\mathbf{N})} \tag{D.7}$$

when **X** and **N** are independent.

REFERENCES

[1] R. M. Metcalfe and D. R. Boggs, "Ethernet: Distributed Packet Switching for Local Computer Networks," *Communications of the ACM*, vol. 19, no. 7, pp. 395–404, July 1976.

[2] *10 Gigabit Ethernet Technology Overview*. [Online]. Available: http://www.ethernetalliance.org/technology/white_papers/10gea_overview.pdf (June 5, 2007)

[3] A. Flatman, "In-Premises Optical Fibre Installed Base Analysis to 2007," in *IEEE 802.3aq Task Force Meeting, Orlando*, March 2004. [Online]. Available: http://www.ieee802.org/3/aq/public/mar04/flatman_1_0304.pdf (June 5, 2007)

[4] *IEEE 802.3ae-2002*, 10 Gigabit Ethernet Standard, 2002.

[5] Z. Haas and M. A. Santoro, "A Mode-Filtering Scheme for Improvement of the Bandwidth-Distance Product in Multimode Fiber Systems," *IEEE Journal of Lightwave Technology*, vol. 11, no. 7, pp. 1125–1131, 1993.

[6] E. G. Johnson, J. Stack, and C. Koehler, "Light Coupling by a Vortex Lens into Graded Index Fiber," *IEEE Journal of Lightwave Technology*, vol. 19, no. 5, pp. 753–758, 2001.

[7] K. M. Patel and S. E. Ralph, "Improved multimode link bandwidth using spatial diversity in signal reception," in *Conference on Lasers and Electro-Optics, CLEO*, May 2001, p. 416.

[8] P. Pepeljugoski, J. Schaub, J. Tierno, J. Kash, S. Gowda, B. Wilson, and A. Hajimiri, "Improved Performance of 10 Gb/s Multimode Fiber Optic Links Using Equalization," in *Optical Fiber Communications Conference*, March 2003.

[9] R. Khosla, K. Kumar, K. M. Patel, C. Pelard, and S. E. Ralph, "Equalization of 10GbE multimode fiber links," in *Annual Meeting of the Lasers and Electro-Optics Society, LEOS '03*, vol. 1, October 2003, pp. 27–28.

[10] J. D. Ingham, R. V. Penty, I. H. White, and D. G. Cunningham, "Electronic equalisation for length extension of ×2 to ×3 in 10 Gbit/s multimode-fibre data communication links," *Electronics Letters*, vol. 40, no. 22, pp. 1437–1439, October 2004.

[11] K. Balemarthy, S. Ralph, R. Lingle Jr., G. Oulundsen, Y. Sun, and J. George, "Electronic dispersion compensation of non-ideal multimode fiber links," in *Optical Fiber Communications Conference*, March 2005.

[12] J. P. Weem, P. Kirkpatrick, and J.-M. Verdiell, "Electronic Dispersion Compensation for 10 Gigabit Communication Links over FDDI Legacy Multimode Fiber," in *Optical Fiber Communications Conference*, March 2005.

[13] C. Xia and W. Rosenkranz, "Statistical Analysis of Electrical Equalization of Differential Mode Delay in MMF Links for 10-Gigabit Ethernet," in *Optical Fiber Communications Conference*, March 2005.

[14] C. Xia, M. Ajgaonkar, and W. Rosenkranz, "On the Performance of the Electrical Equalization Technique in MMF Links for 10-Gigabit Ethernet," *IEEE Journal of Lightwave Technology*, vol. 23, no. 6, pp. 2001–2011, June 2005.

[15] J. G. Proakis, *Digital Communications*. McGraw-Hill, 1995.

[16] *IEEE 802.3aq, in progress*, 10G-LRM Task Force. [Online]. Available: http://www.ieee802.org/3/aq (June 5, 2007)

[17] K. Balemarthy, S. Ralph, R. Lingle Jr., G. Oulundsen, Y. Sun, J. George, and J. Abbott, "Fiber Modeling Resolution and Assumptions: Analysis Data, and Recommendations," in *IEEE 802.3aq Task Force Meeting, San Antonio*, November 2004. [Online]. Available: http://www.ieee802.org/3/aq/public/nov04/balemarthy_1_1104.pdf (June 5, 2007)

[18] ——, "Fiber Modeling Resolution and Assumptions: Analysis Data, and Recommendations: Addendum 2," in *IEEE 802.3aq Task Force Meeting, San Antonio*, November 2004. [Online]. Available: http://www.ieee802.org/3/10GMMFSG/email/msg00502.html (June 5, 2007)

[19] R. Lingle Jr., K. Balemarthy, and S. Ralph, "Finite Equalizer Performance for TP3 Stressed Sensitivity Test on Gen67YY," in *IEEE 802.3aq Task Force Meeting, Atlanta*, March 2005. [Online]. Available: http://www.ieee802.org/3/aq/public/mar05/lingle_1_0305.pdf (June 5, 2007)

[20] J. Balakrishnan and C. R. Johnson Jr., "Time-Reversal Diversity in Decision Feedback Equalization," in *Proceedings of Allerton Conference on Communications, Control and Computing*, Monticello, IL, USA, October 2000.

[21] C. S. McGahey, A. C. Singer, and U. Madhow, "BAD : A Bi-directional Arbitrated Decision Feedback Equalizer," in *Proceedings of Conference on Information Sciences and Systems*, Princeton, NJ, USA, March 2000.

[22] K. Balemarthy and S. E. Ralph, "Bidirectional DFEs for 10Gb/s Ethernet over Multimode Fiber Links," in *National Conference on Communications, Kanpur, India*, January 2007.

[23] ——, "Bidirectional DFEs for 10Gb/s Ethernet over Multimode Fiber Links: Complexity Reduction and Reach Extension," in *Optical Fiber Communications Conference*, March 2007.

[24] The Ethernet Alliance, "The Need for 100G Ethernet?" in *DesignCon*, February 2006.

[25] H. R. Stuart, "Dispersive multiplexing in multimode fiber," in *Optical Fiber Communications Conference*, vol. 3, March 2000, pp. 305–307.

[26] A. R. Shah, R. C. J. Hsu, A. Tarighat, A. H. Sayed, and B. Jalali, "Coherent Optical MIMO (COMIMO)," *IEEE Journal of Lightwave Technology*, vol. 23, no. 8, pp. 2410–2419, August 2005.

[27] K. M. Patel and S. E. Ralph, "Spatially resolved detection for enhancement of multimode-fiber-link performance," in *Annual Meeting of the Lasers and Electro-Optics Society, LEOS*, vol. 2, November 2001, pp. 483–484.

[28] S. E. Ralph, K. M. Patel, C. Argon, A. Polley, and S. W. McLaughlin, "Intelligent Receivers for Multimode Fibers: Optical and Electronic Equalization of Differential Modal Delay," in *Annual Meeting of the Lasers and Electro-Optics Society, LEOS*, vol. 1, 2002, pp. 295–296.

[29] K. M. Patel and S. E. Ralph, "Enhanced Multimode Fiber Link Performance Using a Spatially Resolved Receiver," *IEEE Photonics Technology Letters*, vol. 14, no. 3, pp. 393–395, March 2002.

[30] ——, "Enhanced Multimode Fiber Link Performance Using a Spatially Resolved Photodetector," in *Conference on Lasers and Electro-Optics, CLEO*, vol. 1, 2002, p. 498.

[31] K. M. Patel, A. Polley, and S. E. Ralph, "Modal Dispersion Compensation by Simultaneous Use of Spatially Resolved Equalization and Restricted Mode Launch," in *Annual Meeting of the Lasers and Electro-Optics Society, LEOS*, vol. 2, 2003, pp. 973–974.

[32] K. M. Patel and S. E. Ralph, "Multimode Fiber Link Equalization by Mode Filtering Via a Multisegment Photodetector," in *IEEE Microwave Symposium*, vol. 2, June 2003, pp. 8–13.

[33] K. M. Patel, A. Polley, K. Balemarthy, and S. E. Ralph, "Spatially Resolved Detection and Equalization of Modal Dispersion Limited Multimode Fiber Links," *IEEE Journal of Lightwave Technology*, vol. 24, no. 7, pp. 2629–2636, July 2006.

[34] C. Argon, K. M. Patel, S. W. McLaughlin, and S. E. Ralph, "Spatially Resolved Equalization and Decision Feedback Equalization of Multimode Fiber Links," in *Lasers and Electro-Optics Society Summer Topical Meeting*, July 2002, pp. 19–20.

[35] ——, "Spatially Resolved Equalization and Forward Error Correction for Multimode Fiber Links," in *IEEE International Conference on Communications, ICC*, vol. 3, May 2002, pp. 1726–1730.

[36] ——, “Exploiting Diversity in Multimode Fiber Communications Links Via Multisegment Detectors and Equalization,” *IEEE Communications Letters*, vol. 7, no. 8, pp. 400–402, August 2003.

[37] K. Balemarthy and S. E. Ralph, “Multiple-Input, Multiple-Output Processing of Multi-mode Fiber Links,” in *Annual Meeting of the Lasers and Electro-Optics Society, LEOS*, October 2006, pp. 639–640.

[38] P. Pepeljugoski, D. Kuchta, Y. Wark, P. Pleunis, and G. Kuyt, “15.6Gb/s Transmission over 1km of Next Generation Multimode Fiber,” *IEEE Photonics Technology Letters*, vol. 14, no. 5, pp. 717–719, May 2002.

[39] K. Balemarthy, A. Polley, and S. E. Ralph, “Electronic Equalization of Multi-km 10Gb/s Multimode Fiber Links: Mode Coupling Effects,” *IEEE Journal of Lightwave Technology*, vol. 24, pp. 4885–4894, December 2006.

[40] J. A. Buck, *Fundamentals of Optical Fibers*. John Wiley & Sons, 1995.

[41] M. Webster, L. Raddatz, I. H. White, and D. G. Cunningham, “A Statistical Analysis of Conditioned Launch for Gigabit Ethernet Links Using Multimode Fiber,” *IEEE Journal of Lightwave Technology*, vol. 17, no. 9, pp. 1532–1541, September 1999.

[42] *108 Fiber Model*, IEEE 802.3aq (10G-LRM) Task Force. [Online]. Available: http://www.ieee802.org/3/aq/public/tools/108fiberModel (June 5, 2007)

[43] *Monte Carlo Fiber Model*, IEEE 802.3aq (10G-LRM) Task Force. [Online]. Available: http://www.ieee802.org/3/aq/public/tools/MonteCarlo/OM1/ (June 5, 2007)

[44] S. D. Personick, “Baseband Linearity and Equalization in Fiber Optic Digital Communications Systems,” *Bell System Technical Journal*, vol. 52, no. 7, pp. 1175–1194, September 1973.

[45] K. M. Patel, “Spatially Resolved Equalization: A New Concept in Intermodal Dispersion Compensation for Multimode Fiber,” Ph.D. dissertation, Georgia Institute of Technology, 2004.

[46] *Connector Transfer Matrices*, IEEE 802.3aq (10G-LRM) Task Force. [Online]. Available: http://www.ieee802.org/3/aq/public/tools/ctm/ (June 5, 2007)

[47] *IEEE 802.3z-1998*, Gigabit Ethernet Standard, 1998.

[48] J. Ewen, “PIE Metric Comparison: 108-Fiber & Monte Carlo Delay Sets,” in *IEEE 802.3aq Task Force Meeting, San Antonio*, November 2004. [Online]. Available: http://www.ieee802.org/3/aq/public/nov04/ewen_2_1104.pdf (June 5, 2007)

[49] G. D. Forney Jr., “Maximum-likelihood Sequence Estimation,” *IEEE Transactions on Information Theory*, vol. 18, no. 3, pp. 363–378, May 1972.

[50] A. Färbert, S. Langenbach, N. Stojanovic, C. Dorschky, T. Kupfer, C. Schulien, J.-P. Elbers, H. Wernz, H. Griesser, and C. Glingener, "Performance of a 10.7 Gb/s Receiver with Digital Equaliser using Maximum Likelihood Sequence Estimation," in *European Conference on Optical Communication*, Stockholm, 2004.

[51] J. R. Barry, E. A. Lee, and D. G. Messerschmitt, *Digital Communication*, 3rd ed. Kluwer Academic, 2004.

[52] R. D. Gitlin and S. B. Weinstein, "Fractionally-Spaced Equalization: An Improved Digital Transversal Equalizer," *Bell System Technical Journal*, vol. 60, no. 2, pp. 275–296, February 1981.

[53] T. Berger and D. W. Tufts, "Optimum Pulse Amplitude Modulation Part I: Transmitter-Receiver Design and Bounds from Information Theory," *IEEE Transactions on Information Theory*, vol. 13, no. 2, pp. 196–208, April 1967.

[54] H. Nyquist, "Certain Factors Affecting Telegraph Speed," *Bell System Technical Journal*, vol. 3, p. 324, April 1924.

[55] D. W. Tufts, "Nyquist's Problem - The Joint Optimization of Transmitter and Receiver in Pulse Amplitude Modulation," *Proceedings of the IEEE*, vol. 53, no. 3, pp. 248–259, March 1965.

[56] R. W. Lucky, "Automatic Equalization for Digital Communications," *Bell System Technical Journal*, vol. 44, pp. 547–588, April 1965.

[57] M. E. Austin, "Decision-Feedback Equalization for Digital Communication over Dispersive Channels," M.I.T., Research Laboratory of Electronics, Tech. Rep. 461, August 1967.

[58] J. Salz, "Optimum Mean-Square Decision Feedback Equalization," *Bell System Technical Journal*, vol. 52, no. 8, pp. 1341–1373, October 1973.

[59] J. Cioffi, *Class Notes on Equalization, Stanford University*. [Online]. Available: http://www.stanford.edu/class/ee379a/course_reader/chap3.pdf

[60] N. Al-Dhahir and J. M. Cioffi, "MMSE Decision-Feedback Equalizers: Finite-Length Results," *IEEE Transactions on Information Theory*, vol. 41, no. 4, pp. 961–965, July 1995.

[61] S. Ariyavisitakul, "A Decision-Feedback Equalizer with Selective Time-Reversal operation for High-Rate Indoor Radio Communication," in *GLOBECOM*, vol. 3, December 1990, pp. 2035–2039.

[62] ——, "A Decision-Feedback Equalizer with Selective Time-Reversal Structure," *IEEE Journal on Selected Areas in Communications*, vol. 10, no. 3, pp. 599–613, April 1992.

[63] H. Suzuki, "Performance of a New Adaptive Diversity-Equalisation for Digital Mobile Radio," *Electronics Letters*, vol. 26, no. 10, pp. 626–627, May 1990.

[64] J. K. Nelson, A. C. Singer, U. Madhow, and C. S. McGahey, "BAD : Bidirectional Arbitrated Decision-Feedback Equalization," *IEEE Transactions on Communications*, vol. 53, no. 2, pp. 214–218, February 2005.

[65] J. Balakrishnan and C. R. Johnson Jr., "Bidirectional Decision Feedback Equalizer: Infinite-Length Results," in *Proceedings of Asilomar Conference on Signals, Systems and Computers*, Pacific Grove, CA, USA, November 2001, pp. 1450—1454.

[66] J. Balakrishnan, "Bidirectional Decision Feedback Equalization and MIMO Channel Training," Ph.D. dissertation, Cornell University, 2002.

[67] J. M. Cioffi, G. P. Dudevoir, M. V. Eyuboglu, and G. D. Forney Jr., "MMSE Decision-Feedback Equalizers and Coding – Part I: Equalization Results," *IEEE Transactions on Communications*, vol. 43, no. 10, pp. 2582–2594, 1995.

[68] D. A. Pierre, *Optimization Theory with Applications*. Dover Publications Inc., 1986.

[69] C. E. Shannon, "A Mathematical Theory of Communication," *Bell System Technical Journal*, vol. 27, pp. 379–423, 623–656, July and October 1948.

[70] T. M. Cover and J. A. Thomas, *Elements of Information Theory*. John Wiley & Sons Inc., 2006.

[71] R. You and J. M. Kahn, "Upper-Bounding the Capacity of Optical IM/DD Channels With Multiple-Subcarrier Modulation and Fixed Bias Using Trigonometric Momemt Space Method," *IEEE Transactions on Information Theory*, vol. 48, no. 2, pp. 514–523, February 2002.

[72] S. Hranilovic and F. R. Kschischang, "Capacity Bounds for Power- and Band-Limited Optical Intensity Channels Corrupted by Gaussian Noise," *IEEE Transactions on Information Theory*, vol. 50, no. 5, pp. 784–795, May 2004.

[73] S. Hranilovic, "Spectrally Efficient Signaling for Wireless Optical Intensity Channels," Ph.D. dissertation, University of Toronto, 2003.

[74] A. J. Paulraj, D. A. Gore, R. U. Nabar, and H. Bolcskei, "An Overview of MIMO Communications – A Key to Gigabit Wireless," *Proceedings of the IEEE*, vol. 92, no. 2, pp. 198–218, February 2004.

[75] A. R. Shah, R. C. J. Hsu, and B. Jalali, "ISI Equalization for a Coherent Optical MIMO (COMIMO) System," in *Conference on Lasers and Electro-Optics, CLEO*, May 2005, pp. 1348–1350.

[76] R. C. J. Hsu, A. Tarighat, A. Shah, A. H. Sayed, and B. Jalali, "Capacity Enhancement in Coherend Optical MIMO (COMIMO) Multimode Fiber Links," *IEEE Communications Letters*, vol. 10, no. 3, pp. 195–197, March 2006.

[77] G. J. Foschini, “Layered Space-Time Architecture for Wireless Communication in a Fading Environment When Using Multi-Element Antennas,” *Bell Labs Technical Journal*, pp. 41–59, Autumn 1996.

[78] S. E. Miller, “Mode detection and delay equalization in multimode optical fiber transmission systems,” U. S. Patent 3777150, December 4, 1973.

[79] C. P. Tsekrekos, A. Martinez, F. M. Huijskens, and A. M. J. Koonen, “Mode Group Diversity Multiplexing Transceiver Design for Graded-Index Multimode Fibres ,” in *European Conference on Optical Communciation*, vol. 3, September 2005, pp. 727–728.

[80] S. Schollman, C. Xia, and W. Rosenkranz, “Experimental Investigations of Mode Group Diversity Multiplexing on Multimode Fibre,” in *Optical Fiber Communications Conference*, March 2006.

[81] E. Alon, V. Stojanocvic, J. M. Kahn, S. Boyd, and M. Horowitz, “Equalization of Modal Dispersion in Multimode Fiber using Spatial Light Modulators,” in *GLOBECOM ’04*, vol. 2, 2004, pp. 1023–1029.

[82] Y. Sun, M. E. Ali, K. Balemarthy, R. L. Lingle Jr., S. E. Ralph, and B. E. Lemoff, “10Gb/s transmission over 300m OM3 fiber from 990-1080nm with electronic dispersion compensation,” in *Optical Fiber Communications Conference*, March 2006.

[83] E. Telatar, “Capacity of Multiantenna Gaussian Channels,” *European Transactions on Telecommunications*, vol. 10, no. 6, pp. 585–595, November 1999.

[84] P. Balaban and J. Salz, “Optimum Diversity Combining and Equalization in Digital Data Transmission with Applications to Cellular Mobile Radio – Part I: Theoretical considerations,” *IEEE Transactions on Communications*, vol. 40, pp. 885–894, May 1992.

[85] A. Duel-Hallen, “Equalizers for Multiple Input/Multiple Output Channels and PAM Systems with Cylostationary Input Sequences,” *IEEE Journal on Selected Areas in Communications*, vol. 10, no. 3, pp. 630–639, April 1992.

[86] N. Al-Dhahir and A. H. Sayed, “The Finite-Length Multi-Input Multi-Output MMSE-DFE,” *IEEE Transactions on Signal Processing*, vol. 48, no. 10, pp. 2921–2936, October 2000.

[87] J.-F. Frigon and B. Daneshrad, “A Multiple Input-Multiple Output (MIMO) Adaptive Decision Feedback Equalizer (DFE) with Cancellation for Wideband Space-Time Communications,” *International Journal of Wireless Networks*, vol. 9, no. 1, pp. 13–23, January 2002.

[88] D. Marcuse, *Theory of Dielectric Optical Waveguides*. Academic Press, 1991.

[89] R. Olshansky, “Mode Coupling Effects in Graded-Index Optical Fibers,” *Applied Optics*, vol. 14, no. 4, pp. 935–945, 1975.

[90] ——, “Distortion Losses in Cabled Optical Fibers,” *Applied Optics*, vol. 14, no. 1, pp. 20–21, January 1975.

[91] B. Stoltz and D. Yevick, “Influence of Mode Coupling on Differential Modal Delay,” *Applied Optics*, vol. 22, no. 15, pp. 2349–2355, August 1983.

[92] D. Yevick and B. Stoltz, “Effect of Mode Coupling on the Total Pulse Response of Perturbed Optical Fibers,” *Applied Optics*, vol. 22, no. 7, pp. 1010–1015, April 1983.

[93] M. Ohashi, K. Kitayama, and S. Seikai, “Mode coupling effects in a graded-index fiber cable,” *Applied Optics*, vol. 20, no. 14, pp. 2433–2438, 15 July 1981.

[94] K. Nagano and S. Kawakami, “Measurements of mode conversion coefficients in graded-index fibers,” *Applied Optics*, vol. 19, no. 14, 15 July 1980.

[95] K. Kitayama and M. Ikeda, “Mode Coupling Coefficient Measurements in Optical Fibers,” *Applied Optics*, vol. 17, no. 24, pp. 3979–3983, December 1978.

[96] M. J. Yadlowsky and A. R. Mickelson, “Distributed loss and mode coupling and their effect on time-dependent propagation in multimode fibers,” *Applied Optics*, vol. 32, no. 33, 20 November 1993.